COMPREHENSIVE NUMERICAL STUDY OF MICROFLUIDIC FUEL CELLS

by

Ali Ebrahimi Khabbazi

B.Sc., University of Tehran, Iran, 2007

A THESIS SUBMITTED IN PARTIAL FULFILLMENT OF
THE REQUIREMENTS FOR THE DEGREE OF

MASTER OF APPLIED SCIENCE

in

The College of Graduate Studies
(Mechanical Engineering)

THE UNIVERSITY OF BRITISH COLUMBIA
(Okanagan)

August 2010

Abstract

The microfluidic fuel cell or laminar flow-based fuel cell is a membraneless fuel cell which typically consists of two electrodes mounted within a T- or Y-shaped microchannel. Aqueous fuel and oxidant are introduced from the two inlets of the channel and flow together side-by-side toward the end of the channel. The Reynolds number in the microchannel is low, and hence viscous forces are dominant over the inertial forces. This causes the anolyte and catholyte form a co-laminar flow inside the microchannel which is required to maintain the separation of the fuel and oxidant and limit the reactions to the appropriate electrodes.

In this work, a comprehensive numerical model of the microfluidic fuel cell is developed using COMSOL Multiphysics. This model accounts for the mass and momentum transport phenomena inside the device as well as the electrochemical reaction kinetics which are described by the Butler-Volmer equations. Potential equations are used to model both the ionic conduction in the electrolyte and the electrical conduction in the solid electrodes. The validity of the developed model is first checked by verifying it against the numerical and experimental results previously reported in the literature. The model is then used to assess the effect of different modifications, which have been applied on the microfluidic fuel cell since its advent, by calculating the polarization curves associated with each modification.

In this thesis, a novel design of microfluidic fuel cell with a tapered channel is also proposed. Using the numerical model, it is shown that the tapered geometry improves the fuel utilization by up to four times in addition to a substantial improvement in the power density.

A similar numerical model is developed to study the performance of a microfluidic fuel cell with flow-through porous electrodes. Using this model, the effect of porosity on the net power output of the fuel cell is investigated and an optimum value for porosity is calculated. The model presented is a valuable tool, as it can be used to study the effect of any modifications on the cell performance before fabricating and testing the new design in an extensive experimental study.

Table of Contents

Abstract ii

Table of Contents iv

List of Tables vi

List of Figures vii

Nomenclature xii

Acknowledgements xiv

Dedications xv

1. Introduction 1

1.1 Fuel Cell 1

1.2 Fuel Cell History and Classification 3

1.3 Miniaturization of Fuel Cells 6

1.4 Microfluidic fuel cell 8

1.4.1 Fundamental Principles in Microfluidic Fuel Cells 13

1.4.2 Contributions and Technical Advances in Microfluidic Fuel Cells 20

1.4.2.1 Experimental Contributions 21

1.4.2.2 Numerical Modeling Advances in Microfluidic Fuel Cells 25

1.4.3 Challenges and Opportunities 27

1.5 Motivation and Layout of the Thesis 30

2. Modeling Steps in COMSOL 32

2.1 Constants 33

2.2 Fluid Flow 35

2.3 Charge Conservation 38

2.4 Mass Transport 41

2.5 Reaction Kinetics 44

2.6 Implementation in COMSOL 47
2.6.1 Solution Procedures 47
2.6.2 Meshing 50

2.7 Assumptions and Limitations of the Developed Numerical Model 51

3. Results for Microfluidic Fuel Cells with Solid Electrodes 52

3.1 Model Validation 52

3.2 Results of Developed Model for Different Designs 57
3.2.1 Study the Effect of the Length of the Channel 57
3.2.2 Study the Effect of the Different Cross-Section Aspect Ratios 59
3.2.3 Study the Effect of Inserting the 3rd Flow 67
3.2.4 Study the Effect of Multiple Inlets 69

3.3 Proposed Geometry 72

4. Results for Microfluidic Fuel Cells with Flow-Through Porous Electrodes 76

4.1 Introduction 76

4.2 Modeling 79
4.2.1 Geometry 79
4.2.2 Governing Equations 79

4.3 Results 88

5. Conclusions and Suggestions for Future Work 92

5.1 Conclusions 92

5.2 Future Work 95

6. References 97

List of Tables

Table 3.1 The Constants Used in the Anodic and Cathodic Flows for Solid Electrode Design ……..…… 53

Table 4.1 The Constants Used in the Anodic and Cathodic Flows for Porous Electrode Design ……..…… 86

List of Figures

Figure 1.1 A general schematic of a fuel cell 2
Figure 1.2 A schematic of William Grove's experiment (Hydrogen and oxygen are combined, and an electric current is produced) [5]. 3
Figure 1.3 A schematic of a hydrogen-oxygen PEM fuel cell showing the membrane, catalysts and gas diffusion layers sandwiched between the bipolar plates..... 5
Figure 1.4 The relative advantage of fuel cells over the widely used Li-ion batteries in terms of energy density [3] 7
Figure 1.5 This figure shows a typical Y-shaped microfluidic fuel cell with the plot of fuel concentration over the entire fuel cell domain. Fuel and oxidant are introduced from the two inlets of the channel. They are flowing together side-by-side forming a co-laminar flow. Electrons and protons are produced on the anode. Protons travel through the electrolyte and electrons take the external circuit toward the cathode. Protons and electrons meet oxidant species on the cathode to complete the reduction reaction and generate electricity..... 9
Figure 1.6 This figure shows the extension of the electrodes up to the point that they do not reach to the mixing region to avoid fuel crossover. 10
Figure 1.7 The Classical Energy diagram for a simple chemical reaction showing the energy hill [5] 14
Figure 1.8 A typical polarization curve for a direct formic acid fuel cell is shown. Three main polarization regions are demonstrated. 16
Figure 1.9 A schematic of an air-breathing microfluidic fuel cell with porous cathode structure is shown (Jayashree et al. [29]). Oxygen is captured from the ambient air through the porous cathode. 22
Figure 1.10 Three different strategies for the active control of concentration boundary layers in microfluidic fuel cells (Yoon et al. [52]) 24

Figure 1.11 The schematic of the microfluidic fuel cell with flow-through porous electrodes fabricated by Kjeang et al. [36] 25
Figure 1.12 A Schematic diagram of the microfluidic fuel cell system with the tapered electrodes to accommodate the mixing region growth as fluids flow downstream (Bazylak et al. [8]) 26
Figure 2.1 The ”Constants” dialogue box in COMSOL Multiphysics 33
Figure 2.2 A simple Y-shaped geometry created using the GUI of COMSOL Multiphysics shows the subdomain-based electrodes and the continuity boundary separating the anode side from the cathode side. 34
Figure 2.3 The “Subdomain Settings” dialogue box of the “Incompressible Navier Stokes” application mode in COMSOL Multiphysics 36
Figure 2.4 This figure shows the boundary settings for the outlet of the channel using the “Boundary Settings” dialogue box of the “Incompressible Navier Stokes” application mode in COMSOL Multiphysics 37
Figure 2.5 This figure shows the settings for the anode subdomain using the “Subdomain Settings” dialogue box of the “Conductive Media DC” application mode in COMSOL Multiphysics 39
Figure 2.6 The “Boundary Settings” dialogue box of the “Conductive Media DC” application mode in COMSOL Multiphysics. 40
Figure 2.7 This figure shows the settings for the anode subdomain using the “Subdomain Settings” dialogue box of the “Convection and Diffusion” application mode in COMSOL Multiphysics 42
Figure 2.8 This figure shows the boundary settings for the inlet (from which fuel is introduced) using the “Boundary Settings” dialogue box of the “Convection and Diffusion” application mode in COMSOL Multiphysics 43
Figure 2.9 The “Scalar Expression” dialogue box where the Butler-Volmer equations are defined 46

Figure 2.10 The “Solver Parameters” dialogue box showing how to implement “Stationary segregated” solution procedure. 48
Figure 2.11 The “Solver Manager” dialogue box used to solve the PDEs separately is shown. Using the “Sequence” tab, it is possible to put the solvers in a desired order before solving them. 49
Figure 3.1 Verification of the proposed model against the results reported by Chang et al. [20] for a 30 mm-long channel 54
Figure 3.2 The verification of the proposed model against the experimental results reported by Choban et al. [17] 56
Figure 3.3 The effect of the channel length on the microfluidic fuel cell performance ... 58
Figure 3.4 The schematics and dimensions of different cross-section aspect ratios and electrode geometries are presented in (a), (b), (c), and (d) which are referred to the “Simple square”, “Extended square”, “Low aspect ratio” and “High aspect ratio”, respectively. The electrodes in (b), (c) and (d) are extended away from the side walls toward the centre of the channel up to the edges of the mixing region. 59
Figure 3.5 The effect of the channel aspect ratio and electrode geometry is shown. The current is normalized by the surface area. 61
Figure 3.6 The effect of the channel aspect ratio and electrode geometry is shown for the case that the current is normalized by the cell volume. 62
Figure 3.7 The oxidant concentration contour plot at two different cell voltages (600mV and 320mV) emphasizing on the loss of oxidant at the vicinity of the electrodes (depletion regions) particularly in (b) “Low aspect ratio” operating at 320mV and (d) “High aspect ratio” operating at 320mV. (a) and (c) show the oxidant concentration at 600mV. 65
Figure 3.8 Contour plots (plane at 3mm) showing the concentration gradient of the oxidant in (a) “High aspect ratio” operating at 600mV, (b) “High aspect ratio” operating at 320mV, (c) “Low aspect ratio” operating at 600mV and (d) “Low aspect ratio” operating at 320mV 66

Figure 3.9 A schematic of a microfluidic fuel cell with the third electrolyte stream (this schematic shows the velocity field in the microfluidic fuel cell). 67
Figure 3.10 The effect of inserting the third flow between the anolyte and catholyte on the polarization curve.....68
Figure 3.11 The schematic of a microfluidic fuel cell with multiple periodically-placed inlets. This schematic shows the concentration of the oxidant which is entering from the top side wall of the cell.....70
Figure 3.12 The effect of the multiple periodically-placed inlets modification on the polarization curve.....71
Figure 3.13 The schematic of a microfluidic fuel cell with tapered channel is presented. This figure shows the oxidant concentration profile in the lower half of the channel in different cross-sections along the channel.....73
Figure 3.14 A comparison of the mixing region width in the “Extended square” and the proposed tapered geometry is shown. The criterion line indicates 2% of the maximum concentration of the fuel or oxidant which is used to define the width of the mixing region.....74
Figure 3.15 The effect of tapering the channel on the polarization curve is shown. The tapered channel provides an opportunity to install more active surface areas inside the channel by reducing the mixing region width over a certain length.....75
Figure 4.1 A schematic of a microfluidic fuel cell with flow-through porous electrodes..77
Figure 4.2 The “Incompressible Navier-Stokes” application mode should be selected from the “Chemical Engineering” mode to have the porous media option (Brinkman equations).....81
Figure 4.3 Relatively low electric conductivity of porous electrodes results in non-uniform reaction rates over the entire electrode domain. This schematic depicts how this phenomena leads to more depletion near the cathode current collector. The color plot shows the oxidant concentration. 83

Figure 4.4 This figure presents the polarization curves of the microfluidic fuel cell with flow-through porous electrodes. The numerical results are in good agreement with those obtained from experiments [36].....89
Figure 4.5 The effect of the porosity on the fuel cell net power output 91

Nomenclature

A	cross-sectional area of the charge transfer
A_e	reference value for the active surface area
D	diffusion coefficient
E	reversible potential
F	Faraday constant
G	Gibbs free energy of formation
H	height of the channel
ΔH	enthalpy difference between the reactants and products
K	permeability
k_{CK}	Carman-Kozeny constant
OCP	open-circuit potential
R	universal gas constant
R_f	ohmic resistance for ionic transport
S	consumption rate of reactant species
T	cell temperature
U	average flow velocity
a	specific surface area
ai_0	exchange current density
c	local concentration of the reactants
c_0	inlet concentration
d	distance between the anode and cathode
d_f	fibre diameter
e	mole number
i	rate of the electrochemical reaction
i_f	actual current produced

i_t	current produced in case of complete oxidization of fuel
n	number of electrons transferred in the reaction
p	pressure
v	velocity
x	distance fluid travels down the channel
α	charge transfer coefficient
δ	inter-diffusion region width
ε	porosity
ε_0	reference porosity
ε_i	current efficiency of the fuel cell
ε_r	theoretical or reversible efficiency of the fuel cell
ε_v	voltage efficiency of the fuel cell
η	activation overpotential
μ	viscosity
ρ	density
σ_e	ionic conductivity of the electrolyte
σ_s	electric conductivity of the solid phase (electrodes)
σ^{eff}	effective value of the electric conductivity
ϕ_e	local potential in the electrolyte
ϕ_s	solid phase voltage

Acknowledgements

First of all, I would like to express my profound and sincere gratitude to my wonderful supervisor, Dr. Mina Hoorfar. She is such an energetic and hardworking supervisor without whose effort, patience and support, this thesis would not have been possible. Her incredible understanding, encouragement and personal guidance are deeply appreciated.

I would like to thank my advisory committee members: Dr. Homayoun Najjaran, with whom I had such a great time, and Dr. Vladan Prodanovic. Their constructive personal and academic advice has proved invaluable to me throughout the course of my studies at UBC. I would also like to thank my external examiner, Dr. Aimy Bazylak from the University of Toronto, for her willingness to fulfill this role.

I am very grateful to one of my best friends, Andrew Richards. Our countless discussions on everything from technical issues to everyday topics made this research project way more fun and of course rewarding. I would also like to thank many other friends who have enriched my life here in Canada during the past two years.

I am deeply grateful to Dr. Raisee, my Bachelor's supervisor, who has had such a great impact on my academic life that I will never forget.

My deepest and warmest thanks go to my precious parents for their constant emotional and spiritual supports. I would like to say from the depth of my heart: "Thank you mum, thank you dad for everything." I also wish to thank my understanding sisters for all of their supportive and motivational words.

Dedicated to my dear Mum, Dad and lovely sisters

1. Introduction

1.1 Fuel Cell

Fuel cells are electrochemical devices that directly convert chemical energy to electrical energy. They consist of an electrolyte medium sandwiched between two electrodes which are called anode and cathode (Figure 1.1). Fuel is delivered to the anode side and the oxidant is delivered to the cathode side. Ions generated as a result of oxidations or reductions are transported from one electrode to the other through the ionically conductive electrolyte. The electrons generated at the anode take the external circuit to the cathode, and hence the electricity is generated. The fuel and oxidant do not mix with each other at any point in the fuel cell, and no actual combustion occurs as in combustion engines. Fuel cells, unlike conventional thermal power plants, are not operating on a thermal cycle; as such they are not limited by the Carnot efficiency. However, the relevant irreversibilities and losses (explained later on this chapter) prevent fuel cells from achieving 100% efficiency. Despite these losses the fuel cell has still a great potential in replacing conventional combustion engines running on the fossil fuels [1].

In addition to large power applications, fuel cells have been considered for portable devices [2-4]. Recently, a comparison was made between the energy densities of a typical fuel cell and a lithium-ion battery [3]. The results of such a study showed that fuel cells have higher energy density and hence great potential to be used in

portable devices. This concept will be expanded more and explained in detail in Section 1.3.

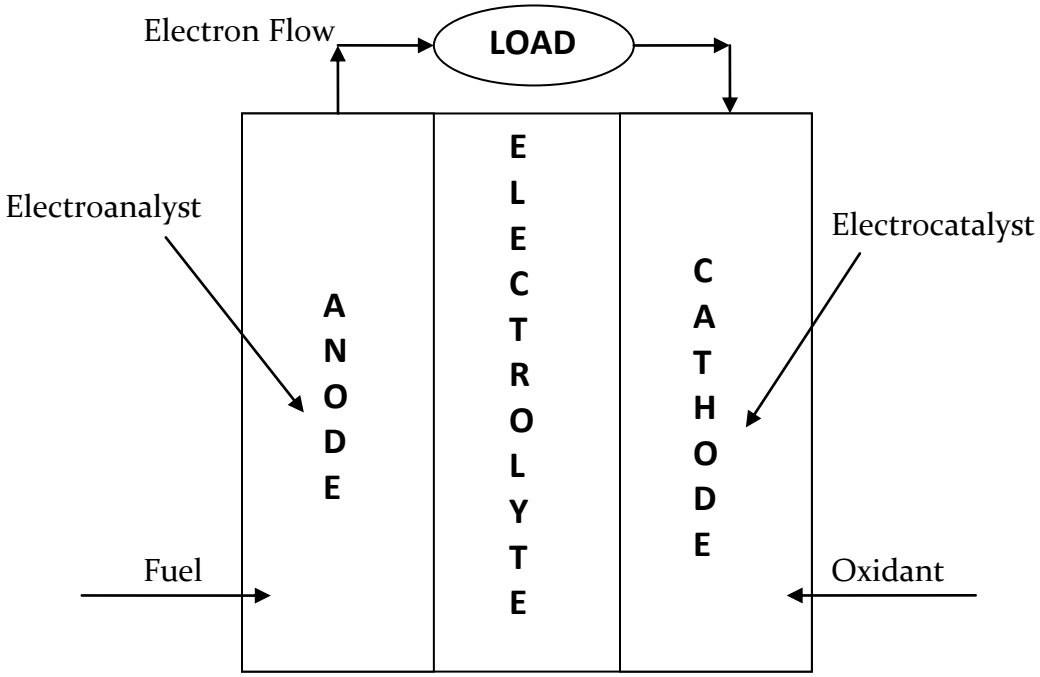

Figure 1.1 A general schematic of a fuel cell

1.2 Fuel Cell History and Classification

The concept of the fuel cell was discovered by a German scientist, Christian Friedrich Schönbein, in 1838 and published in the January 1839th edition of the "Philosophical Magazine" [2]. Based on this work, the first working prototype fuel cell was developed by a Welsh scientist, Sir William Robert Grove, using the experiment shown in Figure 1.2.

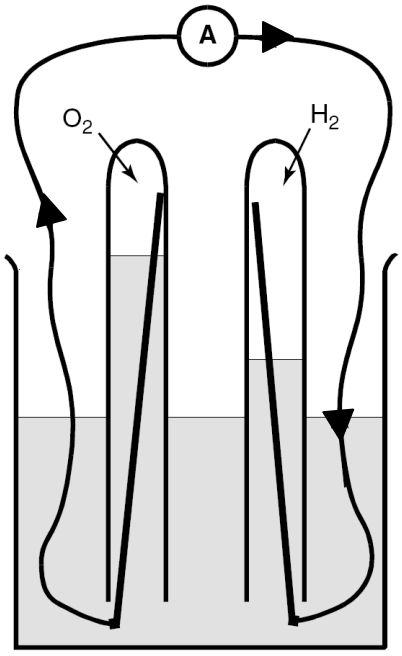

Figure 1.2 A schematic of William Grove's experiment (Hydrogen and oxygen are combined, and an electric current is produced) [5].

Since the invention of the fuel cell by Sir William Grove, researchers have investigated a wide variety of fuel cell designs in an effort to develop a power source which is practical (for widespread applications) in terms of cost, efficiency and reliability [6]. These various designs are classified in many different ways in the literature [7]. Primarily, fuel cells are classified according to the materials utilized for the electrolyte

[7]. For instance, Polymer Electrolyte Fuel Cells (PEFC) has a flexible polymer electrolyte. There is an additional level of classification which is based on the fuel used (e.g., hydrogen PEFC or direct methanol PEFC). One of the other methods to categorize fuel cells is in terms of the operating temperature range [7]. Among all these types of the fuel cell, the proton exchange membrane fuel cell (PEMFC) is the most widely developed and studied type of the fuel cell [4]. The PEMFC uses gaseous hydrogen as fuel and oxygen from the ambient air as oxidant. As it is shown in Figure 1.3, the membrane is sandwiched between the catalyst layers, gas-diffusion electrodes, and bipolar plates. Bipolar plates are used to provide high-quality cell interconnection. At the same time, they are used to feed oxygen to the cathode and fuel gas to the anode. From the bipolar plates, the reactants diffuse through the gas diffusion electrodes and react at the catalyst layers. At the anode, hydrogen molecules are split into protons (H^+) and electrons. Protons travel through the proton conducting membrane, and electrons take an external circuit toward the cathode. On the cathode catalyst, oxygen molecules react with the electrons and protons. As a result, heat and water is produced.

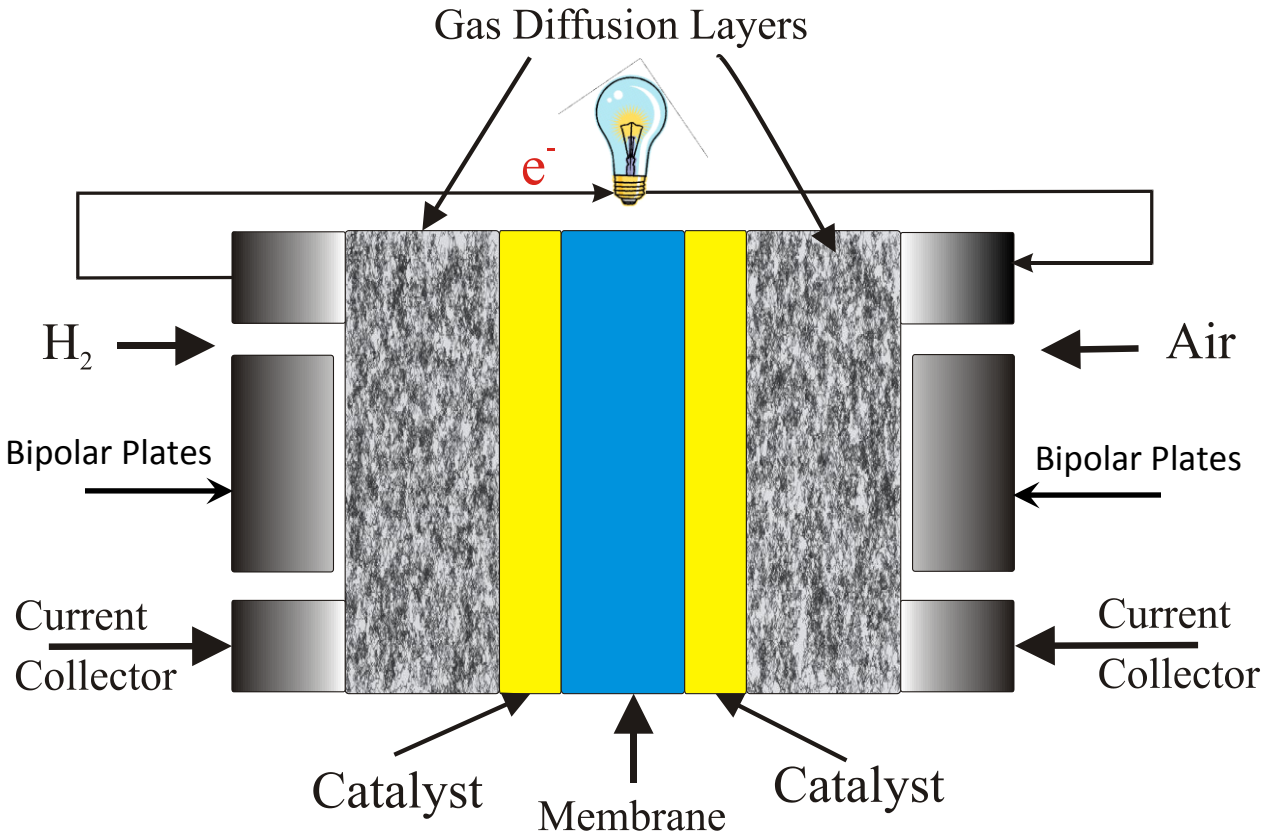

Figure 1.3 A schematic of a hydrogen-oxygen PEM fuel cell showing the membrane, catalysts and gas diffusion layers sandwiched between the bipolar plates

1.3 Miniaturization of Fuel Cells

Recently, there has been a growing demand for a small but high power source of energy for portable devices such as laptops, cell phones, global positioning systems (GPS). These devices are expected to function for long periods of time without the need for recharging [8]. The current battery technology can hardly keep up with this growing power demand [3]. Fuel cells, in general, are shown to have a large potential to perform better than the lithium-ion batteries in term of the energy density [3]. Figure 1.4 depicts this fact by comparing the energy content of a MeOH/Air fuel cell and a lithium-ion battery. This comparison shows that a fuel cell with the same energy content as a lithium-ion battery can be approximately four times smaller in volume. Because of this exceptional energy density, fuel cells have a tremendous potential to fulfill the need for compact, powerful and long-lasting power sources in portable applications.

The difference in the energy content of a fuel cell and a lithium-ion battery is growing by the volume. This growing difference indicates that fuel cells have an additional advantage by providing more compact energy sources when a higher amount of energy is required. The power density of the fuel cells can be further improved by miniaturization of the cell, which increases the surface-to-volume ratio, as the electrochemical reactions in fuel cells are surface based [9, 10].

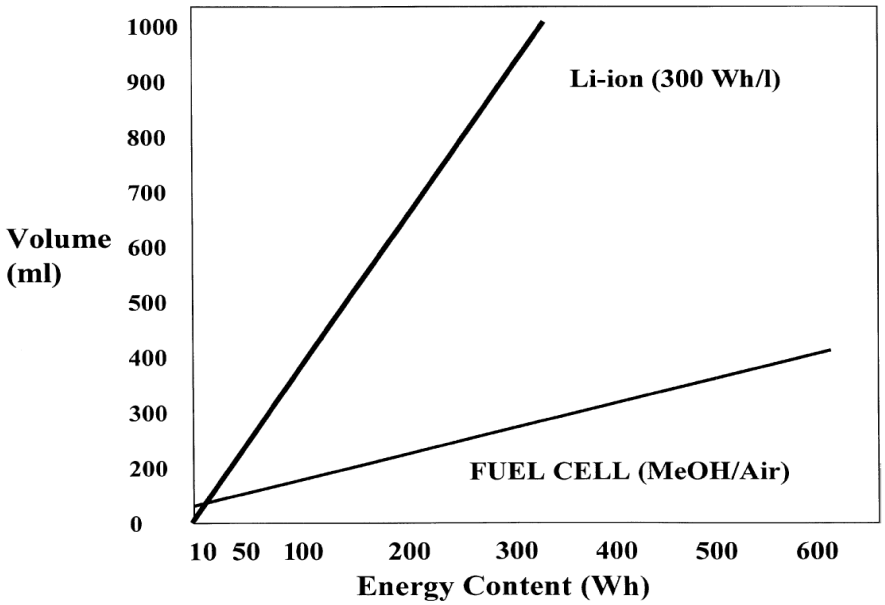

Figure 1.4 The relative advantage of fuel cells over the widely used Li-ion batteries in terms of energy density [3]

A prodigious amount of research has been conducted on the miniaturization of the conventional fuel cells [11-13]. Although the energy density of the miniaturized fuel cells increases as their size continues to shrink, several technological and mechanical challenges (including efficiency issues related to water and heat management, the ohmic overpotential caused by the membrane, and fabrication difficulties such as machining of the graphite bipolar plates) still remain [12, 14]. These challenges in addition to the increased cost and costumer safety issues [15] limit the further decrease in the size, and hence limit the increase in the power density of the miniaturized fuel cells. Because of these limitations, novel designs are required to make a miniaturized fuel cell commercially viable. The microfluidic fuel cell is an innovative design with a

great potential to overcome the current drawbacks of the miniaturized fuel cells, and become an inexpensive and reliable compact power source for practical applications.

1.4 Microfluidic fuel cell

A typical microfluidic fuel cell consists of a T- or Y-shaped microchannel (see Figure 1.5). In such systems, the fuel and oxidant are introduced in the microchannel through the two separate inlets. The aqueous anolyte and catholyte solutions travel down the channel side-by-side forming a co-laminar flow between the anode and cathode which are typically positioned on the side walls along the channel. The laminar flow in the microfluidic fuel cells maintains the separation of the fuel and oxidant and thus plays a similar role to that of the solid membrane in PEMFCs. The invention of the microfluidic fuel cell in 2002 [16] based on this concept was a significant step forward in the development of the miniaturized fuel cells because this novel design overcomes the problems and limitations imposed by the traditional miniaturized PEMFCs with the solid membrane [8]. In addition to the technical benefits of the microfluidic fuel cell, there are some cost-related advantages. For instance, the cost of fabrication and maintenance associated with the membrane is also eliminated. Microfluidic fuel cells also benefit from using liquid fuels which have higher energy densities as opposed to the gaseous fuels used in typical PEMFCs [3].

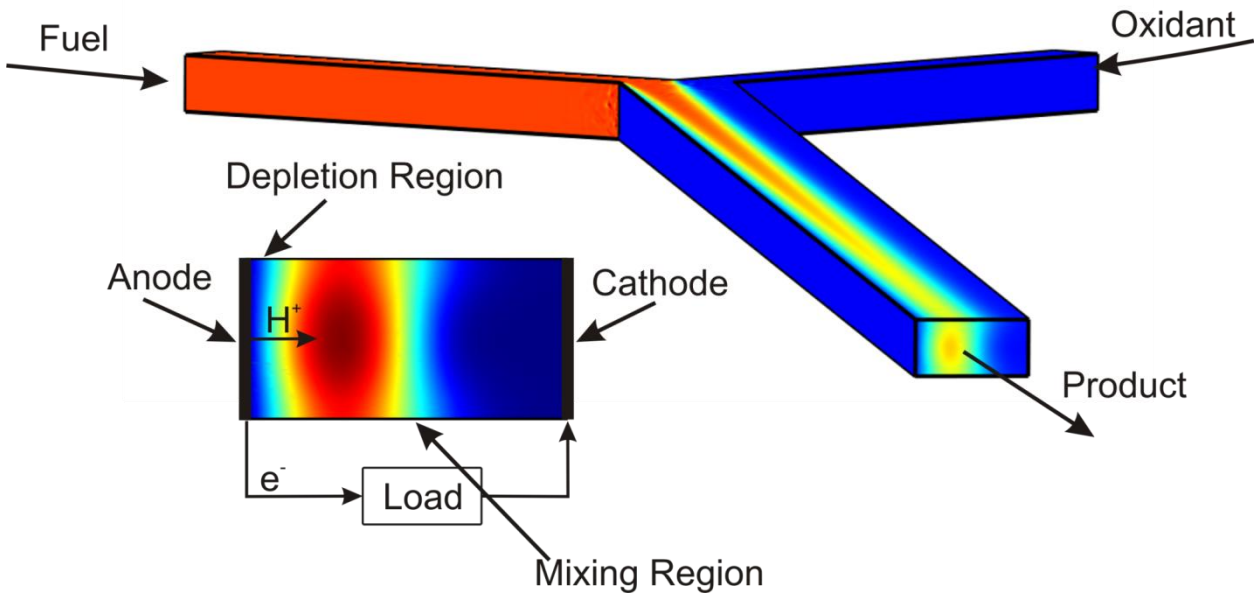

Figure 1.5 This figure shows a typical Y-shaped microfluidic fuel cell with the plot of fuel concentration over the entire fuel cell domain. Fuel and oxidant are introduced from the two inlets of the channel. They are flowing together side-by-side forming a co-laminar flow. Electrons and protons are produced on the anode. Protons travel through the electrolyte and electrons take the external circuit toward the cathode. Protons and electrons meet oxidant species on the cathode to complete the reduction reaction and generate electricity.

Mixing Region

As the anolyte and catholyte travel toward the outlet of the channel, the laminar nature of the flow prevents convective mixing of the two solutions and keeps the fuel and oxidant largely on their own sides of the channel. However, diffusion in a direction transverse to the flow creates a thin region around the liquid-liquid interface in the middle of the channel where the solution contains both fuel and oxidant. This region is called mixing region shown in Figure 1.6. The thinner the mixing region the better the performance of the device. A thin mixing region indicates better fuel/oxidant separation which provides each side (anode and cathode) with more available reacting species. In

other words, the mixing region limits the amount of the reactants that can be potentially available to the electrodes. This also limits the extension of the electrodes from the wall toward the middle of the channel (which is desirable since it increases the active surface area) due to the cross-over issue (i.e., reactants reaching the wrong electrode) [8]. Basically, if the electrodes are extended to overlap with the mixing region, fuel crossover results in a mixed potential (which tends to lower the equilibrium electrode potential) at the cathode and hampers the fuel cell performance [17].

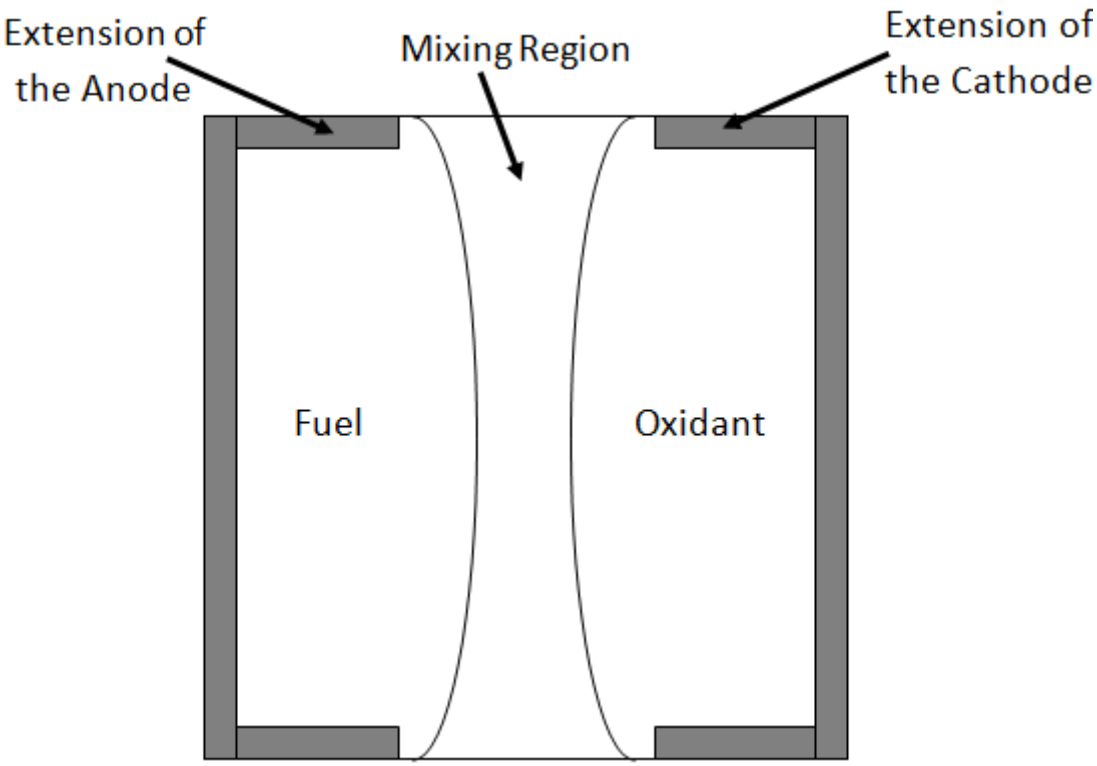

Figure 1.6 This figure shows the extension of the electrodes up to the point that they do not reach to the mixing region to avoid fuel crossover.

The transport of the reactants is predominantly by convection along the channel and mainly through diffusion across the channel. Thus, the mixing region thickness can be controlled by changing the fuel and oxidant flow rate which changes the relative

rates of streamwise and transverse mass transport. This ratio of convective to diffusive mass transport is commonly quantified in terms of the Peclet number (i.e., $Pe = UH/D$) [17]. By increasing the inlet velocity, the Peclet number increases which means that the rate of the transverse diffusion is becoming much less than the streamwise convection. In other words, the time that the fuel/oxidant species are in diffusional contact is reduced. Thus, the reactants have less time to diffuse to the other side of the channel which leads to a thinner mixing region.

The mixing region is wider at the top and the bottom (see Figure 1.6). This phenomenon is due to a lower velocity at the vicinity of the walls which increases the duration of the diffusional contact between the anodic and cathodic streams and causes the mixing region to take on an hourglass shape. The maximum width of the mixing region (δ) which occurs at the wall is experimentally demonstrated [18] to scale as the one-third power of the axial distance, x, along the channel and inversely as the one-third power of the average flow velocity. The following expression represents the calculated width of the diffusive mixing region at the walls of the fuel cell [18, 19]:

$$\delta \approx \left(\frac{DHx}{U}\right)^{1/3} \tag{1-1}$$

where, x represents the distance that the fluid travels down the channel, D, H and U are the diffusion coefficient, the height of the channel and the average flow velocity, respectively. The exact extent of this inter-diffusion interface can be theoretically quantified by solving the convection-diffusion equation for the steady-state transport of

chemical species assuming that the Peclet number is high so the diffusion along the channel can be neglected compared to the convection.

Depletion Layer

The concentration of the fuel and oxidant at the electrodes is reduced to zero indicating that the electrochemical reaction rates are much faster than the diffusion rates [8]. This fast rate of consumption of the reacting species at the electrodes results in the development of a concentration boundary layer (CBL) shown in Figure 1.5. The CBL or depletion layer formed at the vicinity of the electrodes acts as a resistance for the reactants to reach to the active surfaces. This hampers the electrochemical reactions and eventually affects the performance of the fuel cell adversely. To enhance the reaction rates and improve the performance, a steeper concentration boundary layer (which drives larger flux of the reactants) is required. Running the microfluidic fuel cell with higher Peclet number (i.e., higher inlet velocity) will press the CBL against the electrodes which leads to a steeper depletion layer. Although higher inlet velocities results in faster replenishment of the depleted areas, there is an upper limit before the hydrodynamic instabilities occurs [17, 20]. These hydrodynamic instabilities include the small perturbations which happen at very high flow rates and cause the electrolyte streams oscillate and occasionally touch the opposite electrode [17].

1.4.1 Fundamental Principles in Microfluidic Fuel Cells

Open Circuit Potential

The electromotive force (EMF) or reversible open-circuit potential (OCP) of a microfluidic fuel cell is defined as follows:

$$E = -\frac{\Delta G}{nF} \tag{1-2}$$

where ΔG denotes the difference between the Gibbs free energy of formation of products and reactants, F represents the Faraday constant and n is the number of electrons transferred for each molecule of the fuel. The negative sign means that the energy is released. It should be noted that the Gibbs free energy of formation is not constant and it varies with the temperature. Microfluidic fuel cells are low-temperature fuel cells and their working temperature is usually assumed to be equal to the ambient temperature.

In an ideal microfluidic fuel cell, the cell voltage is independent of the current drawn. However, due to some irreversibilities (losses) this ideal behaviour is never observed in practice: The cell voltage drops as more current is drawn from the cell (see the next section). Even under the open-circuit conditions (zero current), the reversible cell voltage calculated by Eq. (1-2) is not realized primarily because of sluggish reaction kinetics which could be due to the low probability of a molecule having enough energy to overcome the "energy hill" [5]. The classical visualization of the "energy hill" is presented in Figure 1.7. It shows that the reacting molecules must gain a specific

amount of energy and reach a minimum energy level before they can react with each other, produce new molecules and release energy. To increase the probability of a molecule having enough energy to get over the "energy hill", there are three possible ways: 1) raising the temperature, 2) using of a catalyst (such as Platinum), and 3) increasing the active surface area [5]. The first one is not desirable for microfluidic fuel cells; however, the last two (specially the last item) are used to enhance the reactions in such devices.

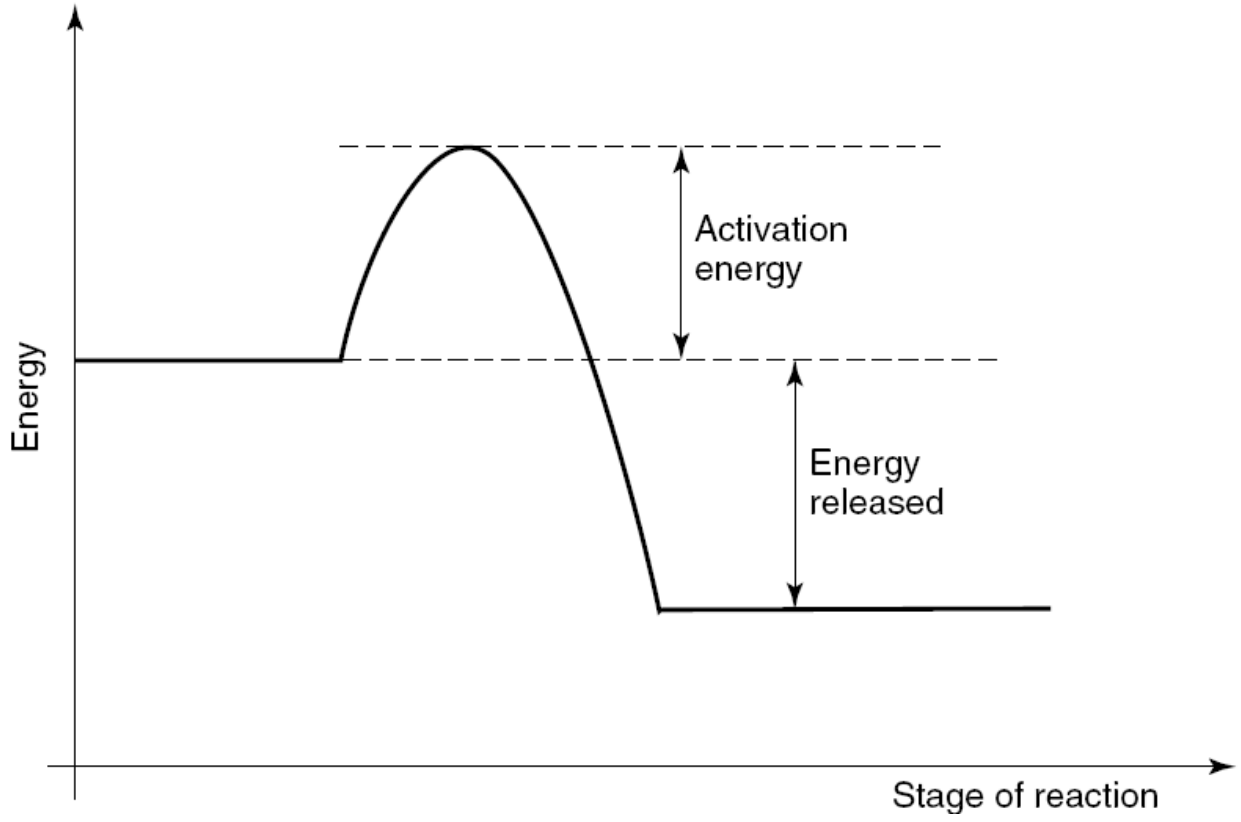

Figure 1.7 The Classical Energy diagram for a simple chemical reaction showing the energy hill [5]

Different fuels have different OCP. There are various types of fuels which have been used in the microfluidic fuel cell including hydrogen dissolved in different

electrolytes [21-23], methanol [24-27], formic acid [17, 28-34], vanadium redox species (V(III)/V(II)) [19, 35-37], and hydrogen peroxide [38]. Among different fuels formic acid is one of the most repeatedly-used fuels with high energy density. Formic acid has been used in both PEM-based fuel cells [39-42] and microfluidic fuel cells [17, 28, 29, 31], and it is electrochemically more active than many other fuels such as methanol [40]. Formic acid releases electrons and produces protons at the anode through the electrochemical reaction shown below:

$$HCOOH \rightarrow CO_2 + 2H^+ + 2e^- \quad (1\text{-}3)$$

The reversible OCP for the formic acid can be calculated as follows:

$$E = \frac{-\Delta G}{nF} = \frac{285500}{2 * 96485} = 1.48\,V \quad (1\text{-}4)$$

The actual OCP of the formic acid is however lower than the theoretical value calculated above by a considerable amount: the sluggish electrochemical reaction kinetics particularly at the cathode accounts for an approximately 500 mV overpotential loss in the room temperature [7, 17, 20].

Overpotential Losses

The performance of a fuel cell is generally demonstrated by a polarization curve which shows the cell voltage at different current densities. Figure 1.8 shows a typical polarization curve of a fuel cell depicting three different regions each of which is dominated by one important irreversibility.

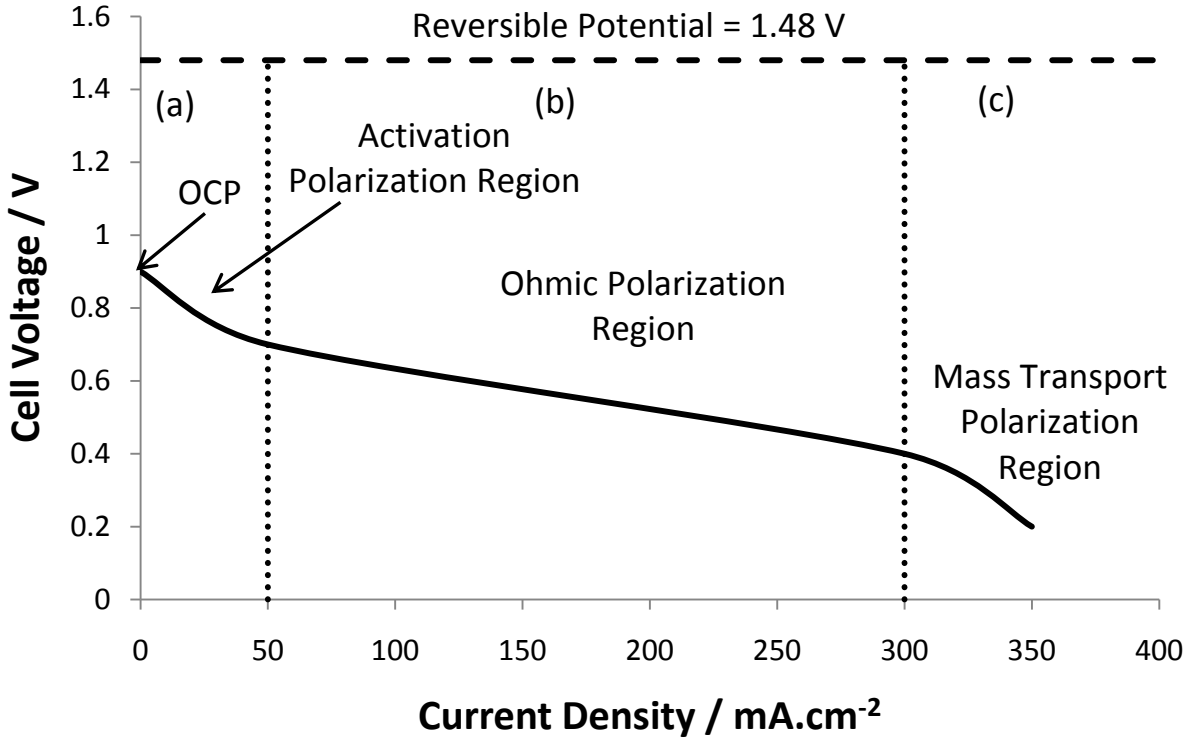

Figure 1.8 A typical polarization curve for a direct formic acid fuel cell is shown. Three main polarization regions are demonstrated.

The potential loss in Region (a) is mainly due to the activation polarization. Activation overpotential is an irreversibility associated with the activation energy needed for initiation of the reaction. This is primarily caused by the sluggishness of the electrochemical reactions at low current densities. The next loss (shown in Region (b)) is associated with the proportion of the energy consumed to transfer the electrons to or from the electrodes. Region (b) is mainly dominated by the ohmic polarization; however, there is still a small contribution from the activation loss. Basically, the ohmic overpotential consists of: 1) resistance to proton transfer in the electrolyte, and 2) other electrical resistance from the different components of the cell such as electrodes, wiring

and the contact points (i.e., where the wires are attached to the electrodes). The ohmic resistance for ionic transport in the electrolyte is expressed as follows [16]:

$$R_f = \frac{d}{\sigma_e A} \tag{1-5}$$

In this equation, R_f is the ohmic resistance for ionic transport, d represents the distance between the anode and cathode, σ_e refers to ionic conductivity and A is the cross-sectional area of the charge transfer.

In Region (c), high current densities are drawn from the cell indicating that the electrochemical reaction rates are high. High reaction rates mean high reactant consumption rates which make the regions around the electrodes depleted from the reacting species. This is called mass transport polarization meaning the inability of the reacting species to reach to the active sites fast enough to support the applied load. This issue can be alleviated to some extent by introducing a higher flux of reactants. The voltage drop in Region (c) is mainly due to the mass transport issue with small contributions from ohmic and activation polarizations.

Efficiency

In general, fuel cells are known to be more efficient compared to the conventional thermal power plants because their efficiency is not limited to the Carnot cycle efficiency. The anodic and cathodic electrochemical reactions for the microfluidic fuel cells using formic acid as the fuel are represented below:

Anode: $$HCOOH \rightarrow CO_2 + 2H^+ + 2e^-$$ (1-6)

Cathode: $$O_2 + 4H^+ + 4e^- \rightarrow 2H_2O$$ (1-7)

The operating efficiency of the fuel cells in general and microfluidic fuel cells in particular are lower than the theoretical values due to losses including activation, ohmic and mass transport overpotentials (explained in the previous section). However, all the available energy from the above reactions can be converted to the electrical energy in an ideal process. Considering that ΔH is the total energy available from the process and ΔG is a portion that can be theoretically converted to the electrical energy, the theoretical or reversible efficiency of the fuel cell reaction is then expressed as:

$$\varepsilon_r = \frac{\Delta G}{\Delta H} \quad (1\text{-}8)$$

Here, the absolute value of ΔG is generally less than the enthalpy change, ΔH.Theoretically, however, the opposite could happen. In fact, for a reversible situation where the entropy of the products is higher than the reactants, the system (i.e., the fuel cell) can actually absorb heat from the surroundings and use this heat to do work on the surroundings (generate electricity). Thus, the magnitude of ΔG will be greater than the magnitude of ΔH. Thus, maximum efficiencies greater than 100% are theoretically possible [17].

As it has been stated before, the cell voltage of a working fuel cell is always lower than the reversible potential value due to the fuel cell losses. This leads to the introduction of another term called voltage efficiency which is expressed as follows:

$$\varepsilon_v = \frac{E(i)}{E} \tag{1-9}$$

where $E(i)$ is the cell voltage at a given current density and E is the reversible potential.

Current efficiency is another type of efficiency which affects the total efficiency of a working fuel cell. This efficiency comes into effect due to incomplete oxidation (consumption) of the fuel at the anode. The current efficiency is defined as:

$$\varepsilon_i = \frac{i_f}{i_t} \tag{1-10}$$

where i_f is the current produced in the case which not all of the fuel reactants are oxidized at the anode, and i_t is the current produced in the case of complete oxidization of the fuel reactants at the anode.

The overall efficiency of a working fuel cell is then defined as the product of all of the above efficiencies:

$$\varepsilon = \varepsilon_r \varepsilon_v \varepsilon_i \tag{1-11}$$

1.4.2 Contributions and Technical Advances in Microfluidic Fuel Cells

The first co-laminar microfluidic fuel cell introduced by Choban et al. [17] in 2002 consisted of a Y-shaped microchannel in which an aqueous fuel stream and an aqueous oxidant stream were flowing side-by-side. Formic acid was selected as the fuel and the saturated oxygen solution was chosen as the oxidant. After this first demonstration, there had been numerous developments of the microfluidic fuel cell design based on different fuels (explained in the previous section) and oxidants including the most commonly-used one like oxygen in aqueous or gaseous form [17, 21-23, 25-27, 29-31, 43-45], hydrogen peroxide [24, 28, 30, 38], vanadium redox couple (V(IV)/V(V)) [19, 35-37], potassium permanganate [17, 33, 34] and sodium hypochlorite [32]. In addition to the attempts made in the design of different cells by changing the fuel and oxidant species, there has been significant contributions in the enhancement of the microfluidic fuel cell performance by targeting and ameliorating the limitations caused by phenomena like the growth of the mixing region, which can cause fuel crossover if it reaches to the electrodes, and the formation of the concentration boundary layer (CBL), which hampers the mass transport. Both numerical and experimental approaches were taken to study the effect of different elements (including different channel geometries, electrode structures, and utilization of various types of fuels and oxidants) on the performance of the microfluidic fuel cell. These contributions are categorized in the following subsections.

1.4.2.1 Experimental Contributions

Low Concentration of Oxygen in the Cathodic Stream

In the first microfluidic fuel cell [17], the saturated oxygen solution was used as oxidant. The power density of the cell was relatively low (around 0.2mW.cm^{-2}) [17, 26]. This low power density was primarily due to low solubility and diffusivity of oxygen in the cathode side, and the CO-poisoning effect of formic acid oxidation in the anode side. The issue of the low solubility of oxygen in the cathode side was resolved using potassium permanganate which has a higher solubility in aqueous media [17]. In that work, the anode poisoning issue was addressed by depositing adatoms of Bi onto Pt [26].

An innovative solution to resolve the problem associated with the low concentration of the oxygen in the cathodic stream was proposed by Jayashree et al. [29] who incorporated a gas permeable cathode to enable the cell to access to the surrounding air (see Figure 1.9). In their work, the integration of an air-breathing porous cathode allows for penetration of gaseous oxygen from the ambient air. This source of oxygen has four orders of magnitude higher diffusivity and several times higher concentration (10mM) than dissolved oxygen in the aqueous medium [16, 29]. With this configuration a peak power density of 26mW.cm^{-2} was achieved when 1M formic acid in 0.5M sulfuric acid is used as the fuel.

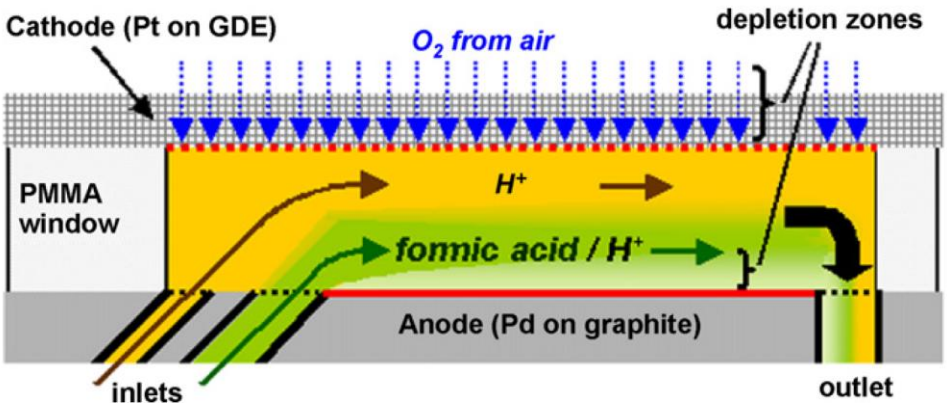

Figure 1.9 A schematic of an air-breathing microfluidic fuel cell with porous cathode structure is shown (Jayashree et al. [29]). Oxygen is captured from the ambient air through the porous cathode.

Another solution to resolve the issue regarding the oxidant low concentration is the use of liquid oxidant. There are numerous liquid fuels with high energy densities; however, the use of liquid oxidants is not common except for hydrogen peroxide [46-48]. The only problem with the use of hydrogen peroxide is the oxygen gas evolution which causes instability issues leading to fluctuation of OCP [30]. There are, however, some remedies proposed to alleviate the stability issue. Aogaki et al. [49] proposed the use of induced magnetic field to separate the streams. Sun et al. [33] introduced the third electrolyte to the channel to promote the anolyte and catholyte separation. (III) Kjeang et al. [28] reported a microfluidic fuel cell functioning based on formic acid and hydrogen peroxide with a grooved microchannel design to capture the oxygen bubbles produced from the reactions. Gu et al. [50] has reported gold as an alternative catalyst for hydrogen peroxide reduction which minimizes gas evolution while providing high current density.

The alternative strategy to solve the oxygen low concentration problem without having to deal with the stability issue is to use the vanadium redox species (i.e., V^{2+}/ V^{3+} and VO^{2+}/ VO_2^{+}). Vanadium redox couples provide many benefits to the fuel cell: they have high solubility, and hence, they can provide a solution with relatively high concentration of reacting species (up to 5.4 M) [51]. They also produce high OCP (up to 1.7 at uniform PH), and do not need expensive metal catalysts to start the oxidation and reduction reaction.

Enhancement of Reactant Transport to the Electrodes

Diffusion is the main transport mechanism for the reacting species to reach the electrodes. Therefore, the low diffusion coefficient of the reactants in the microfluidic fuel cells leads to slow replenishment of the depleted regions (i.e., CBL). The electrochemical reactions can be impeded by slow replenishment of the depletion layer. To improve the CBL replenishment and eventually enhance the fuel cell power density, Yoon et al. [52] proposed three different strategies to control actively the CBLs (Figure 1.10). In the first proposed strategy, the consumed species are removed by multiple outlets placed periodically. In the second strategy, more reactants were added through multiple periodically placed inlets. Finally, in the third strategy, a secondary transverse flow was generated by creating topographical herringbone patterns on the channel walls [16]. The last approach is beneficial to fuel utilization of the microfluidic fuel cell by enhancing the cross-stream transport of the reactants. However, it must be used

cautiously as it can increase the mixing rate of the fuel and oxidant which would lead to sever crossover problems.

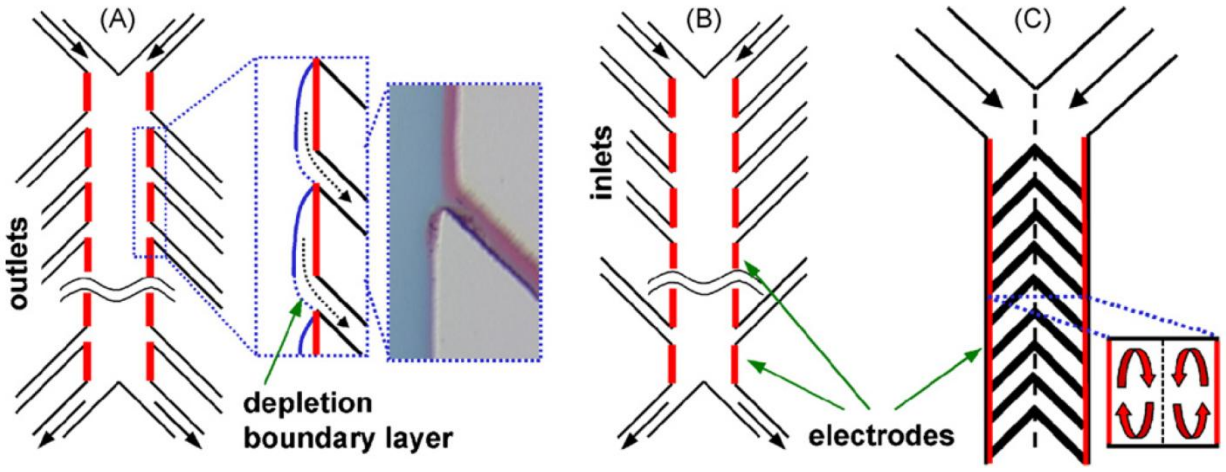

Figure 1.10 Three different strategies for the active control of concentration boundary layers in microfluidic fuel cells (Yoon et al. [52])

Lim and Palmore [53] suggested a passive boundary layer control through splitting the electrodes into smaller units separated by a gap. They reported a 25% improvement in the maximum current density when a single pair of electrode is split to two pairs of electrodes while the total active surface area is kept constant. The overall current density of the cell was not however improved since the geometrical surface area required for the gap did not contribute in any current generation.

Replacing the conventional solid electrodes with porous electrodes is another method proposed for enhancing reactant transport as it increases the available active surface area to the reactants. The flow-through porous electrode design suggested by Keang et al. [36] has the advantage of having high fuel utilization and producing high cell voltages at the same time. This design (shown in Figure 1.11) is based on cross-

flow of aqueous vanadium redox species through the electrodes into an exit channel, where the waste solutions meet and establish a co-laminar flow. This co-laminar flow of reacted species facilitates ionic charge transfer in a membraneless configuration.

Figure 1.11 The schematic of the microfluidic fuel cell with flow-through porous electrodes fabricated by Kjeang et al. [36]

1.4.2.2 Numerical Modeling Advances in Microfluidic Fuel Cells

The first 3D computational model was developed by Bazylak et al. [8] to analyze a T-shaped microfluidic fuel cell. They tested three different channel cross-sections with different aspect ratios, obtained the fuel and oxidant distribution, and calculated the fuel utilization value. They found that the rectangular cross-sections have higher fuel utilization compared to the square one. The numerical simulation results also suggested the implementation of a tapered electrode design to take into account the growth of the co-laminar mixing region in the downstream direction (see Figure 1.12) [8]. After the first attempt, an extensive numerical and theoretical analysis of microfluidic fuel cells has been conducted by Chang et al. [20] and Chen et al. [54]. In their work, complete polarization curves were obtained by modeling the electrochemical reaction kinetics with the Butler-Volmer expression. The results of their model were in agreement with the experimental studies [17, 26]. The results also confirmed that the cell performance is 1) limited by the cathodic mass transport rate and 2) independent of the anodic

concentration. Chen et al. [55] also developed a 2D computational model of cathode kinetics under the co-laminar condition. Their results recommended high Peclet number, high oxygen concentration, thick cathode catalyst layer and high aspect ratio geometry to improve the performance.

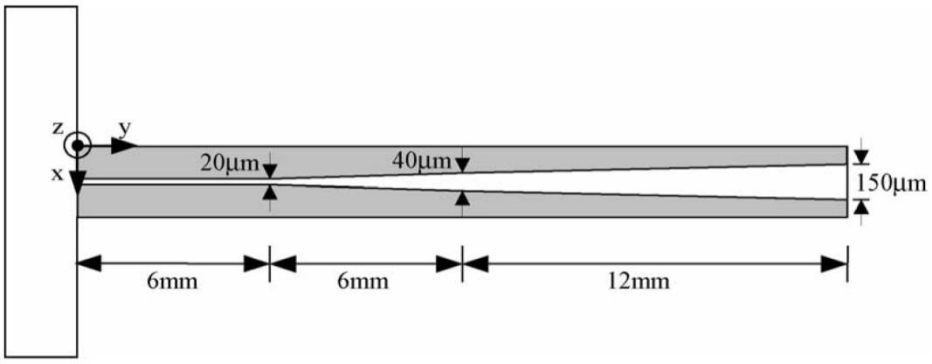

Figure 1.12 A Schematic diagram of the microfluidic fuel cell system with the tapered electrodes to accommodate the mixing region growth as fluids flow downstream (Bazylak et al. [8])

Chen et al. [54] also developed a numerical simulation to model the microfluidic fuel cell using hydrogen peroxide as both fuel and oxidant in mixed media [38]. This model was also based on the Butler-Volmer electrochemical reaction kinetics. The developed model was used to study the effects of the species transport and geometrical design. The numerical results were invariant at flow rates above 0.1mL.min^{-1}. This shows that there were no mass transport limitations in the cathode. It should be mentioned that the oxygen bubbles produced from hydrogen peroxide decomposition were not considered in that study.

1.4.3 Challenges and Opportunities

Microfluidic fuel cells have potential to address the low power density issue of the currently existing power sources used particularly in the context of portable applications. As it has been mentioned earlier, the reactions in fuel cells are surface-based. Thus, the power density of a fuel cell can be enhanced by miniaturization which increases the surface-to-volume ratio. There are, however, some power density-restricting and performance-limiting concerns associated with the microfluidic fuel cell which remain to be resolved. Some of these problems are low fuel utilization which is resulted from insufficient mass transport to the electrodes, sluggish electrochemical kinetics which can cause low OCP, and ohmic resistance which can adversely influence the amount of the current density that could be achieved. These issues along with suggested solutions are separately discussed below.

Electrochemical Kinetics

The activation overpotential which is the main cause of the deviation of OCP from its reversible value is due to the sluggish electrochemical reactions. Choosing appropriate catalysts and increasing the overall active surface area of the electrodes are the two most effective solutions to address the issue regarding the slow electrochemical reactions. Increasing the operational temperature is an alternative method to enhance the chemical reactions, but it is not practical for the microfluidic fuel cells. An appropriate choice of the electrolyte media with the desired pH value could also affect the electrochemical kinetics.

Ohmic Resistance

Ohmic resistance is another problem contributing to the cell overpotential. Overall ohmic losses are directly proportional to the cell current in the microfluidic fuel cells, and hence, are acting as a special barrier to devices which operate at high current densities. The ohmic resistance in the microfluidic fuel cells is generally higher than that observed in the membrane-based fuel cells due to a larger separation of the electrodes in microfluidic fuel cells [16]. This fact reveals the importance of further attention to this power density-restricting issue. The ohmic resistance in the microfluidic fuel cell is a combination of the ionic charge transfer resistance and the electrical resistance of the electrodes and wirings. Increasing the concentration of the supporting electrolyte and decreasing the average species travel distance between the electrodes can contribute to a large reduction in the electrolyte ohmic resistance. Introducing a strong electrolyte with high ionic concentration as the 3rd electrolyte stream between the anolyte and catholyte can also reduce the overall electrolyte resistance. However, Sun et al. [33] showed that the flow rate of this middle stream must be chosen carefully as it can adversely affect the OCP. They demonstrated that the open circuit potential first increases and then decreases with the flow rate of the 3rd stream. It is also shown that the short circuit current decreases rapidly after a short increase in the 3rd stream flow rate in the beginning. Thus, taking both the potential and the current into account, there is an optimum flow rate with which the maximum performance can be achieved. Apart from the solution resistance, electrical resistance in the solid part of the microfluidic fuel

cell should be minimized by, for instance, incorporating highly conductive current collectors.

Mass Transport

The mass transport issue is one of the main power-limiting problems preventing the microfluidic fuel cell from achieving high power densities at high current densities. Reacting species transport from the bulk to the electrodes primarily occurs through diffusion and convection. In the typical design of the microfluidic fuel cells in which the electrolyte is flowing over the electrodes, reactants are conveyed by convection from the inlet to the vicinity of the electrodes. Afterwards, they reach to the electrodes through diffusion. In these systems, increasing the reactant concentrations and the mean flow velocity, and reducing the width of the channel (which helps the reactant molecule travel less to reach the active site) will improve mass transport [17]. Choosing reactant species with higher diffusivity can also alleviate the mass transport issue [16].

1.5 Motivation and Layout of the Thesis

Motivation

The microfluidic fuel cell technology would greatly benefit from further theoretical and numerical modeling. These simulations can be used to study the effects of various geometrical modifications and electrochemical and flow parameters on the performance and the power density of the microfluidic fuel cell. Numerical modeling can also be used to determine the significant parameters and to optimize them for a better performance without conducting lengthy and extensive experiments. Despite all these facts, only a few studies [8, 20, 54-58] involving numerical modelling have been reported so far.

Layout of the Thesis

In this thesis, a 3-D numerical model of a Y-shaped microfluidic fuel cell containing the flow kinetics, species transport, and electrochemical reactions within the channel and the electrodes is developed and implemented in COMSOL Multiphysics 3.5. The model is then verified against the experimental results previously reported in the literature [17]. Afterwards, the verified and validated model is used to assess the effect of different modifications which have been implemented in the microfluidic fuel cell since its advent. The effect of these modifications on the cell performance is investigated through polarization curves and calculation of fuel utilization. With the simulation developed in this research, the effects of 1) the channel geometry aspect ratio and electrode configuration, 2) the third flow inserted between the anolyte and catholyte in the channel (i.e., multi–stream laminar flow), and 3) the multiple periodically

placed inlets, on the microfluidic fuel cell performance are studied. Finally, a novel design of the microfluidic fuel cell, consisting of a tapered channel, is suggested and compared to the non-tapered geometry through the polarization curves.

The thesis has been organized as follows: In Chapter 2, the steps which have been taken in COMSOL to obtain these polarization curves are clearly and thoroughly explained. The ‘‘Navier Stokes’’ module is used to model the pressure-driven laminar flow inside the channel. The Butler-Volmer equation was implemented to incorporate the electrochemical reactions at the electrodes. The ‘‘Conductive Media DC’’ module of COMSOL is used to model the electric fields within the fuel cell. In Chapter 3, the results of the model including the Polarization (I-V) curves for each modified microfluidic fuel cell are presented. In this chapter, the oxidant concentration and concentration gradient contour plots of high and low aspect ratio geometries at two different operational cell voltages are obtained and compared. Finally, the results of the proposed tapered geometry are presented. A Comparison of the mixing region width in the ‘‘Extended square’’ and the proposed tapered geometry is shown and the effect of tapering the channel on the polarization curve is demonstrated. Chapter 4 presents, the numerical modeling of a microfluidic fuel cell with flow-through porous electrodes. The effect of the inlet velocity and the electrode porosity is shown. Conclusions and suggested ideas for future work are presented in Chapter 5.

2. Modeling Steps in COMSOL

In this work, a theoretical model of the microfluidic fuel cell is developed using a commercial CFD package, COMSOL Multiphysics. This model is developed to account for the fluid flow kinetics, species transport, and electrochemical reactions at the electrodes with appropriate boundary conditions. The governing partial differential equations (PDEs) describing the physics of the fuel cell operation are solved by COMSOL using finite element (FEM) numerical techniques for the spatial discretization. In this chapter, a clear and step-by-step implementation of the COMSOL modules (application mode) used to obtain the polarization curves is presented.

2.1 Constants

After creating the fuel cell geometry using the graphical user interface (GUI) of COMSOL Multiphysics, the values of various parameters such as, electrolyte density and viscosity, open circuit potential are entered in the ‘‘Constants’’ dialogue box which is in the ‘‘Options’’ menu.

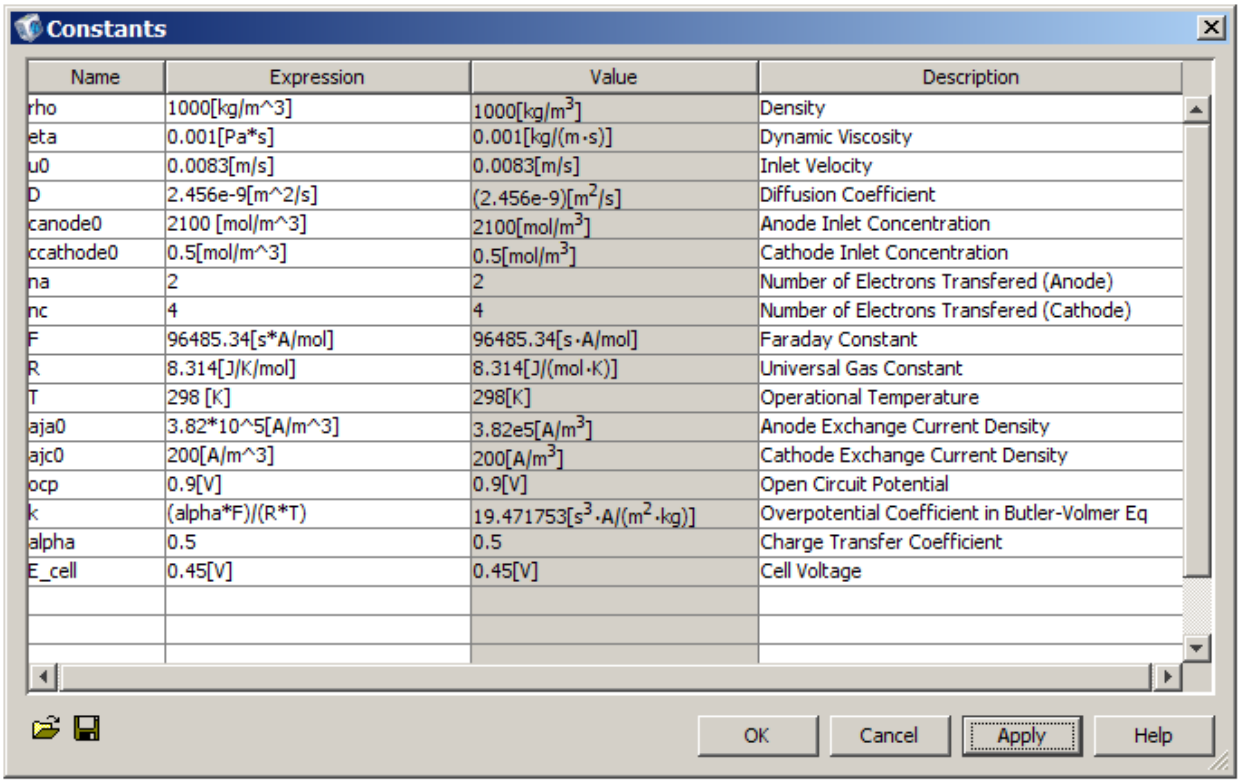

Figure 2.1 The ”Constants” dialogue box in COMSOL Multiphysics

As it is shown in Figure 2.2, the electrodes are introduced as very thin subdomains at the vicinity of the channel side walls. This method is implemented because it is found that modeling with subdomain-based electrodes converges more readily compared to the case where the electrodes are considered as boundary conditions. This approach has been practiced for modeling of microfluidic fuel cells in the past [20].

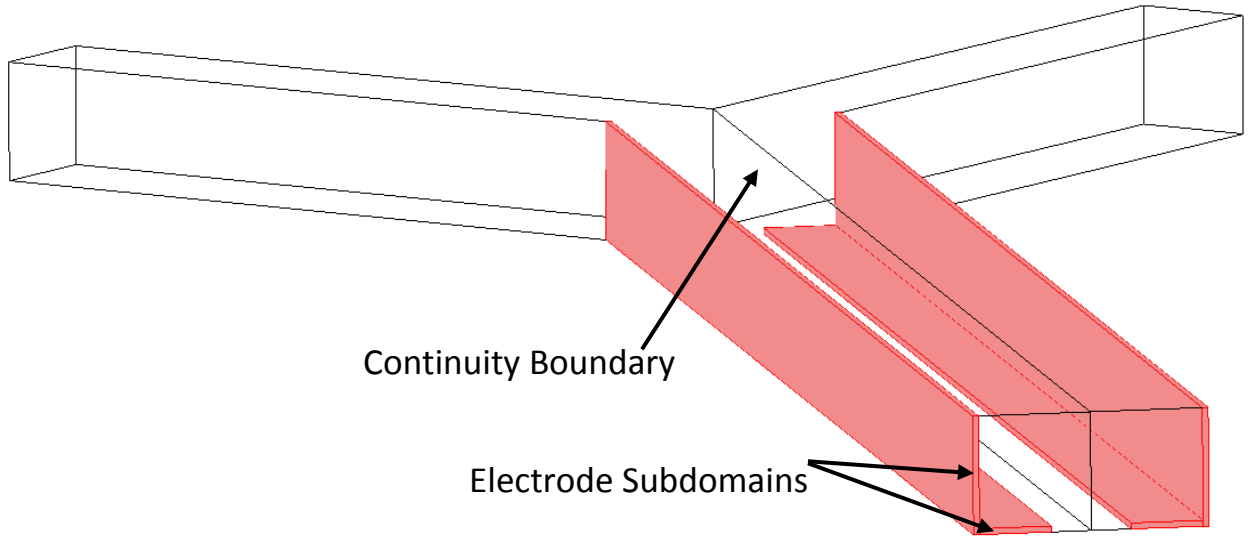

Figure 2.2 A simple Y-shaped geometry created using the GUI of COMSOL Multiphysics shows the subdomain-based electrodes and the continuity boundary separating the anode side from the cathode side.

In addition to the continuity boundary shown in Figure 2.2, there are continuity boundaries between the electrode subdomains and the bulk of the channel for all but the "conductive media DC" solid-phase application mode. Details on boundary settings are provided in Section 2.3.

2.2 Fluid Flow

Microfluidic flows are characterized by low Reynolds numbers due to the small dimensions of microchannels and low fluid velocities. For this reason, the flow is expected to be laminar and can be assumed to be incompressible. Also, in a typical micro-scale flow, the body forces such as the fluid weight are dominated by surface forces such as viscous shear stress. Applying mass and momentum conservation in a differential form allows the velocity field to be described by the Navier-Stokes and continuity equations [59].

$$\nabla . v=0 \tag{2-1}$$

$$\rho(v . \nabla v)=-\nabla p + \mu\nabla^2 v \tag{2-2}$$

In these equations, v and p are the velocity and pressure, respectively. ρ and μ represent the density and dynamic viscosity which are both assumed to be equal for the two streams and constant over the whole domain. These equations can be implemented using the steady-state, laminar "Incompressible Navier-Stokes" application mode (module) of COMSOL Multiphysics. The flow was assumed to continue into the electrode subdomains. The no-slip boundary condition was applied to all of the channel walls. To reduce the memory required for the simulation, only half of the channel geometry is model. At the symmetry plane defining the top or bottom of the model geometry, a symmetry boundary was applied. A constant velocity was applied to the inlets, and the outlet was assumed to discharge to the atmospheric pressure.

Figures 2.3 and 2.4 show the subdomain and boundary settings for the ‘‘Incompressible Navier-Stokes’’ module. These settings are available in the ‘‘Options’’ menu.

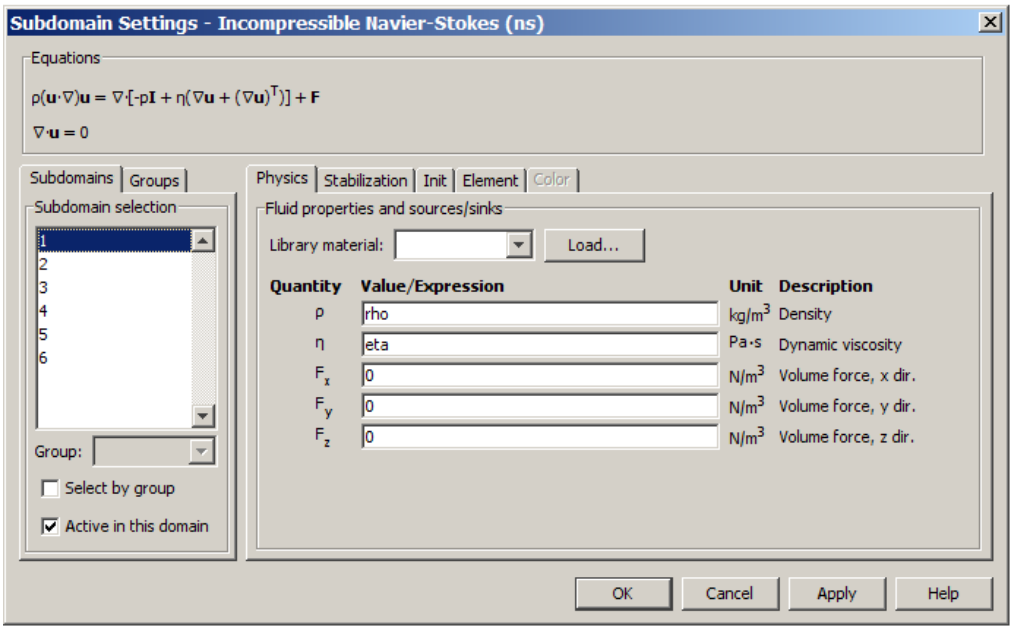

Figure 2.3 The “Subdomain Settings” dialogue box of the “Incompressible Navier Stokes” application mode in COMSOL Multiphysics

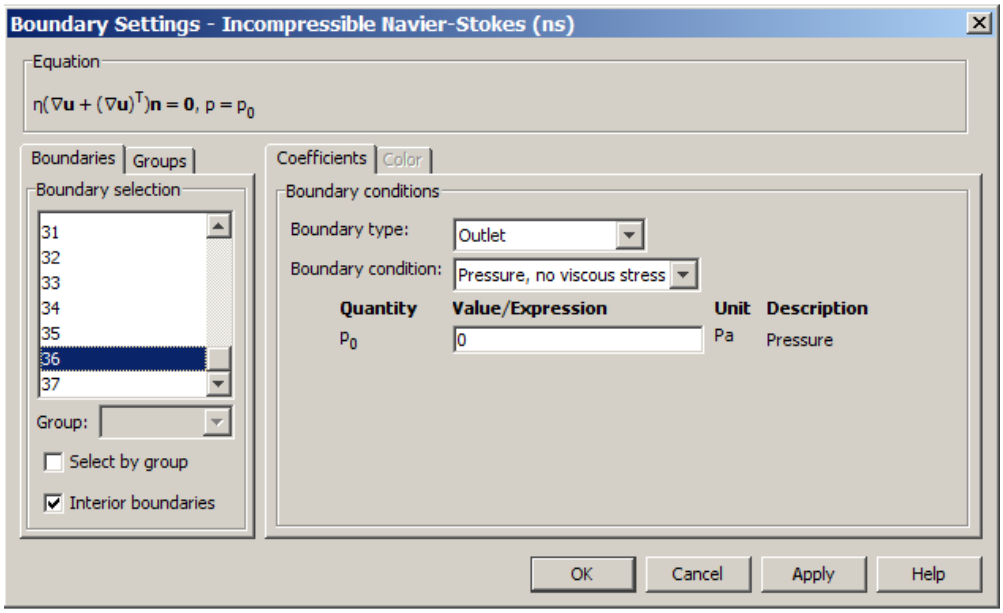

Figure 2.4 This figure shows the boundary settings for the outlet of the channel using the "Boundary Settings" dialogue box of the "Incompressible Navier Stokes" application mode in COMSOL Multiphysics

2.3 Charge Conservation

Since both the fuel and oxidant are dissolved in an acidic electrolyte, the concentration of hydrogen ions was assumed to be uniform throughout the channel. Transport of protons from the anode to the cathode is by electric migration only. In these circumstances the transport of the charged species and the electric field within the electrolyte can be modeled using the potential equation described in the "Conductive Media DC" application mode of COMSOL Multiphysics. The equation describing the electric field within the electrolyte is given as

$$-\nabla.(\sigma_e \nabla \varphi_e) = 0 \tag{2-3}$$

where, φ_e is the local potential in the electrolyte. σ_e represents the ionic conductivity of the electrolyte, and its value for the anolyte is set to 11.47 $S.m^{-1}$ and for the catholyte is set to 43 $S.m^{-1}$. Electric insulation boundary conditions were applied to all of the channel surfaces. Within the electrodes, where charged species are generated or consumed, a current source is applied and the local current density is calculated by the Butler-Volmer reaction kinetics equation described in Section 2.5.

The "Conductive Media DC" application mode was also used to describe the voltage and current distributions within the solid-phase metallic electrodes as

$$-\nabla.(\sigma_s \nabla \varphi_s) = 0 \tag{2-4}$$

Because the metallic electrodes and current collectors are highly conductive, a large value for conductivity (10^7 $S.m^{-1}$) was used for this module. Applying a potential boundary condition for the outer electrode walls resulted in an essentially uniform solid

phase voltage, φ_s, over the entire subdomain. The electric insulation boundary conditions were assigned to other boundaries. Figures 2.5 and 2.6 show the subdomain and boundary settings for the "Conductive Media DC" application mode.

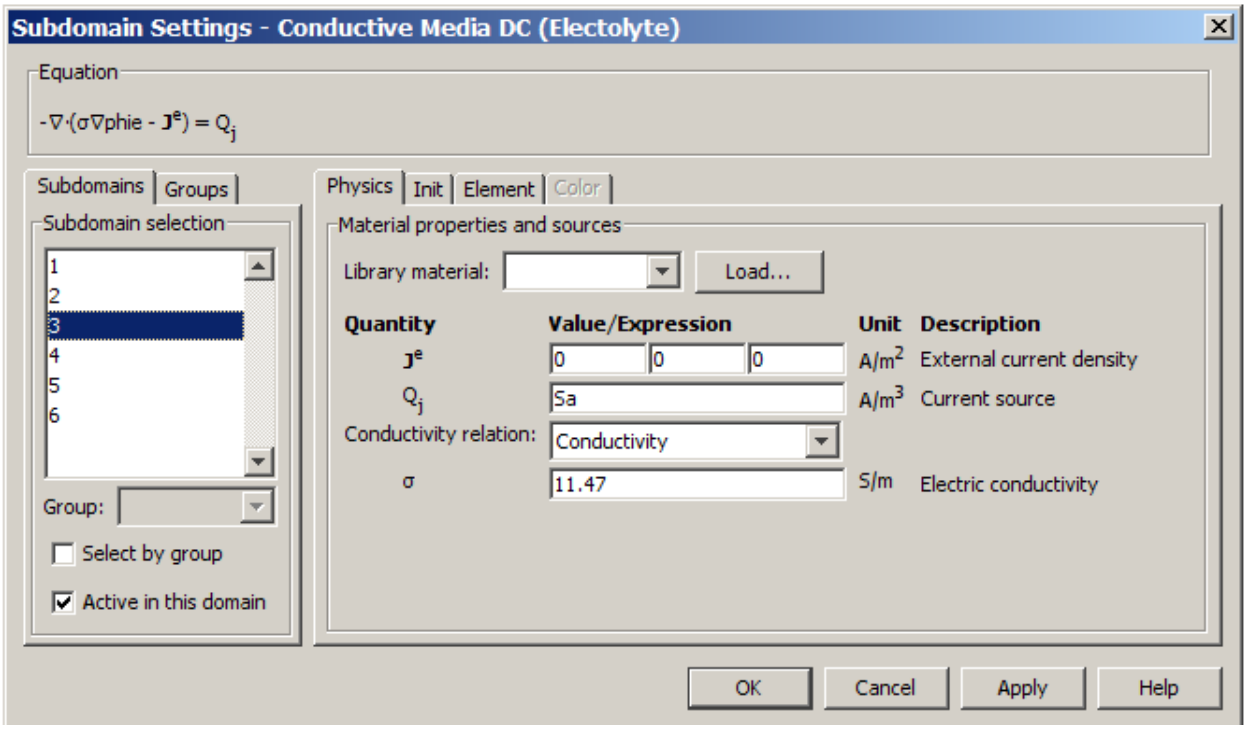

Figure 2.5 This figure shows the settings for the anode subdomain using the "Subdomain Settings" dialogue box of the "Conductive Media DC" application mode in COMSOL Multiphysics

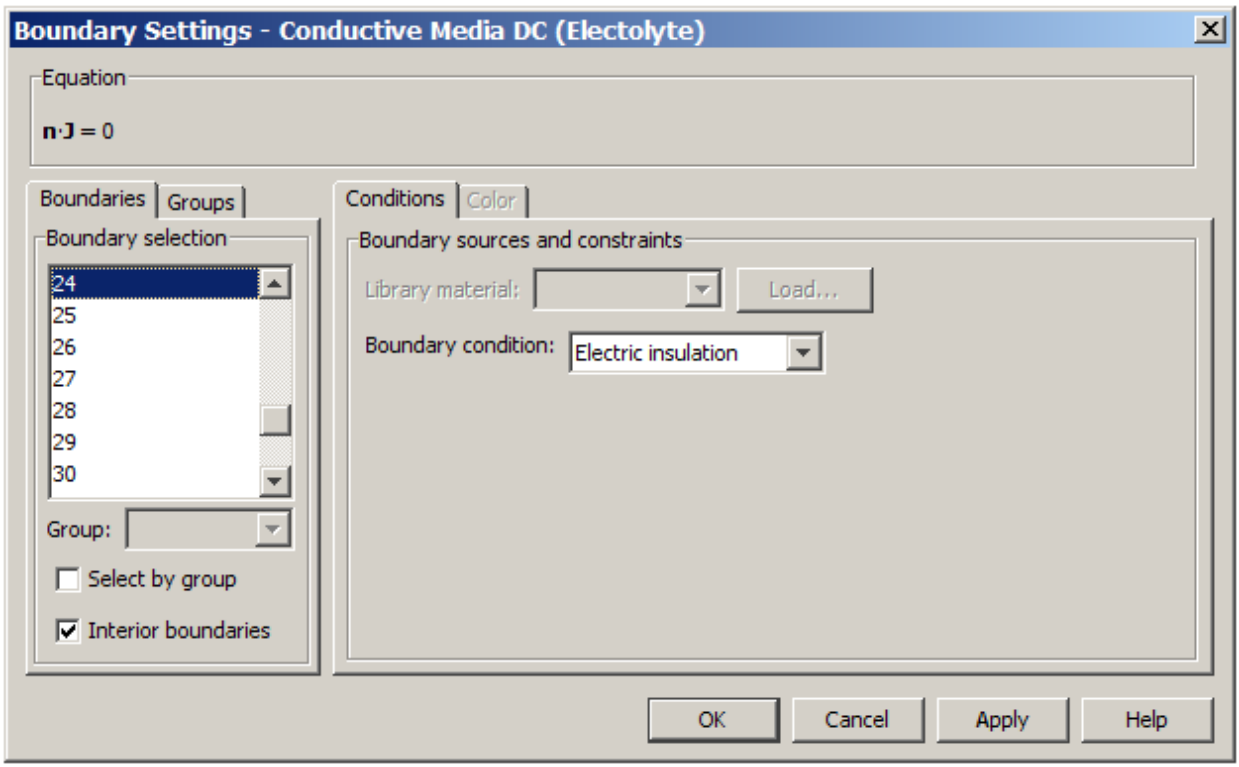

Figure 2.6 The “Boundary Settings” dialogue box of the “Conductive Media DC” application mode in COMSOL Multiphysics.

2.4 Mass Transport

Once the velocity field within the microchannel has been determined by the Navier-Stokes equation, it is possible to use the calculated velocity to model the mass transport phenomena. In the microfluidic fuel cells, the reactant species are transported along the length of the channel by convection. However, diffusive transport in a direction transverse to the flow is necessary to replace reactant species in the vicinity of the electrodes, as they are consumed by reaction. When concentrations are sufficiently low, interactions between different solute species can be ignored and diffusion rates can be assumed to be linearly proportional to concentration gradients [8]. In this model, the system is assumed to be isothermal, and pressure differences are not large enough to influence diffusion coefficients. Considering these assumptions allows the concentration distributions of the fuel and oxidant to be described by the Fick's law [59] given as

$$\nabla.(-D\nabla c + cv) = 0 \tag{2-5}$$

where, c is the local concentration of the reactants. To implement the Fick's law, the "Convection and Diffusion" application mode is used. At the inlets, a uniform concentration is applied. At the outlet, convective flux dominates mass transport and the concentration gradient normal to the outlet is set to zero. Since no transport is possible through the channel walls, insulation boundary conditions were assigned to all of the channel walls. Within the electrode subdomains (where the species are consumed by electrochemical reactions), a source term is added to the above equation. This results in the following equation:

$$\nabla.(-D\nabla c + cv) = \frac{e_i}{nF} i \tag{2-6}$$

where, e represents the mole number, F is the Faraday constant, n denotes the number of electrons transferred in the reaction, and i reflects the rate of the electrochemical reaction which is calculated through Butler-Volmer equation (see

Section 2.5). Figures 2.7 and 2.8 show the subdomain and boundary settings implemented for the ‘‘Convection and Diffusion’’ application mode.

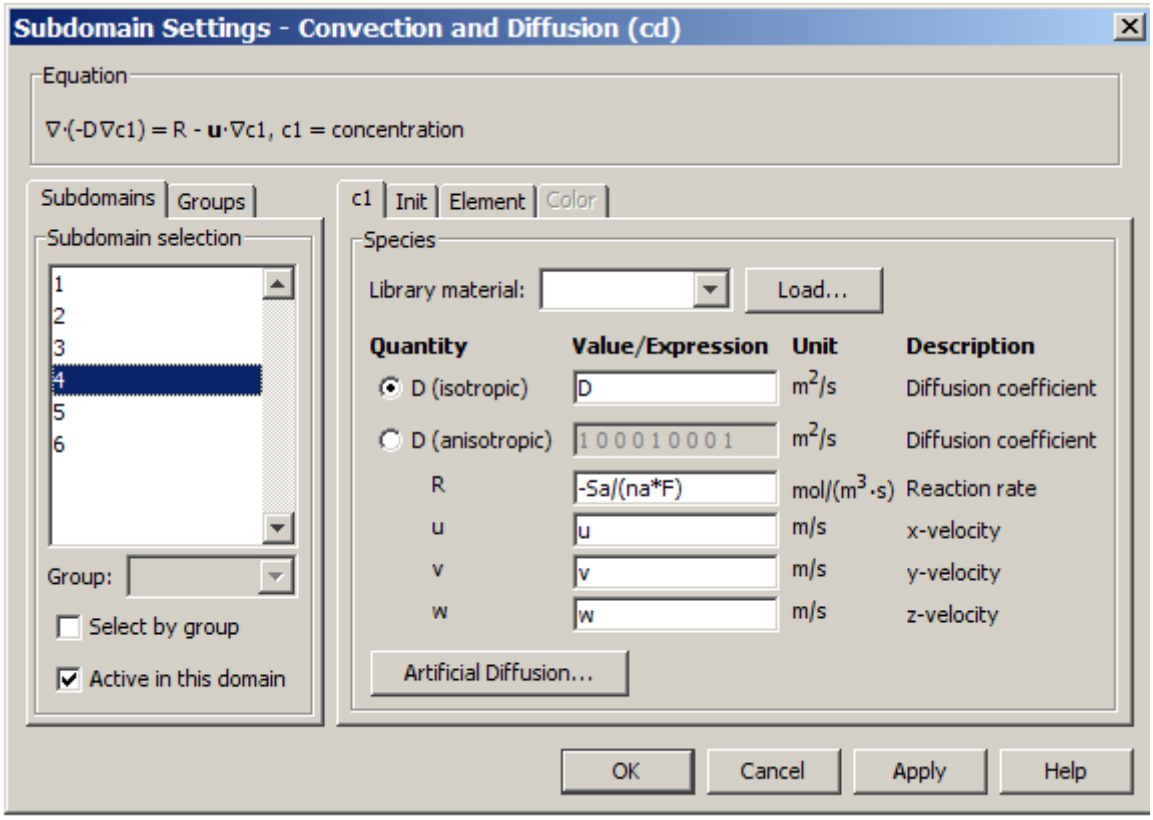

Figure 2.7 This figure shows the settings for the anode subdomain using the “Subdomain Settings” dialogue box of the “Convection and Diffusion” application mode in COMSOL Multiphysics

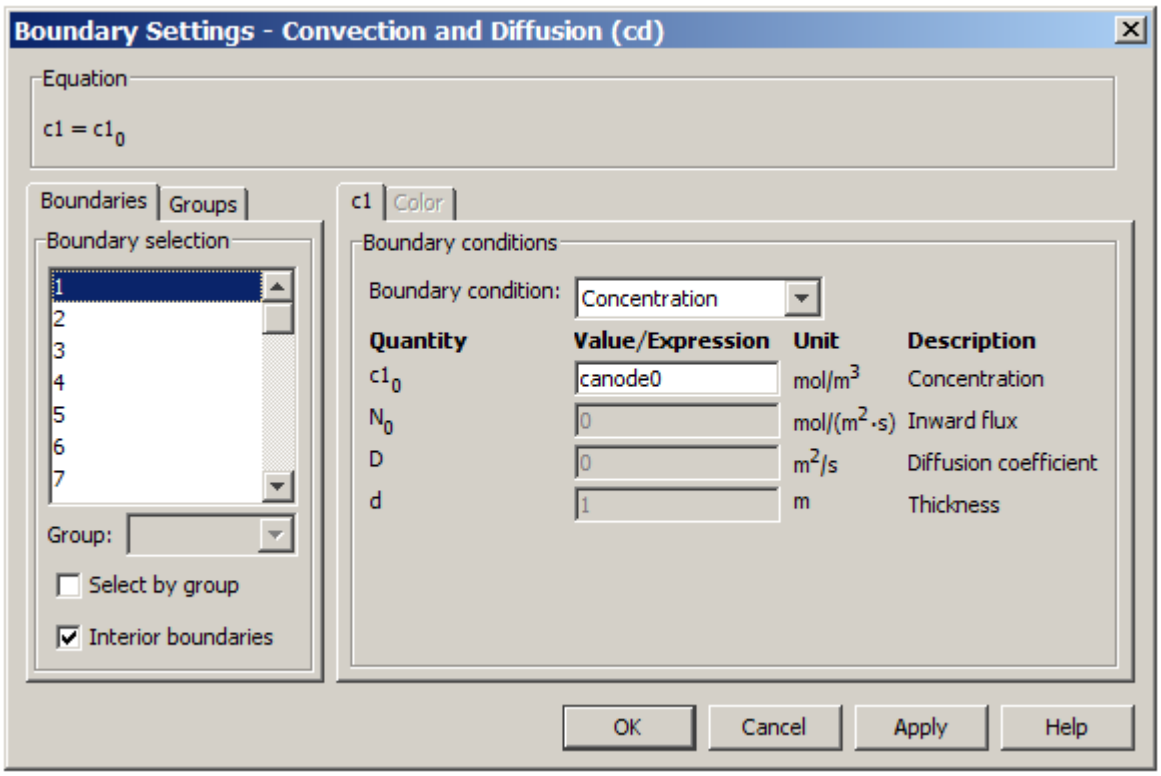

Figure 2.8 This figure shows the boundary settings for the inlet (from which fuel is introduced) using the “Boundary Settings” dialogue box of the “Convection and Diffusion” application mode in COMSOL Multiphysics

2.5 Reaction Kinetics

The Butler-Volmer equation describes the rate of an activation-controlled reaction, for which the rate of reaction is controlled solely by the rate of the electrochemical charge transfer process.

$$i = ai_0 \left[e^{\left(\frac{\alpha nF}{RT}\eta\right)} - e^{\left(-\frac{(1-\alpha)nF}{RT}\eta\right)} \right] \tag{2-7}$$

In the above equation, η is the activation overpotential. There is no concentration term in the original Butler-Volmer equation; however, the Butler-Volmer reaction kinetics equation used here has been multiplied by a concentration term since the rate of the electrochemical reactions in the microfluidic fuel cell is limited by mass transfer. Reaction rates were assumed to be linearly proportional to the reactant concentration. The modified Butler-Volmer equation (Eq. (2-8)) accounts for the effect of the concentrations on the OCP. In essence, this equation describes the local current density, i, across the electrode surface in the microfluidic fuel cell and is related to both the applied electric potential and the concentration of the reactant species [20].

$$i = ai_0 \frac{c}{c_{REF}} \left[e^{\left(\frac{\alpha nF}{RT}\eta\right)} - e^{\left(-\frac{(1-\alpha)nF}{RT}\eta\right)} \right] \tag{2-8}$$

The reactant species are consumed at a rate of S, which is proportional to the current density [20].

$$S = \frac{e_i i}{nF} \tag{2-9}$$

At each electrode, it is necessary to calculate the activation overpotential, which is required to overcome irreversibilities, as the reaction deviates from its equilibrium state. This overpotential is expressed by the potential difference between the solid phase and the electrolyte phase, and it is defined as [60]:

$$\eta = \phi_s - \phi_e \qquad \text{Anode side} \tag{2-10}$$

$$\eta = \phi_s - \phi_e - \text{OCP} \qquad \text{Cathode side} \tag{2-11}$$

The potentials of the solid electrode, ϕ_s, and the adjacent electrolyte, ϕ_e, are found by the solution of the potential equations (Eqs. (2-3) and (2-4)). The open circuit potential, OCP, was taken as a constant value and is assumed to be approximately equal to 0.9 V to match the experimental data given by Choban et al. [17]. Although the OCP varies with the local concentrations of the reactants and products in the electrolyte, the concentration term factored into the equation adequately accounts for the dependency of the reaction rate on the reactant concentration [61]. Using these three quantities, the activation overpotential can be calculated. Figure 2.9 shows how to introduce the Butler-Volmer equation in COMSOL. The ‘‘Scalar Expressions’’ dialogue box can be found at the ‘‘Options’’ menu under the ‘‘Expressions’’ submenu.

For each point on the polarization curve, the cell voltage is taken as the solid phase potential assigned to the cathode since the anode is arbitrarily chosen as the ground. The current density is obtained in the post processing by integrating the normal current density on the cathode boundaries and normalizing it by the channel volume to find the geometry that produces the highest power density per volume. This demonstrates which design is the most suitable as a compact power source for portable devices [36]. To be consistent with the results reported in the literature [17, 20, 33], the output current has also been normalized by the electrode surface area. The polarization curves obtained for different geometries are presented in Chapter 3.

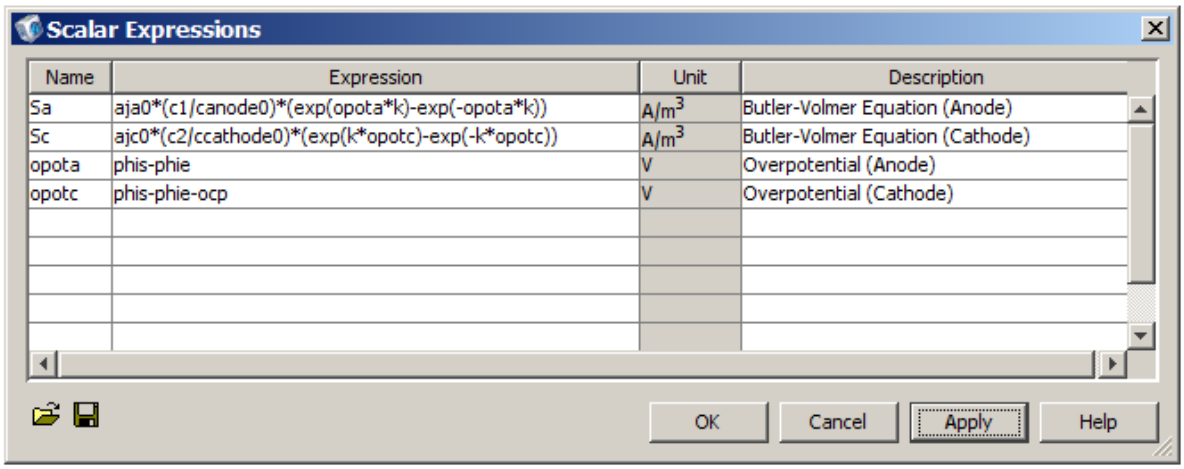

Figure 2.9 The "Scalar Expression" dialogue box where the Butler-Volmer equations are defined

2.6 Implementation in COMSOL

2.6.1 Solution Procedures

A parametric sweep is used to calculate the current density at different cell voltages. Since the Butler-Volmer reaction kinetics expression (Eq. (2-8)) creates bidirectional coupling between the potential and convection-diffusion equations, the two must be solved simultaneously in order to obtain an accurate solution. However, the coupling of these equations results in a set of non-linear equations for which it is difficult to obtain convergence from the COMSOL's non-linear solver. Therefore, instead of solving the modules in a coupled manner, it is recommended to solve this system of equations in an iterative manner. Below, two different implementations of the iterative solution procedure in COMSOL are elaborated in detail.

Stationary Segregated

An iterative solution procedure was implemented by using the stationary segregated solver. This method allows for a stable solution procedure with reduced memory requirements while still accounting for the coupling between the physics modules. To keep the solution time reasonable and ensure a robust solution procedure, the direct UMFPACK linear system solver was used for all modules. In this work, the direct solvers are preferred over indirect solvers since they are often faster and require less tuning. The advantage of the ‘‘stationary segregated’’ method is that the user can determine a preferred termination criterion in terms of the value of the relative error used to terminate the iterations. Figure 2.10 shows the dialogue box featuring the implementation of this method in COMSOL.

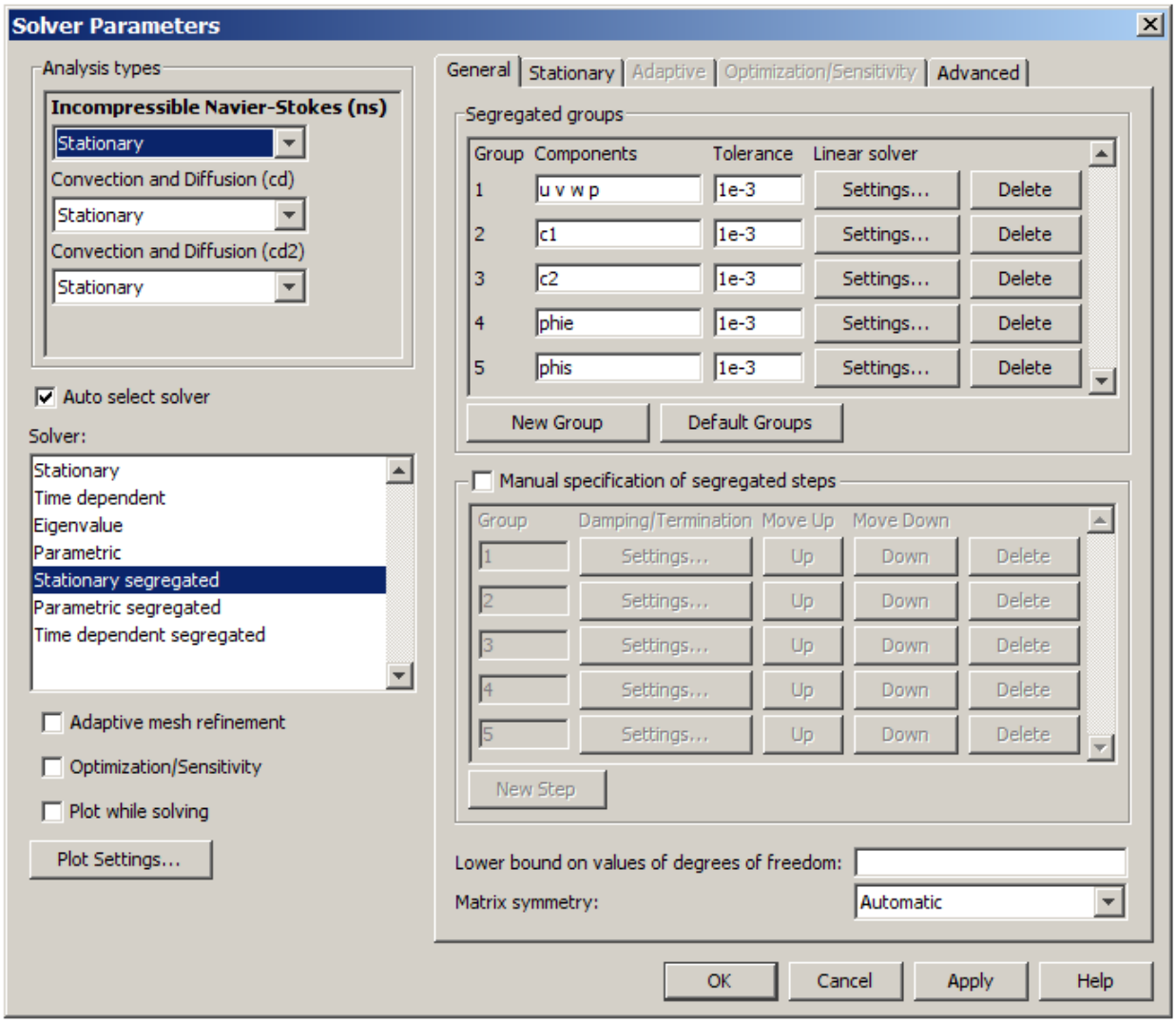

Figure 2.10 The "Solver Parameters" dialogue box showing how to implement "Stationary segregated" solution procedure.

Sequenced Solver

This iterative procedure can also be implemented by using a solver sequence. The fluid flow equations (Eqs. (2-1) and (2-2)) can be solved first since the solution to these equations is not influenced by the other application modes in the model. The solution is then stored to describe the velocity field for the convection-diffusion equation. The coupling of the potential and convection-diffusion equations results again in a set of non-linear equations which requires an accurate initial estimate of the solution in order to obtain convergence from COMSOL's non-linear solver. To obtain this estimate, the

equations are solved independently in an iterative manner. The electric field was first determined by solving the potential equations (Eqs. (2-3) and (2-4)) with the default linearization point. Using the calculated electric field and the stored solution for the velocity field, the convection-diffusion equation is solved to obtain an initial estimate for the concentration distribution. The calculated concentration distribution is used to solve the potential equation again to obtain a second estimate for the electric field which is then used to solve the second iteration of the convection-diffusion equation. After several iterations, the two equations were solved simultaneously. Tests were performed to ensure that the calculated polarization curve was independent of the number of iterations. Again, to keep the solution time reasonable and ensure a robust solution procedure, the direct UMFPACK linear system solver was used for all modules. Figure 2.11 demonstrates this procedure.

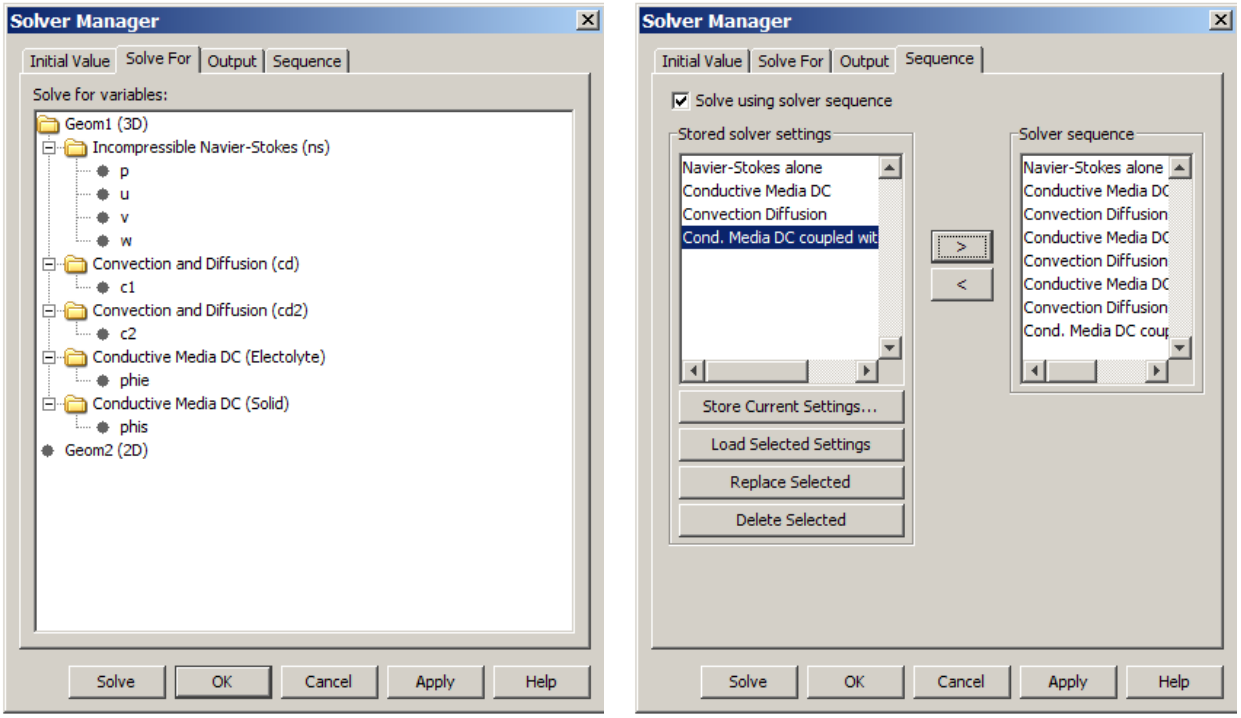

Figure 2.11 The “Solver Manager” dialogue box used to solve the PDEs separately is shown. Using the “Sequence” tab, it is possible to put the solvers in a desired order before solving them.

Both above methods have been tested for a few points of the polarization curve. They both gave almost the same results. In this thesis, however, the first method (i.e., stationary segregated) was used to determine the relative error as a termination criterion.

2.6.2 Meshing

By solving the model repetitively with progressively smaller mesh sizes, it was found that a very fine mesh pattern was required around the electrodes to obtain convergence and ensure that the solution is accurate and independent of the mesh size. This refinement was made for two reasons: 1) to allow for computing the accurate flux when calculating the current density, and 2) to ensure the numerical stability of the convection-diffusion equation which can become unstable in the presence of steep concentration gradients. For the model developed in this thesis, tetrahedral meshes are used. The predefined ‘‘Coarser’’ mesh size, which automatically determines the mesh parameters, is used to establish the mesh in the electrode subdomains. In the subdomains outside of the electrodes, the maximum element size is manually set to 0.17 mm and the element growth rate is set to 1.4. Depending on the geometry, the total number of mesh elements varies from about 30000 to 40000.

The model was solved on a 64-bit Windows Vista platform, with an Intel Xeon 2.26 GHz quad-core processor. Peak memory usage was observed to be about 5 GB.

Similar modeling procedure with minor changes has been practiced for all of the various geometries presented in this thesis.

2.7 Assumptions and Limitations of the Developed Numerical Model

There are a few assumptions associated with the numerical model developed in this thesis which are made to make the model simpler and more time efficient. For example, the electrolyte solution is assumed to be incompressible and isothermal. These assumptions normally do not cause any significant disparities between the numerical and experimental results; however, certain assumptions do limit the range of operating parameters in which the numerical model accurately predicts the performance. For instance, it is assumed that the viscosity, density and the electric conductivity are constant and equal for anodic and cathodic streams. The numerical model with these assumptions reflects the reality in low electrolyte velocities. When the velocity is high, small differences in the density and viscosity of the two streams lead to hydrodynamic instabilities which cannot be captured by the numerical model. It is also assumed that the electric conductivity of the electrolyte streams is constant and independent of the reactant concentrations. With this assumption, the numerical model accurately describes the experimental conditions for low current densities. At high current densities, the electrochemical reactions become faster and as a result the reactant species can be sufficiently depleted to change the local electric conductivity of the electrolyte. Thus, the total ionic resistance of the fuel cell can increase leading to greater ohmic losses which are not accounted for in the numerical model.

The model developed in this thesis describes the steady-state operation. Therefore, the model cannot capture the transient behavior when the fuel cell is turned on or off. Depending on the operating conditions, the transient state would take up to several minutes during which the numerical model is not capable of predicting the fuel cell performance.

3. Results for Microfluidic Fuel Cells with Solid Electrodes

The development of an accurate model capturing the phenomena occurring in the microfluidic fuel cells is not a trivial task. This research presents the 3-D numerical simulation developed using the COMSOL Multiphysics toolbox (explained in Chapter 2) to determine the performance of different microfluidic fuel cell designs. The developed model describes the effects of the activation, ohmic and mass transport overpotentials. The model is first verified against the numerical and experimental results reported in the literature [17, 20]. Once the validity of the model is confirmed, it is used to study the effect of different changes in the microfluidic fuel cell geometry including different channel lengths and channel aspect ratios, 3rd flow insertion and placing multiple inlets. At the end, an innovative design is proposed to control the growth rate of the mixing region. This design which takes advantage of a tapered channel is tested by the developed numerical model. It is shown that the aforementioned design enhances the performance of the cell compared to a non-tapered channel.

3.1 Model Validation

The model is first tested for evaluating the performance of a 30 mm-long channel. The formulations used to develop the model are similar to those reported by Chang et al. [20]. Table 3.1 presents the values of the parameters set in the model. The results of the developed model compared to those reported by Chang et al. [20] are shown in Figure 3.1. It is clear that the results are in very good agreement.

Table 3.1 The Constants Used in the Anodic and Cathodic Flows for Solid Electrode Design

Parameter	Anode	Cathode
Flow rate	250 μl.min^{-1}	250 μl.min^{-1}
Density, ρ^*	1000 kg.m^{-3}	
Dynamic viscosity, μ^*	0.001 Pa.s	
Faraday constant, F	96485.34 C.mol^{-1}	
Cell temperature, T	298 K	
Universal gas constant, R	8.314 J.mol^{-1}K^{-1}	
Ionic conductivity, $\sigma_e{}^*$	11.47 S.m^{-1}	43 S.m^{-1}
Diffusion coefficient, D^{**}	8.3 × 10^{-10} m^{2}s^{-1}	8.3× 10^{-10} m^{2}s^{-1}
Charge transfer coefficient, α^*	0.5	0.5
Number of electrons transferred, n^*	2	4
Exchange current density, $ai_0{}^*$	3.82× 10^5 A.m^{-3}	100 A.m^{-3}
Inlet concentration, $c_0{}^*$	2100 mol.m^{-3}	0.5 mol.m^{-3}

* The value is obtained from [20].

** An approximated value for the diffusion of relatively small molecules in an aqueous solution is assumed [8].

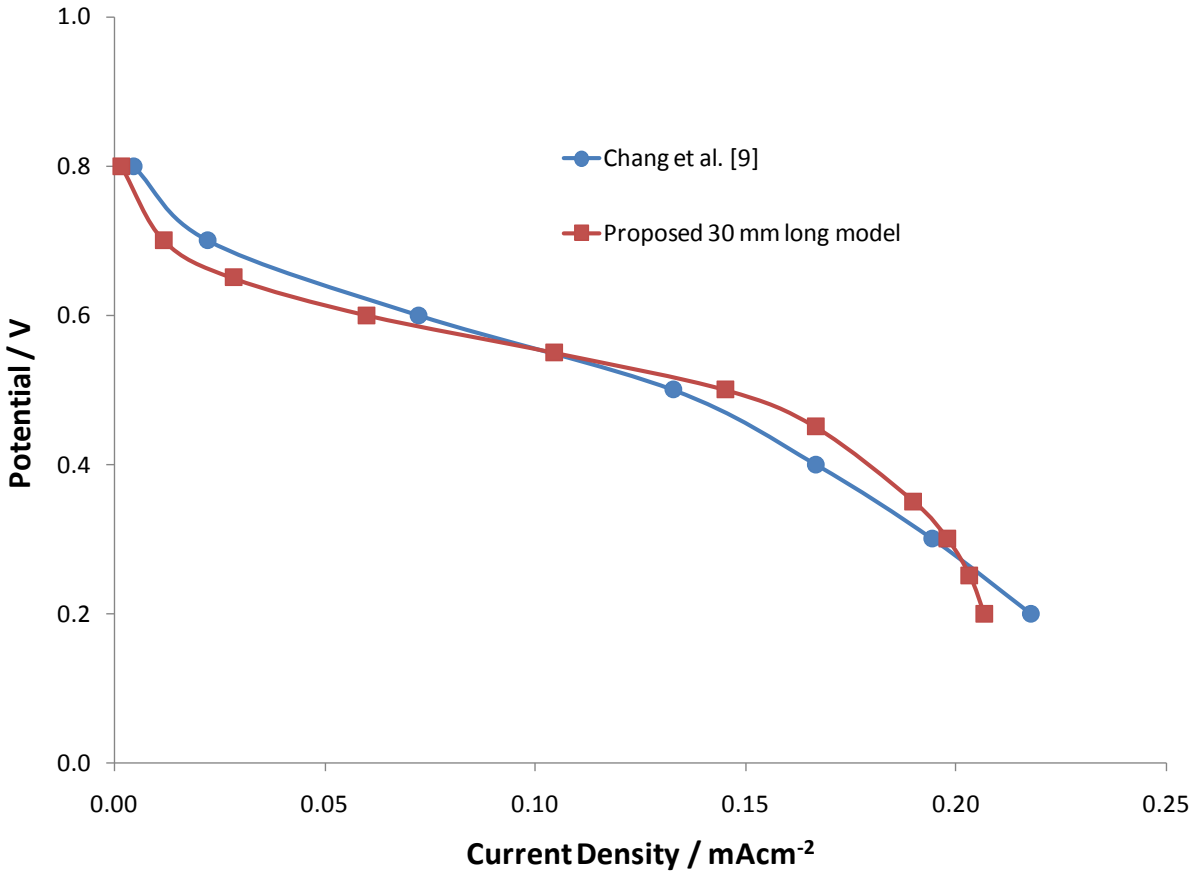

Figure 3.1 Verification of the proposed model against the results reported by Chang et al. [20] for a 30 mm-long channel

To verify further the numerical model accuracy, the results were compared to the experimental values reported by Choban et al. [17]. It is found that there is some discrepancy between the numerical results of Chang et al. [20], to which the model presented in this thesis was compared first, and the experimental work of Choban et al. [17] even though both studies used the same cell geometry and concentrations of fuel and oxidant species. The discrepancy is quantitative but the pattern of the polarization curves is similar. To find a better agreement between the numerical values and the experimental data, it is necessary to make some adjustments to the model parameters.

In this thesis, this issue is in part resolved by increasing the diffusion coefficient of the fuel and oxidant from 8.3×10^{-10} m^2s^{-1} to 2.456×10^{-9} m^2s^{-1} (this value was used by Chen et al. [54]). As another adjustment, the cathode exchange current density (a parameter related to the electrochemical activity of the oxidant species on the cathode catalyst) is doubled from 100 $A.m^{-3}$ to 200 $A.m^{-3}$. It is reasonable to use the exchange current density as a fitting parameter since the true value is not known and depends on several factors including CO poisoning of the catalyst [62], orientation of the platinum crystals [62], and surface roughness of the electrodes [20]. Figure 3.2 is obtained after making the aforementioned adjustments to the model parameters, and it shows good agreement between the calculated polarization curve and the experimental results obtained from [17]. Since the equations implemented in this model (presented in this thesis) accurately describe the physics governing microfluidic fuel cell operation, the developed model can be used to fit any experimental results. Fitting the model results to match experimental data is only a matter of adjusting some of the constant parameters, such as the diffusion coefficient (as it depends on the type of the fuel/oxidant used) and the exchange current density (as it, in fact, changes from one experiment to another even if they are using the same reacting species since the orientation of the platinum crystals and surface roughness of the electrodes can be different from one experiment to another one).

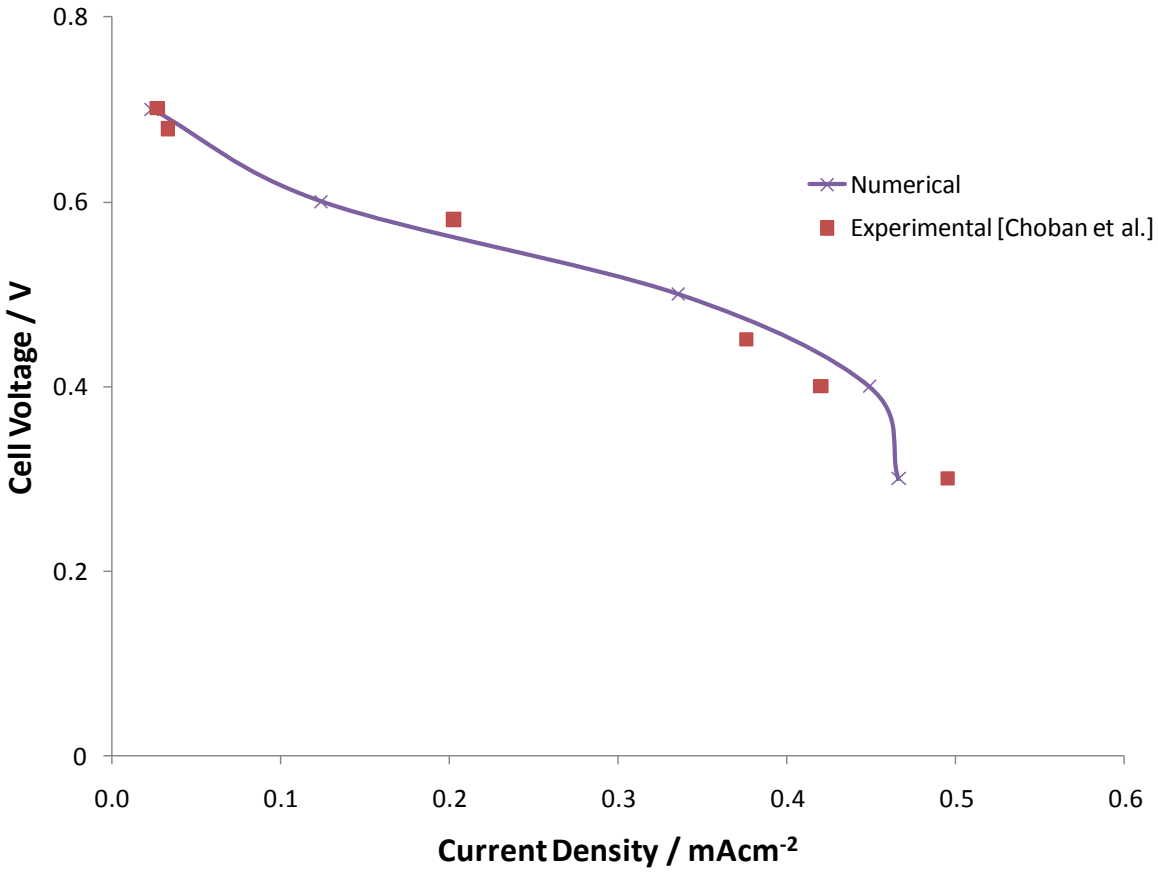

Figure 3.2 The verification of the proposed model against the experimental results reported by Choban et al. [17]

3.2 Results of Developed Model for Different Designs

Cell polarization curves are used as a quantitative measure for cell performance. In previous studies [19, 20, 29, 30, 33], the current and power were conventionally normalized by the electrode surface area. However, it is reasonable to normalize the current and power by the overall fuel cell volume, which is a clear indication of the fuel cell's effectiveness as a compact power source [36]. For most of the polarization curves obtained here, normalizing based on the volume or area does not change the final results. For these cases, the polarization curves obtained based on normalizing the current by the volume are only presented. In the case(s) in which the outcome depends on which normalization is used, both types of polarization curves (per unit volume and area) are presented.

3.2.1 Study the Effect of the Length of the Channel

The model explained in Chapter 2 was first used to study the effect of the length of the channel on the cell performance. The results of this study are presented in Figure 3.3. It is clear that by reducing the channel length higher power densities can be achieved. This is due to the fact that the concentration boundary layer is thinner at the beginning of the channel. The thinner the boundary layer, the higher the concentration gradient. Higher concentration gradient leads to higher reaction rates which finally results in higher current generation. As the fluid travels down the channel, the boundary layer becomes thicker, and hence the concentration gradient becomes smaller which slows down the reaction rate. As a result, the electrode surface area at the vicinity of

the inlets is more crucial in terms of power generation. That is why a shorter channel contributes to higher power density.

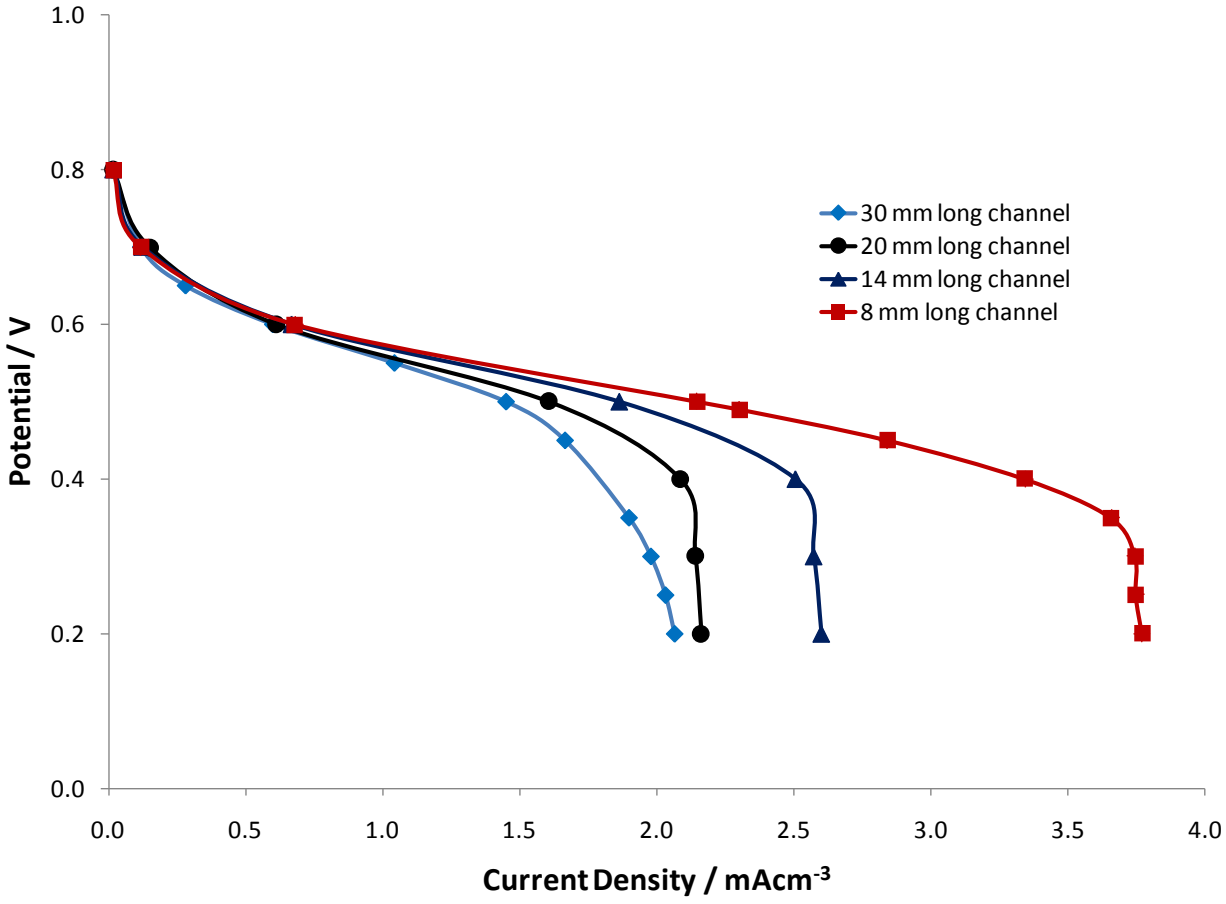

Figure 3.3 The effect of the channel length on the microfluidic fuel cell performance

There is one problem associated with the short-length channels and that is low fuel utilization, which is defined as the ratio of the amount of the consumed species at the electrodes to the total amount of the fuel delivered to the cell (Eq. (3-1)).

$$Fuel\ Utilization = \frac{\langle c\vec{u}\rangle_{inlet} - \langle c\vec{u}\rangle_{outlet}}{\langle c\vec{u}\rangle_{inlet}} \tag{3-1}$$

In this equation, $\langle c\vec{u}\rangle$ represents the concentration flux. The problem associated with low fuel utilization can be resolved by appropriate choice of redox species. For

example, using formic acid in sulfuric acid as the fuel and hydrogen peroxide in sulfuric acid as the oxidant will allow simple fuel recycling and thus better fuel utilization [30].

3.2.2 Study the Effect of the Different Cross-Section Aspect Ratios

The cross-section of the microfluidic fuel cell channel has been designed in different shapes. Figure 3.4 depicts the different channel cross-section aspect ratios and electrode configurations studied in this thesis. The numerical model is used to study the effect of the aspect ratio of the configuration on the cell performance.

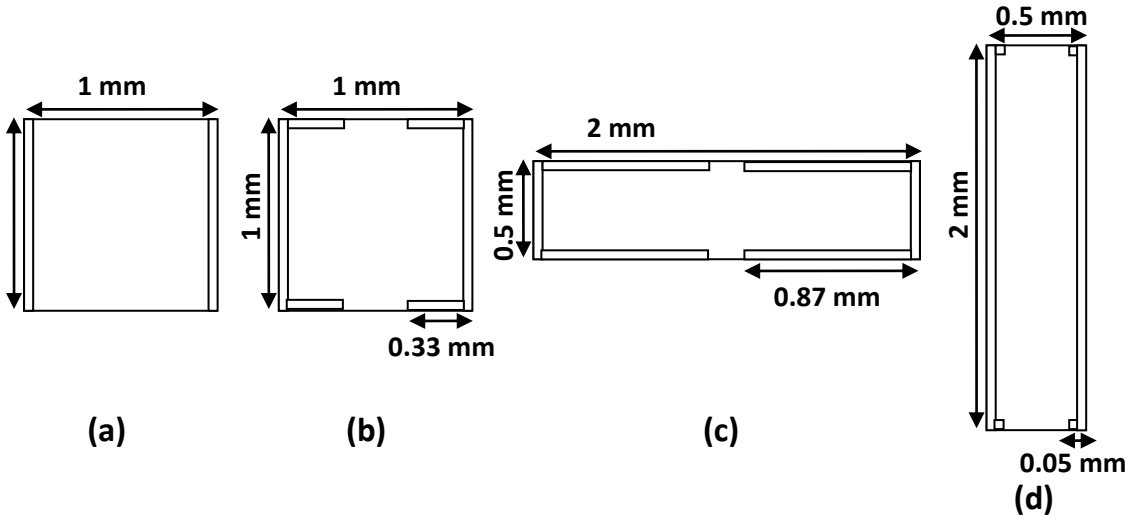

Figure 3.4 The schematics and dimensions of different cross-section aspect ratios and electrode geometries are presented in (a), (b), (c), and (d) which are referred to the "Simple square", "Extended square", "Low aspect ratio" and "High aspect ratio", respectively. The electrodes in (b), (c) and (d) are extended away from the side walls toward the centre of the channel up to the edges of the mixing region.

Figure 3.5 compares the polarization curves obtained for microfluidic fuel cells with different cross-section aspect ratios (i.e., height to width ratio). The results

presented in Figure 3.5 were obtained based on normalization of the current by the surface area. One of the important points in Figure 3.5 is related to the ‘‘Extended square’’ configuration which is basically the square cross-section with the electrodes extended away from the side walls toward the centre of the channel up to the edges of the mixing region (see Fig. 3.4 (b)). When the results are presented based on normalizing the current by the surface area, the performance of the cell with the ‘‘Simple square’’ cross-section seems to be better than that of the ‘‘Extended square’’ cross-section. It may seem that the added surface area by the extension of the electrodes toward the center of the channel does not contribute to current generation as much as the side wall electrodes do. However, this comparison still leaves some uncertainty as to which is a better design because the larger electrode area of the ‘‘Extended square’’ design may compensate for the lower per area output. Normalizing by the volume removes this uncertainty and shows conclusively that the greater active area of the ‘‘Extended square’’ geometry does in fact compensate for the lower per area performance, and is actually a better design from the point of view of developing a compact power source (see Figure 3.6). The fuel utilization of these geometries is also obtained. It is found that the fuel utilization for the ‘‘Simple square’’ and the ‘‘Extended square" geometries at 0.45V is 13.8% and 15.4%, respectively.

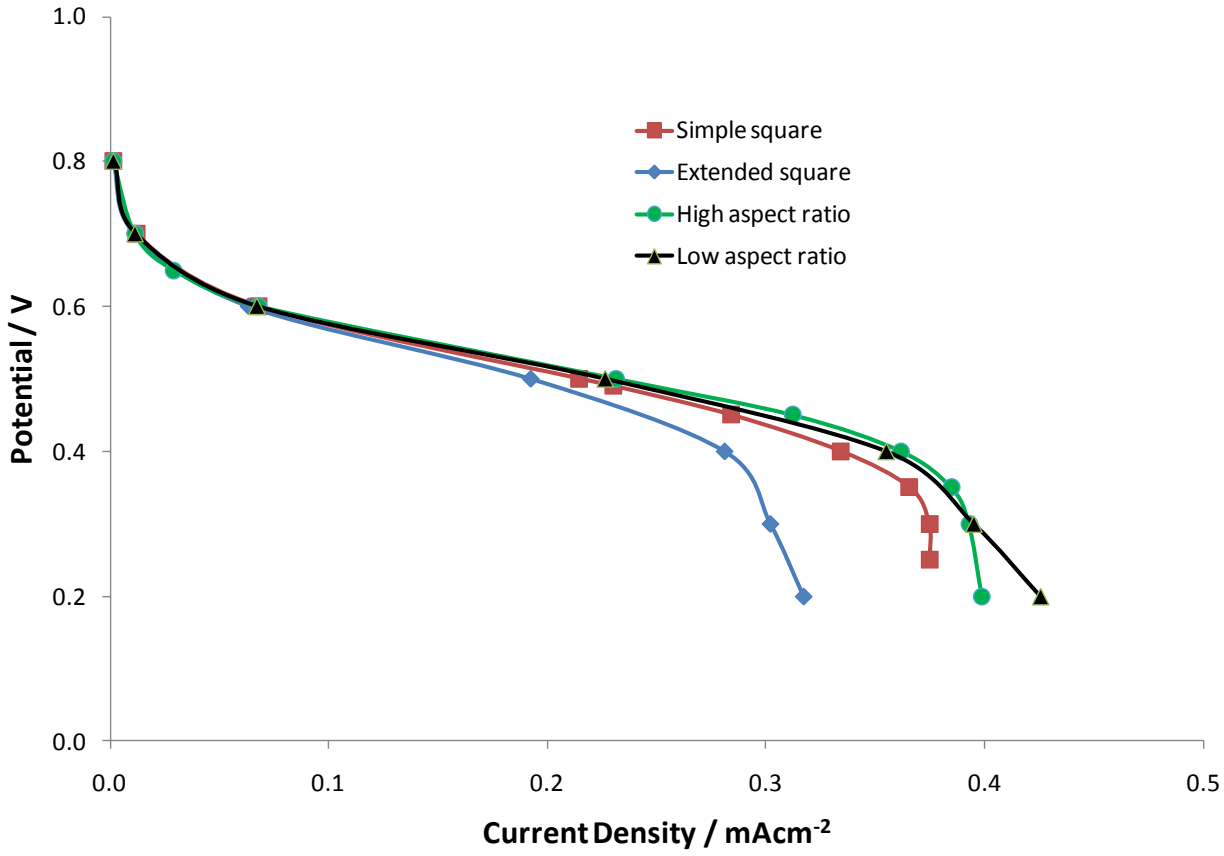

Figure 3.5 The effect of the channel aspect ratio and electrode geometry is shown. The current is normalized by the surface area.

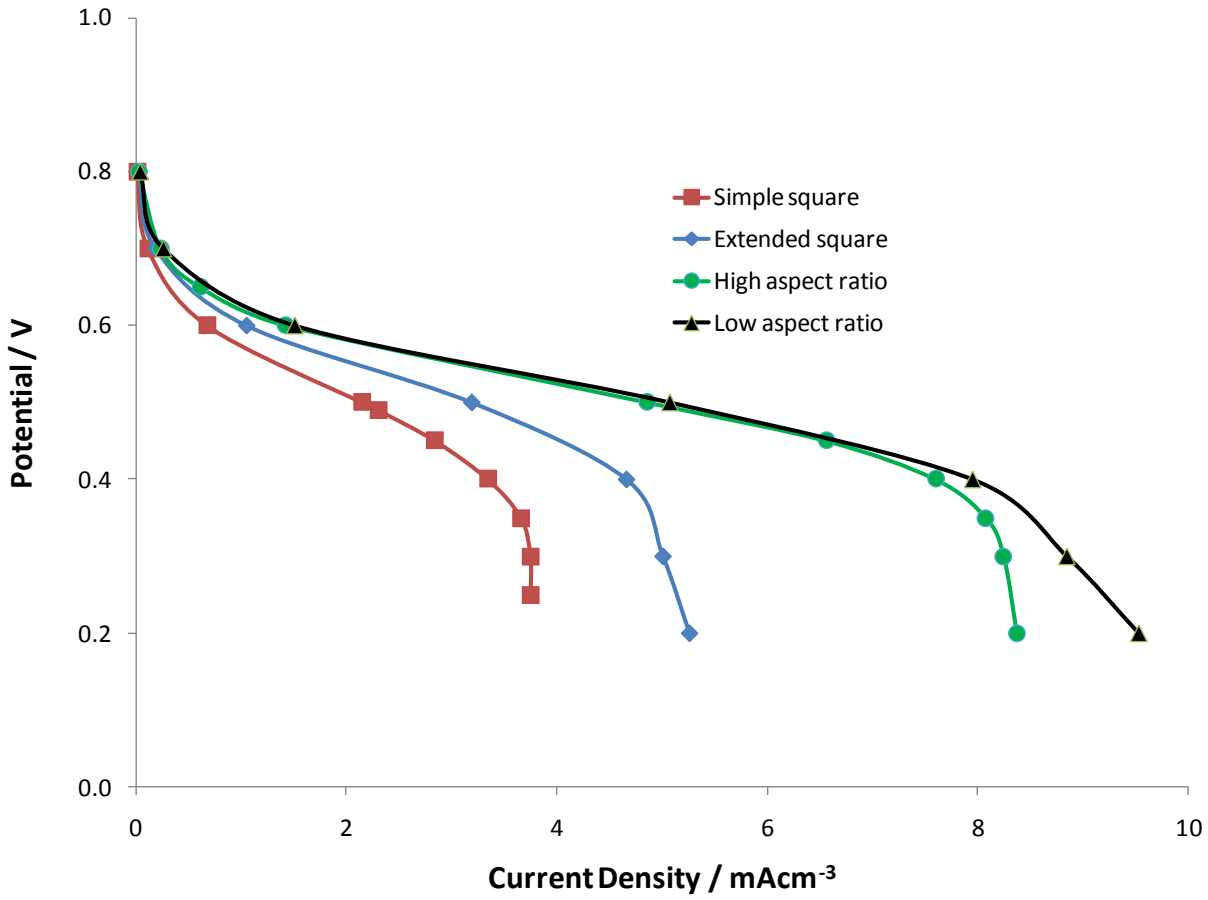

Figure 3.6 The effect of the channel aspect ratio and electrode geometry is shown for the case that the current is normalized by the cell volume.

The high and low aspect ratio geometries have higher power density than the square channels for both area- and volume-based normalization (see Figures 3.5 and 3.6). This is due to the high electrode surface area incorporated in these designs (see Figures 3.4 (c) and (d)). The active surface area in the “Low aspect ratio” geometry is 4.48mm × 8mm which is slightly more than what is incorporated in the “High aspect ratio” geometry (i.e., 4.2mm × 8mm). In spite of the above fact, both geometries have approximately the same power output up to a certain point in the polarization curve. This is because of the high Peclet number and low average ionic resistance of the electrolyte in the “High aspect ratio” geometry compared to those in the “Low aspect ratio” geometry. These two factors compensate for the slightly smaller active surface area in the “High aspect ratio” geometry, and hence cause the “High aspect ratio”

design to generate almost the same power output as the “Low aspect ratio” structure for low to medium range of current densities. At very high current densities, the main limiting factor is the mass transport issue which is caused by the loss of reactants at the vicinity of the electrodes (and the low rate of species diffusion). The concentration of the oxidant around the cathode for low and high aspect ratio geometries is shown in Figure 3.7. This mass transport issue dominates over the ohmic losses making the available electrode surface area a more important parameter in current generation compared to the overall ionic conductance between the anode and cathode. Therefore, from a certain point onward, the lower ionic resistance of the “High aspect ratio” design cannot compensate for its lower electrode surface area as the active surface area is more important factor compared to the ionic conductance in high current densities. In other words, it is easier for the reacting species to reach to the active sites when the electrode surface area is larger. In the “Low aspect ratio” channel, on the other hand, the larger active surface area alleviates the mass transport issue to a certain extent and prevents the sharp drop of the polarization curve similar to what is observed for the “High aspect ratio” geometry at high current density region.

The relative importance of the active surface area at high current densities as opposed to low current densities can also be understood by examining the relationship between mass transport and current generation and studying the concentration gradient around the electrodes for different points on the polarization curve (one at low and the other at high cell voltage). Since it is a diffusive process, the mass transport from the bulk flow to the electrodes is directly dependent on concentration gradients. Neglecting the two small boundaries at the start and end of the electrode subdomains, the total concentration flux of the reactant entering either the anode or cathode can be calculated by integrating the concentration gradient over the electrode boundaries as

$$Electrode\ Concentration\ Flux = \int_s D\nabla c \cdot d\vec{A} \tag{3-2}$$

where $d\vec{A}$ is the differential area vector normal to the electrode surface. Since there can be no accumulation or depletion of reactant species in a steady state operation, the consumption rate of reactant species by electrochemical reactions and the diffusive flux of reactants entering the electrode subdomains must be equal (again neglecting the small electrode boundary at the outlet where some reactant is removed from the cell by convection). Therefore, the total current generated by the fuel cell, I, which is proportional to the reactant consumption rate, must also be proportional to the concentration flux of the reactant species entering the electrode subdomain and can be calculated as below:

$$I = \frac{nF}{e_i} \int_s D\nabla c \cdot d\vec{A} \tag{3-3}$$

The above equation indicates that the fuel cell current is essentially proportional to the product of the concentration gradient and the electrode area. Figure 3.8 shows that for the same operating voltage, both the low and high aspect ratio channels have similar concentration gradients. Also, the concentration gradients for low cell voltages (corresponding to higher average current density) are greater in both cases. Since the concentration gradients for both cells are similar when operating at the same voltage, the difference in the total current output is proportional to the difference in the active area. Although the relative difference in the current output of the two cells will remain approximately the same for different operating voltages, the absolute difference will increase at lower cell voltages due to the multiplication of the difference in the active area with greater concentration gradients. This effect is manifested in the polarization curve by the growing gap between the current density of the two cells as the operating voltage decreases (or current density increases).

The fuel utilization of the low and high aspect ratio channels is also obtained. It is found that the fuel utilization for both designs is approximately 18% when the cell voltage is at 0.45V.

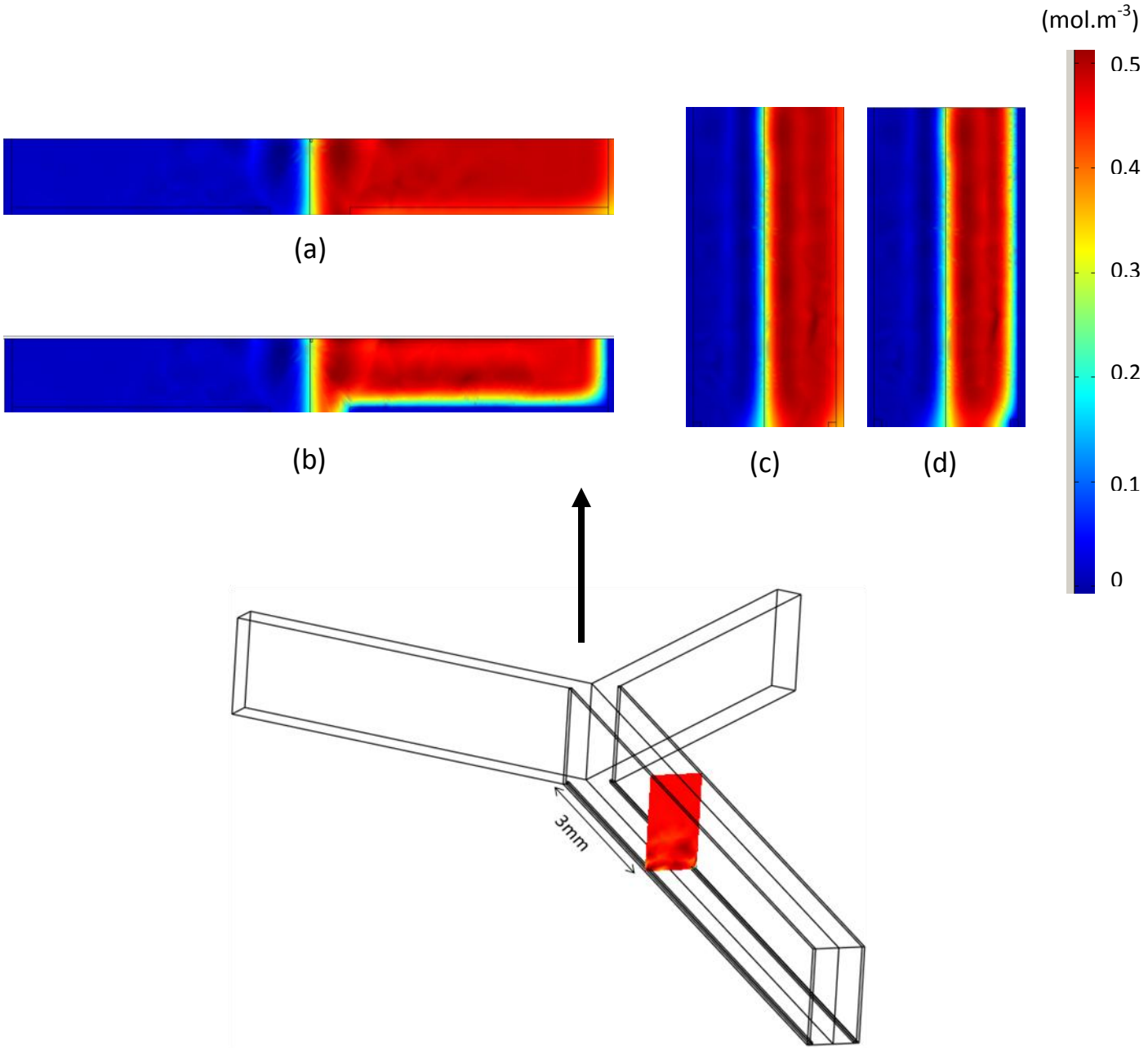

Figure 3.7 The oxidant concentration contour plot at two different cell voltages (600mV and 320mV) emphasizing on the loss of oxidant at the vicinity of the electrodes (depletion regions) particularly in (b) “Low aspect ratio” operating at 320mV and (d) “High aspect ratio” operating at 320mV. (a) and (c) show the oxidant concentration at 600mV.

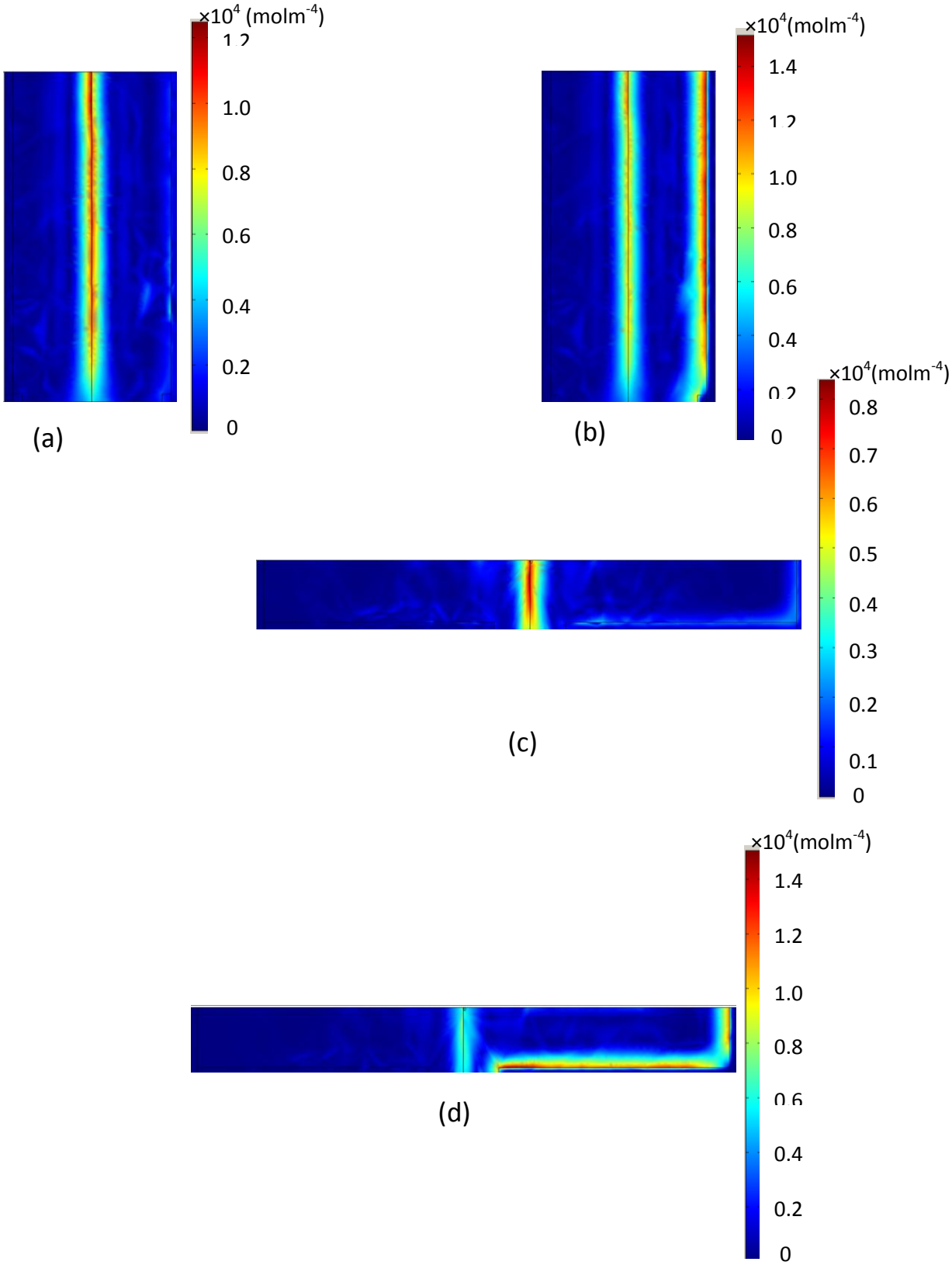

Figure 3.8 Contour plots (plane at 3mm) showing the concentration gradient of the oxidant in (a) "High aspect ratio" operating at 600mV, (b) "High aspect ratio" operating at 320mV, (c) "Low aspect ratio" operating at 600mV and (d) "Low aspect ratio" operating at 320mV

3.2.3 Study the Effect of Inserting the 3rd Flow

The model presented in this thesis is also used to study the performance of the multi-stream laminar flow configuration proposed by [33]. The schematic of such a design is presented in Figure 3.9.

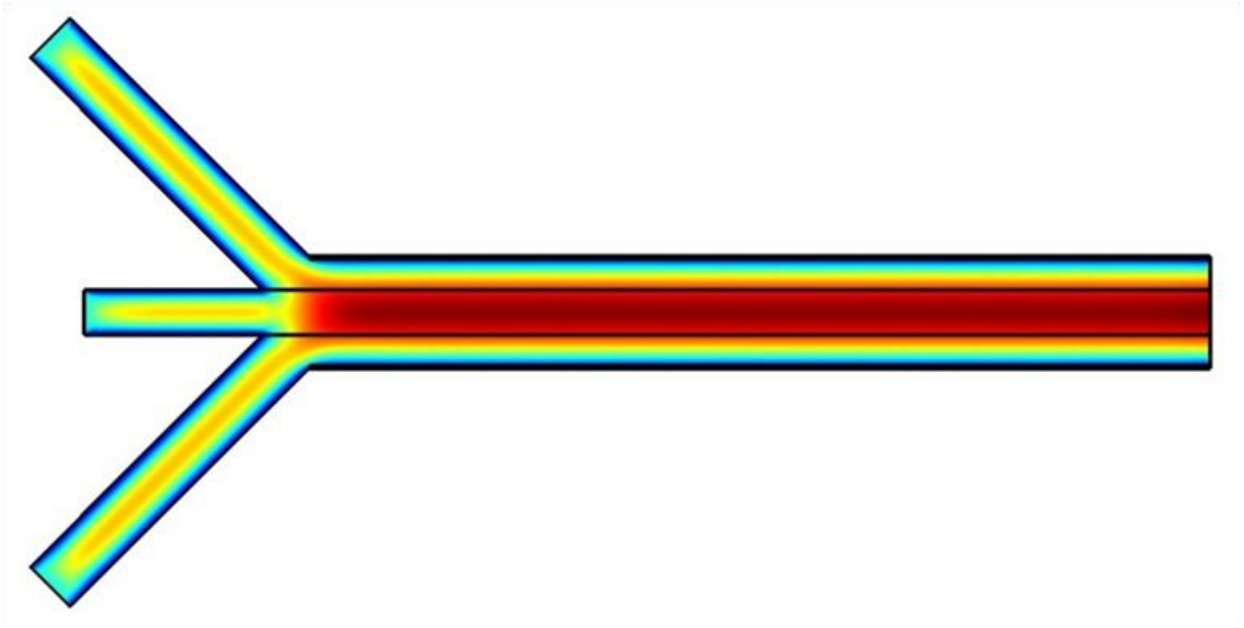

Figure 3.9 A schematic of a microfluidic fuel cell with the third electrolyte stream (this schematic shows the velocity field in the microfluidic fuel cell).

The polarization curve obtained for this design is presented in Figure 3.10. The slight improvement in the polarization curve of the multi-stream laminar flow design is because of the steeper concentration layers and higher ionic conductivity between the anode and cathode. The electric conductivity of the diluted sulfuric acid which has been used in the third flow is assumed to be $47 S.m^{-1}$, and the flow rate is set to $200 \mu l.min^{-1}$. The inlet velocity of the 3rd stream was arbitrarily set to match the inlet velocities of the fuel and oxidant streams. The fuel utilization for this design is 30.07%. The higher fuel utilization of this design compared to the ‘‘Simple square’’ geometry is due to the fact

that the concentration boundary layers are pressed to the channel walls, so the concentration gradients are higher as opposed to what it is in the "Simple square" design. In essence, the higher the concentration gradient, the faster the electrochemical reactions.

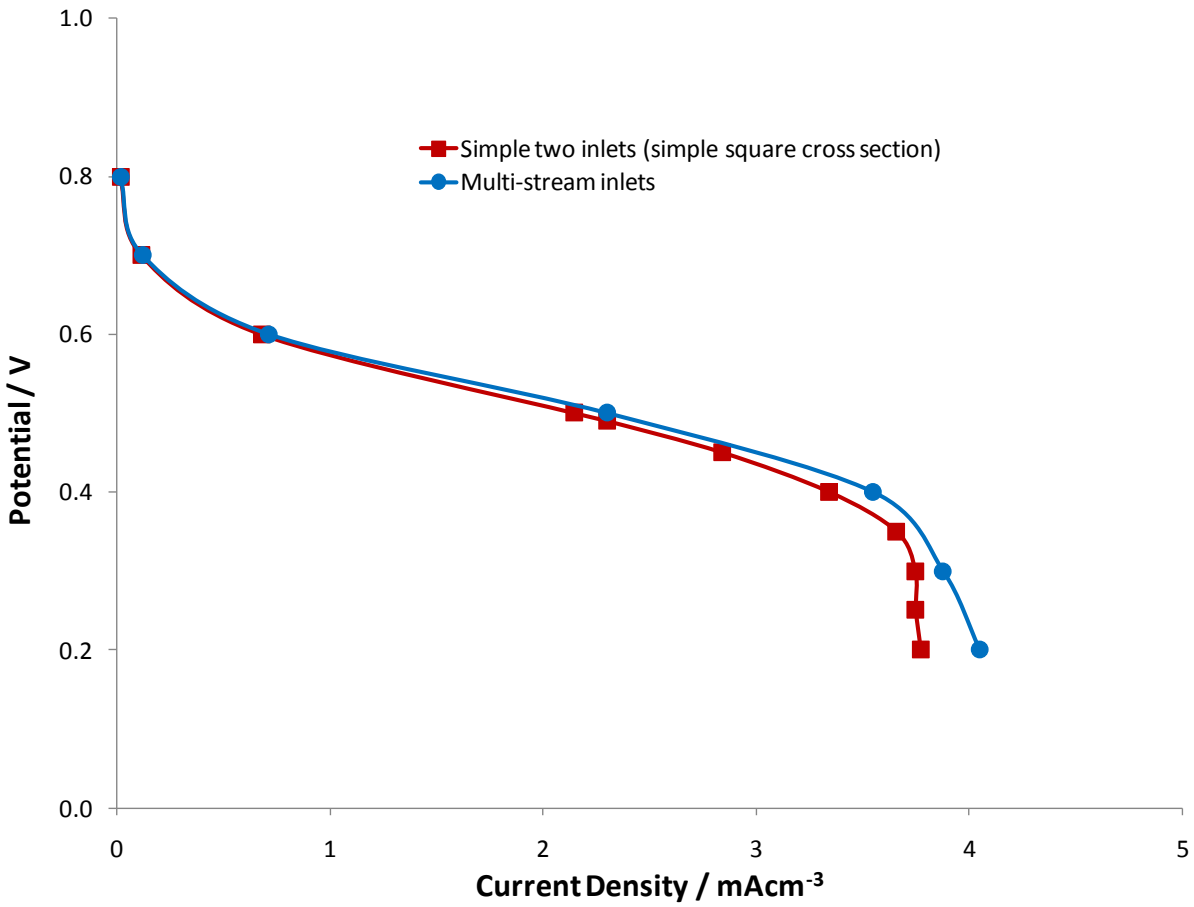

Figure 3.10 The effect of inserting the third flow between the anolyte and catholyte on the polarization curve

3.2.4 Study the Effect of Multiple Inlets

The multiple periodically-placed inlets design shown in Figure 3.11 is also another modification proposed [52] for enhancing the microfluidic fuel cell performance. In this thesis, the performance of this design is compared numerically to that of the standard two-inlet design. Figure 3.12 presents the results. The sudden fall at high current densities in the polarization curve of the simple two-inlet design is due to the mass transfer issue. At high current densities, the reactant consumption rate is much higher than the rate of mass transfer to the electrodes. In the multiple periodically-placed inlets design, on the other hand, the depleted areas are filled constantly with fresh reactants injected from the minor inlets along the channel, which resolves the mass transfer issue. Therefore, there is no sudden drop at high current densities. The total flow rate of this design and the simple two-inlet design is the same; therefore, the mass transport issue is resolved solely by the multiple injections to the depleted areas not by any possible added flow rates. This design turns out to be very useful for the applications in which low voltage with high current density is needed. The fuel utilization is 62.3%. This high fuel utilization is due to the fast replenishment of the depletion regions through the minor inlets.

Figure 3.11 The schematic of a microfluidic fuel cell with multiple periodically-placed inlets. This schematic shows the concentration of the oxidant which is entering from the top side wall of the cell.

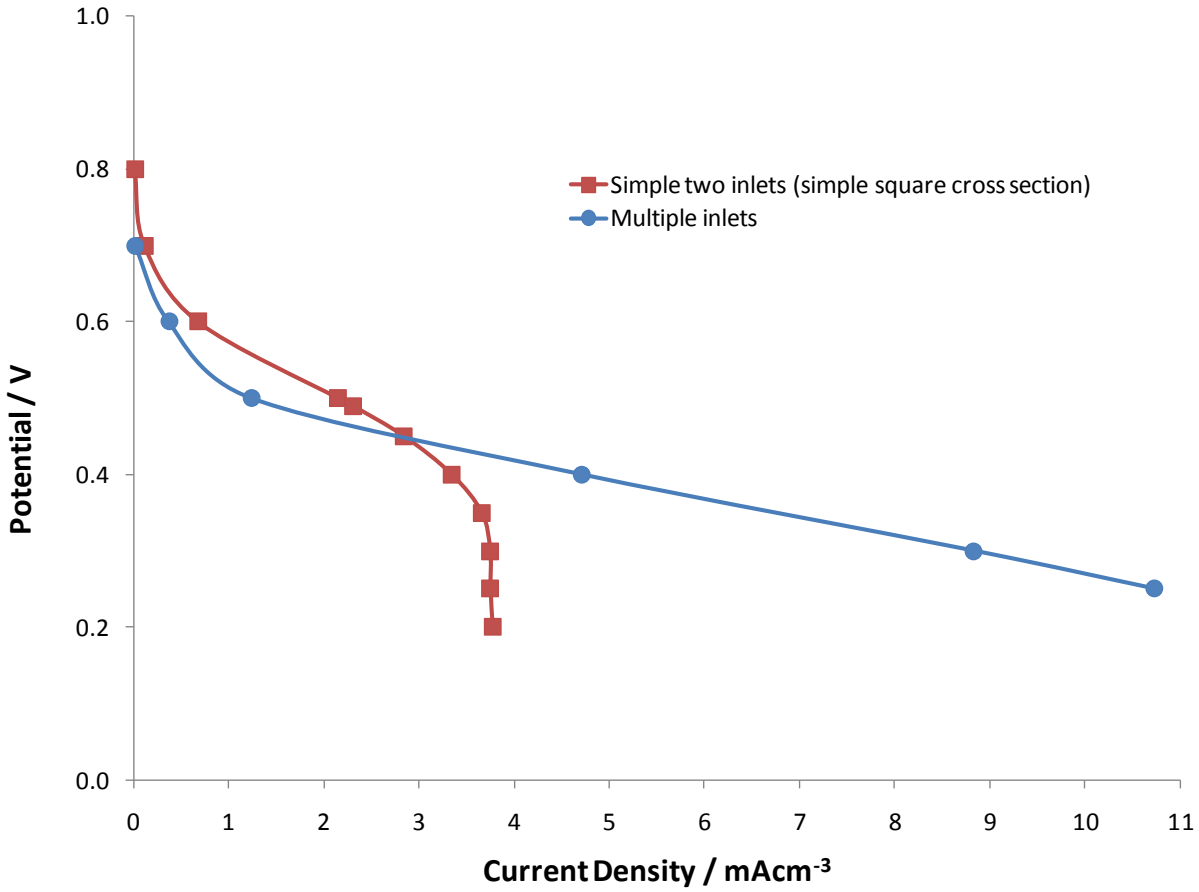

Figure 3.12 The effect of the multiple periodically-placed inlets modification on the polarization curve

3.3 Proposed Geometry

In addition to study the effect of the modifications introduced in the literature [8, 20, 33, 52], the model presented in this thesis is also used to design a new microfluidic fuel cell structure which includes a tapered channel. In this design, the channel height is continuously reduced from 1mm in the beginning to 0.5mm at the outlet. This innovative geometry is suggested based on the development and the growth rate of the mixing region (where the fuel and oxidant meet as the anolyte and catholyte travel down the channel). The growth rate of this mixing region depends on the channel height, so the channel height can continuously be reduced from the inlet to the outlet (i.e., the tapered geometry) to restrict the mixing (inter-diffusion) region growth rate along the channel. This will allow for the extension of the electrodes on the top and the bottom of the channel more toward the middle as the mixing region is thinner in the tapered case. The schematic of this new design is presented in Figure 3.13. This figure shows only the lower half of the cell. For the numerical modeling, the channel is bisected in height to reduce the memory requirement for running the simulation. It is shown that this design incorporates higher electrode surface area inside the microchannel (compared to a non-tapered one), and hence leads to a higher-performance fuel cell.

The mixing region maximum width expression which has been mentioned earlier in Chapter 1 (Eq. (1-1)) implies that by reducing the channel height (which automatically contributes to the increase in the flow velocity) the growth of the mixing region is limited as the fluid travels down the channel. Thus, the channel can be extended further since the diffusion region growth rate is reduced and the crossover happens farther from the inlets. This will also result in the enhancement of fuel utilization. Alternatively, the channel length can be kept constant, and the anode and cathode electrodes can be extended more toward the centre of the channel. The parts of the electrodes which are closer to the inlets are more important in terms of their contribution in the power

generation. Therefore, it is preferred to incorporate more electrode surface area close to the beginning rather than near the end of the channel.

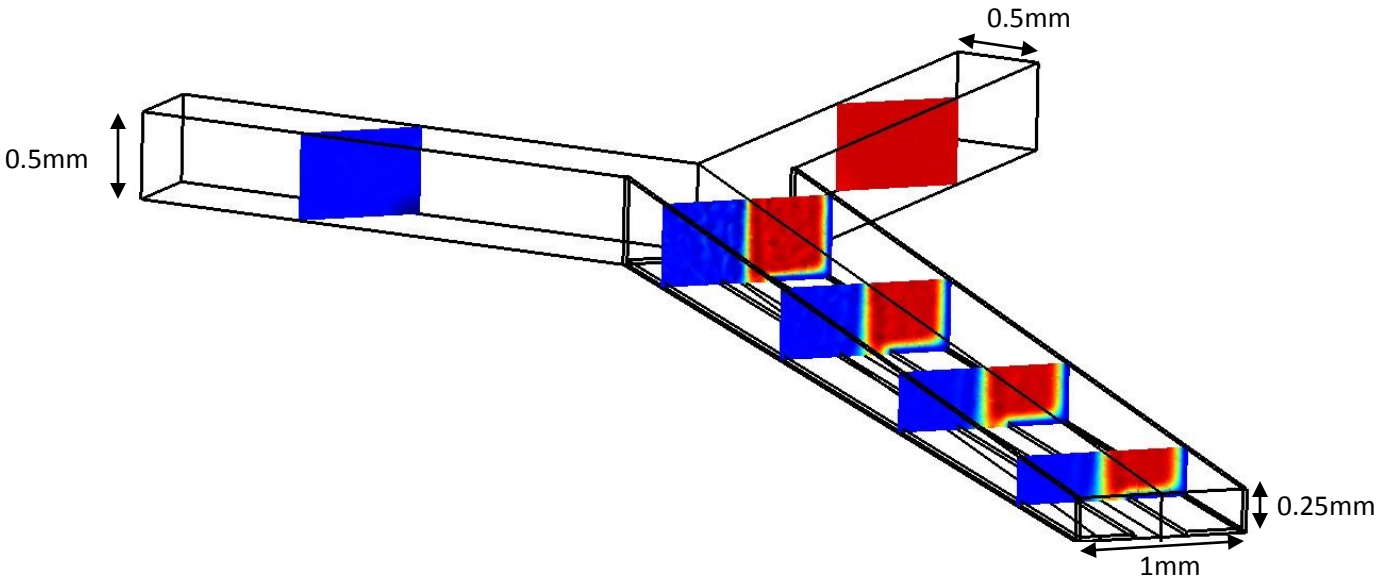

Figure 3.13 The schematic of a microfluidic fuel cell with tapered channel is presented. This figure shows the oxidant concentration profile in the lower half of the channel in different cross-sections along the channel.

A comparison of the mixing regions calculated by the model for the tapered design and the “Extended square” design is shown in Figure 3.14. The figure shows the concentrations of the fuel and oxidant species across the width of the channels at the lower boundary of the outlet cross-section where the mixing region is at its widest extent. Since the concentration boundary layer does not influence the inter diffusion of species across the co-laminar interface, the reaction source terms in the electrode subdomains were removed to make the simulation faster and less memory intensive, and consequently the concentration boundary layers near the electrodes are not shown. However, Figure 3.14 does show that the diffusion of the fuel or oxidant species into the opposite side of the channel is clearly reduced in the tapered design.

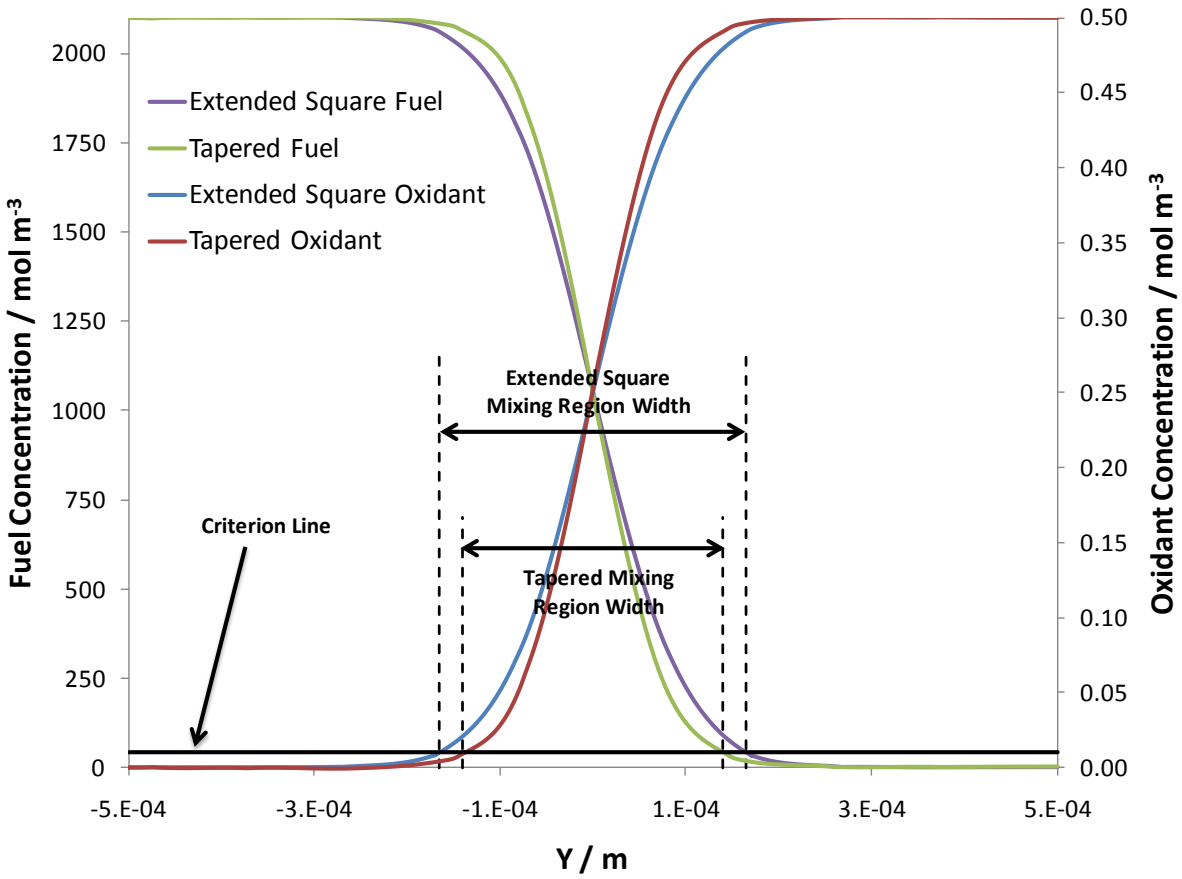

Figure 3.14 A comparison of the mixing region width in the "Extended square" and the proposed tapered geometry is shown. The criterion line indicates 2% of the maximum concentration of the fuel or oxidant which is used to define the width of the mixing region.

In this work, the mixing region thickness is defined as the distance over which the concentration of the fuel or oxidant falls to 2% of its maximum value. Using this definition, the mixing region in the tapered channel is found to be 0.04mm thinner. Since the electrodes must not overlap with the mixing region in order to avoid crossover, the smaller mixing region in the tapered channel allows the anode and cathode to be extended an additional 0.02mm towards the center of the channel. This extension creates 0.32mm^2 of additional anode or cathode areas in the 8mm long channel. The increased active area increases the cell current density as shown in Figure 3.15. The new tapered design also enhances the fuel utilization by up to four times.

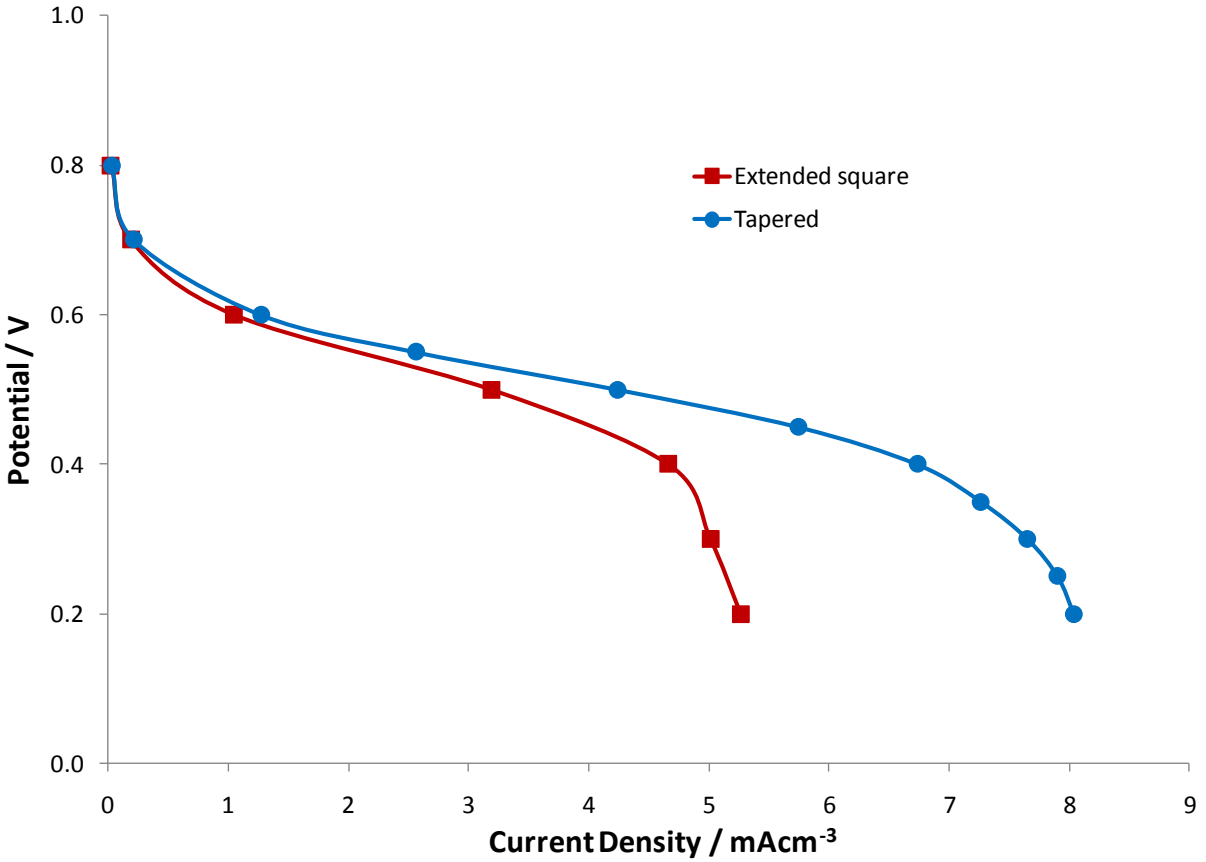

Figure 3.15 The effect of tapering the channel on the polarization curve is shown. The tapered channel provides an opportunity to install more active surface areas inside the channel by reducing the mixing region width over a certain length.

4. Results for Microfluidic Fuel Cells with Flow-Through Porous Electrodes

4.1 Introduction

The model developed in this research is also used to study the performance of the microfluidic fuel cells consisting of porous electrodes (instead of solid electrodes shown in Chapter 3). Kjeang et al. [36] has proposed two designs for microfluidic fuel cells with porous carbon electrodes. In the first design, the co-laminar streams of the fuel and oxidant solutions flow over the electrodes which are mounted on the channel walls similar to a typical microfluidic fuel cell. In the second design, the penetration of the fuel and oxidant solutions into the electrodes is increased by forcing the fluids to flow through the porous material before meeting in a central channel and establishing the co-laminar flow travelling toward the outlet (see Figure 4.1). Electromigration of ions across this co-laminar stream is responsible for charge transfer between the anode and cathode. In both cases, the porous-structured electrodes improve fuel utilization by increasing the active surface area without significant parasitic pumping load [32]. It is possible to reach to almost 100% fuel utilization with this design. For this fuel utilization, however, low flow rate and low cell voltage are required. Among the two designs for the microfluidic fuel cell with porous electrodes, the flow-through design has been shown to have higher fuel utilization and lower mass transport losses compared to the flow-over design [36]. Thus, it considered for further study in this thesis.

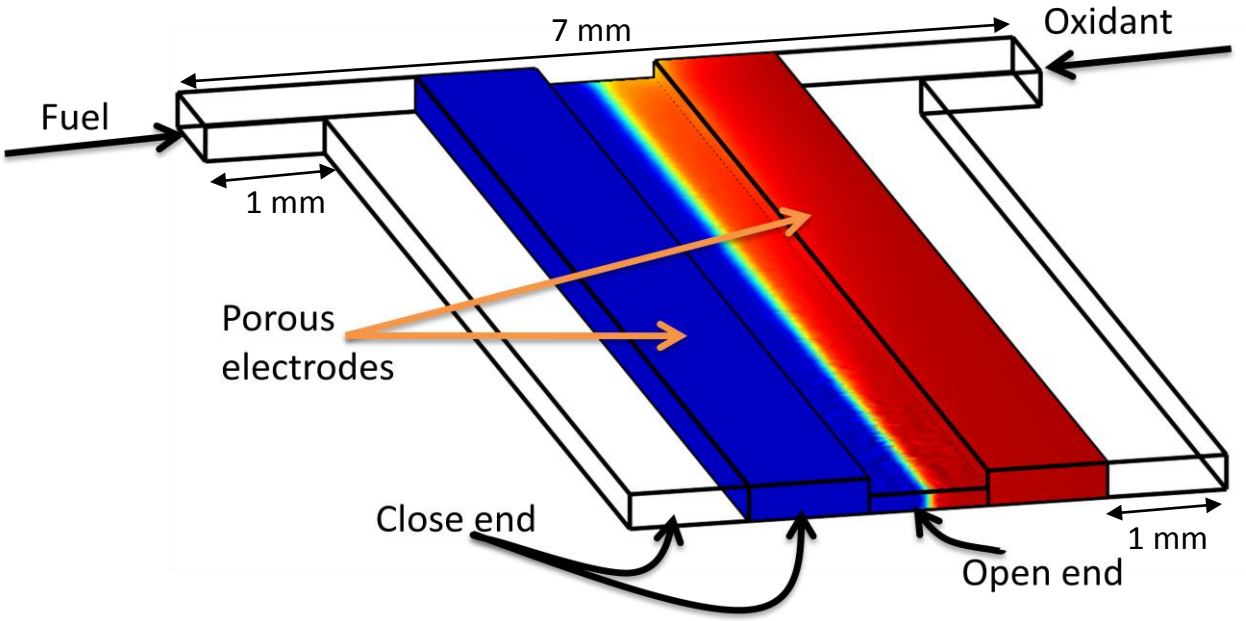

Figure 4.1 A schematic of a microfluidic fuel cell with flow-through porous electrodes

In this work, attempts are made to refine the design of the microfluidic fuel cell with porous electrodes by investigating the effect of the inlet velocity and the electrode porosity on the power density. As expected, higher velocities result in higher power densities. For the porosity, however, there is an optimum value. In the typical range of porosity (less than about 93%), there is a trade-off between the available electrode surface area and electric conductivity of the solid phase (i.e., the porous carbon electrode). For the porosity values above 93% (which is the reference porosity, ε_0, in our model), both available active surface area and solid-phase electric conductivity decrease by increasing the porosity; however, the electrolyte-phase electric conductivity will increase.

In this chapter, a model of a microfluidic fuel cell with flow-through porous electrodes using vanadium redox couples as the fuel and oxidant is presented. As it is

stated in Chapter 1, there are some advantages associated with the use of vanadium redox species such as high open-circuit potential (up to 1.7V at uniform PH [16]), high solubility (up to 5.4M) causing more species available to the electrodes [51], and no requirements for expensive precious metal catalysts for oxidation and reduction reactions [16]. Thus, the reactions can take place on bare carbon electrodes. The electrochemical reactions for the anolyte and catholyte streams are:

$$\text{Anode:} \qquad V^{2+} \Leftrightarrow V^{3+} + e^{-} \tag{4-1}$$

$$\text{Cathode:} \quad VO_2^{+} + 2H^{+} + e^{-} \Leftrightarrow VO^{2+} + H_2O \tag{4-2}$$

Microfluidic fuel cells using vanadium species in both half cells benefit from a rapid and balanced electrochemical system in terms of species transport characteristics and reaction rates [36]. In these systems, the fuel and oxidant can be regenerated from a mixture of the products without separation since they use the same species (Vanadium) as oxidant and reductant [19].

4.2 Modeling

4.2.1 Geometry

The geometry of the microfluidic fuel cell modeled here is created based on a study conducted by Kjeang et al. [36]. The geometry comprises two carbon strips as porous electrodes. The electrodes are 12-mm long, 1-mm wide and 300-μm thick. The depth of the channel from which the fuel and oxidant are fed is also 300μm. The middle channel located between the two porous electrodes is 150-μm deep. More details on the dimensions of the channel can be found in Figure 4.1.

4.2.2 Governing Equations

The governing equations for modeling of the microfluidic fuel cell with porous electrodes are covered in Chapter 2 (i.e., mass transport, momentum transport and reaction kinetics equations). There are, however, some modifications made into these equations to describe the physical phenomena in the porous media. Similar to Chapter 2, the incompressible flow and isothermal conditions are applied here. The effects of gravity and osmotic drag are neglected, and hence the incompressible Navier-Stokes equation can be applied to model the fluid flow in the channels. In the porous electrodes, however, the Brinkman equations are used to model the fluid flow. These equations are appropriate based on the assumption that the physical properties of the electrodes and electrolytes are isentropic and homogeneous. The Brinkman equations used here are essentially the Navier-Stokes equations with an added momentum source term to account for the resistance against the flow in the porous media. Below

are the momentum balance and continuity equations which are used to describe the fluid flow:

$$\nabla . v = 0 \tag{4-3}$$

$$\rho(v . \nabla v) = -\nabla p + \mu \nabla^2 v - \frac{\mu}{K} \varepsilon v \tag{4-4}$$

In these equations K and ε represent the permeability (m^2) and porosity of porous medium respectively.

The Brinkman equation (Eq. 4.4) is integrated into the ‘‘Incompressible Navier-Stokes’’ application mode which is under the ‘‘Chemical Engineering Module’’ of COMSOL. In the ‘‘Subdomain Settings’’ dialogue box of this application mode, there is a ‘‘Flow in porous media (Brinkman equations)’’ check box (see Figure 4.2). By selecting this option it is possible to switch between free flow and porous media flow in a given subdomain. This application mode is particularly beneficial to our modeling since our model is a combination of porous media (electrodes) and free flow (microchannels) subdomains.

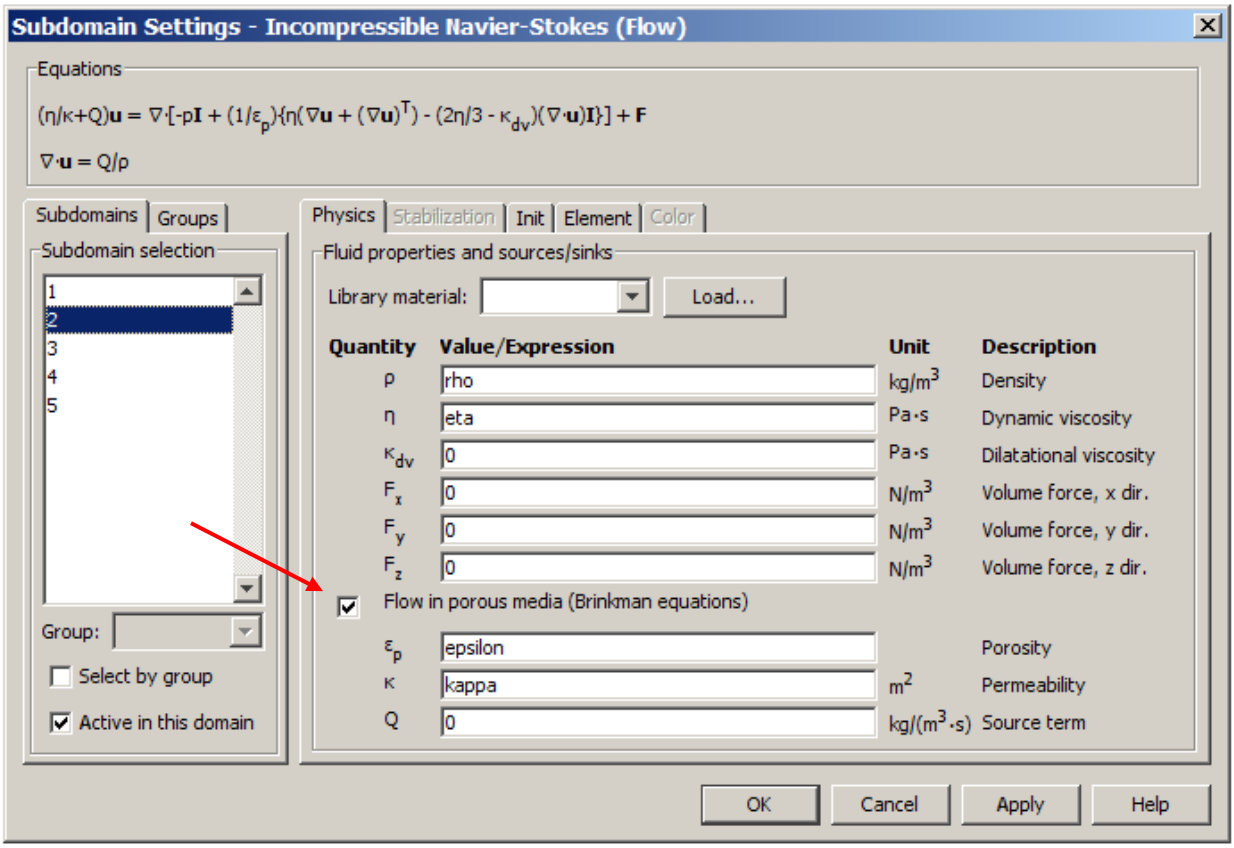

Figure 4.2 The "Incompressible Navier-Stokes" application mode should be selected from the "Chemical Engineering" mode to have the porous media option (Brinkman equations).

The permeability of the porous electrodes is defined by the Carman-Kozeny (CK) equation, which is one of the most commonly-used models used to describe the porous media permeability in the literature [63]. This equation is only valid for laminar flow and is given as:

$$K = \frac{d_f^2 \varepsilon^3}{16 k_{CK} (1-\varepsilon)^2} \tag{4-5}$$

where, d_f is the fibre diameter, ε is the porosity and k_{CK} is the Carman-Kozeny constant which depends on the type of the medium and is an empirical parameter which

is found based on the best fit between the above relationship and the experimental permeability values [64].

The same potential equations as described in Chapter 2 (i.e., the "Conductive Media DC" module) are also used to model the electric fields based on the conservation of electrical charges. The only difference is that the effective value of the electric conductivities must be used to account for the porosity effects. These effective values of the electric conductivity for the solid and electrolyte phases are calculated through the following equations [65]:

$$\sigma_s^{eff} = (1-\varepsilon)^{3/2}\sigma_s \quad (4\text{-}6)$$

$$\sigma_e^{eff} = \varepsilon^{3/2}\sigma_e \quad (4\text{-}7)$$

The electric conductivity of the Toray carbon paper (TGPH-090), σ_S, is considered 15000 $S.m^{-1}$ [66]. This value is far less than what was considered for metallic electrodes (10^7 $S.m^{-1}$) in Chapter 2. As a result, the fixed potential boundary conditions will not contribute to an essentially uniform solid phase voltage, φ_S, anymore. This is particularly true for high current densities. This phenomenon will lead to slightly different reaction rates at different parts of electrodes. The reaction rates would be somewhat higher near the beginning of the electrodes where the electrodes are attached to the wires. The higher depletion of oxidant near the current collector is shown in Figure 4.3. This is an evidence for this increased reaction rate.

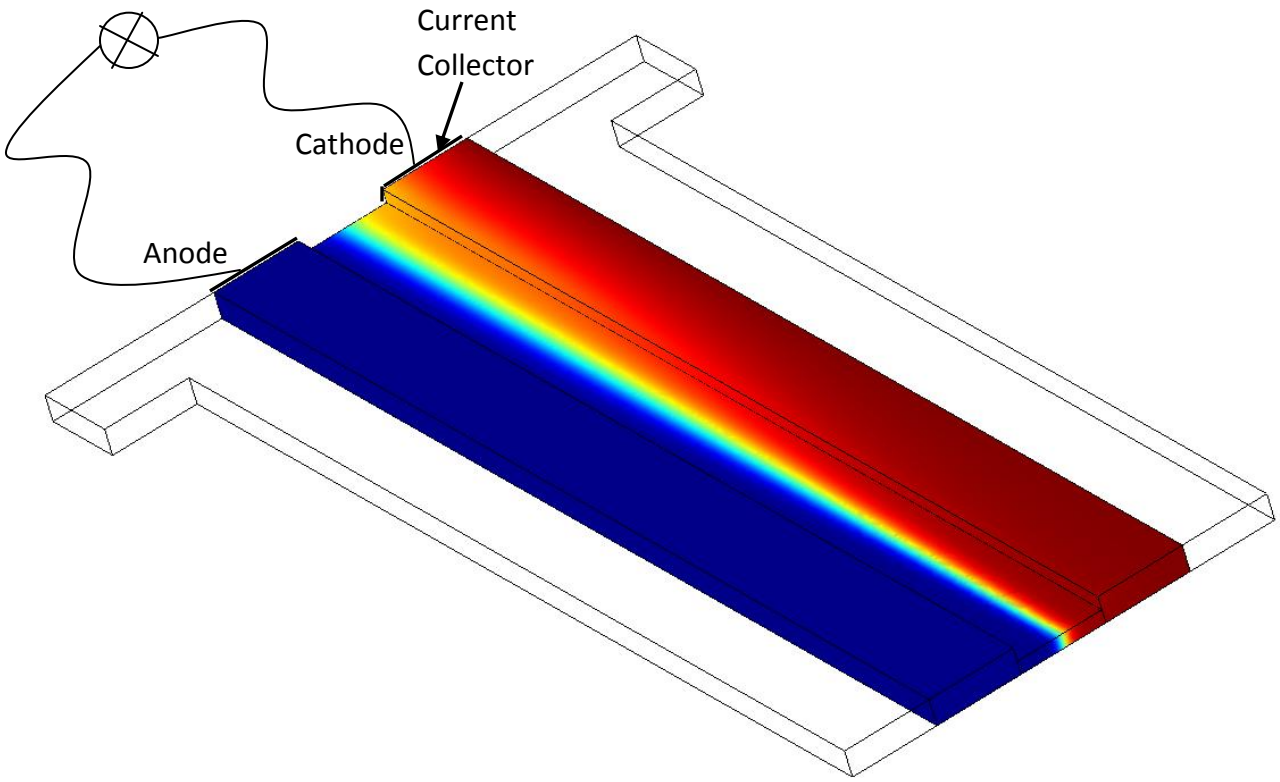

Figure 4.3 Relatively low electric conductivity of porous electrodes results in non-uniform reaction rates over the entire electrode domain. This schematic depicts how this phenomena leads to more depletion near the cathode current collector. The color plot shows the oxidant concentration.

In the presented microfluidic fuel cell with cross-flow of reactants, the reactant species are transported through the electrodes mainly by convection. Because the entire fuel or oxidant stream flows through the electrode region where the active sites are readily available, the fuel cell is able to achieve very high fuel/oxidant utilization. This is not the case for the typical microfluidic fuel cell with flow-over the electrodes in which diffusive transport in a direction transverse to the flow is necessary to replace reactant species in the vicinity of the electrodes as they are consumed during the reaction. Since the diffusive transport is inherently slow compared to the convective transport through the cell (consisting the solid electrode), only a small portion of the

reactants is able to reach the active surface areas of the electrodes, and hence the cell has relatively poor fuel utilization. Notwithstanding this difference in the operation of the two types of fuel cells, the reactant concentration distributions in the flow-through architecture can still be modeled using the "Convection-Diffusion" module in Comsol which describes both of the dominant mass transport mechanisms (i.e., convective and diffusive mass transport). The only difference compared to what was used for the fuel cell with solid electrodes is that the diffusion coefficient must be replaced by the effective diffusion coefficient which can be calculated directly by using the Bruggeman correlation:

$$D_{eff} = \varepsilon^{3/2} D \tag{4-8}$$

Regarding the reaction kinetics, the specific surface area in the Butler-Volmer equation, a, is related to the porosity and is calculated through the equation below [67]:

$$a = \left(\frac{\varepsilon}{\varepsilon_0} \right)^{0.75} A_e \tag{4-9}$$

where, ε_0 and A_e are the reference values for the porosity and specific surface area, respectively. Their values are given in Table 4.1.

The current density is obtained in post processing by integrating the normal current density on the cathode boundaries and normalizing it by the vertically projected area of the electrode (i.e., 12mm × 1mm) in order to be consistent with the experimental results used for the validation of this model [36]. However, it is reasonable to normalize

the current and power densities by the overall fuel cell volume (see Chapter 3). The normalization based on the volume is more realistic and providing more information from the design point of view since the ultimate goal in designing the microfluidic fuel cell is to fabricate a compact, yet powerful device.

Table 4.1 The Constants Used in the Anodic and Cathodic Flows for Porous Electrode Design

Parameter	Anode	Cathode
Density, ρ[1]	1410 kg.m^{-3}	
Dynamic viscosity, μ[1]	5.67e-3 Pa.s	
Faraday constant, F	96485.34 C.mol^{-1}	
Cell temperature, T	298 K	
Universal gas constant, R	8.314 J.mol^{-1}K^{-1}	
Ionic conductivity, σ_e[1]	59 S.m^{-1}	59 S.m^{-1}
Ref. Concentration, c_{REF}	1000 mol.m^{-3}	1000 mol.m^{-3}
Diffusion coefficient, D[4]	9.78e-9 m^{2}s^{-1}	9.78e-9 m^{2}s^{-1}
Charge transfer coefficient, α[2]	0.5	0.5
Number of electrons transferred, n	1	1
Exchange current density, i_0	19.7 A.m^{-2}	139 A.m^{-2}
Open circuit potential, OCP	-0.496 V	0.750 V
Inlet concentration, c_0[3]	2000 mol.m^{-3}	2000 mol.m^{-3}
Reference porosity, ε_0[2]	0.929	
Reference specific surface area, A_e[5]	1.62e4 m^{-1}	

(1) The value is obtained from [68];

(2) The value is obtained from [69];

(3) The value is obtained from [36];

(4) An estimated value is assumed based on [70] to fit to the experimental results [36].

(5) The value is obtained from [71].

4.3 Results

The results obtained from the developed numerical model are presented in Figure 4.4. The results were obtained for two different flow rates (i.e., 60μL.min^{-1} and 300μL.min^{-1}). The numerical results presented with solid lines are compared to the experimental data presented by dashed lines. In general, the numerical results follow the same trend as the experimental data. Quantitatively, the polarization values are also in good agreement with the experimental values. In low current densities, any minor deviation of the numerical results from the experimental data can be attributed to discrepancies between the actual exchange current density and the value assumed in the model. As it has been mentioned in Chapter 3, the true value of exchange current density depends on many different factors which makes it difficult to ascertain the exact value. There is also some deviation from the experimental results observed in the very high current density region. It is clear from the polarization curves that the performance of the fuel cell with porous electrodes is ohmic loss-dominated. Thus, the deviation seems to be primarily due to inaccurate assumptions associated with ohmic losses. One of these approximations is that the electrolyte conductivity was assumed to be a specific constant value which is not changing with the electrolyte concentration. In fact, the electrolyte conductivity is varying as the solution composition changes (due to the reactants consumption by redox reactions), so the actual conductivity is lower than the original conductivity value which is used in the model (see the constants in Table 4.1). The reason that the deviation becomes more distinct in the high flow rates is due to the fact that in these flow rates the electrochemical reaction rates become faster which

result in more severe changes in the electrolyte composition and consequently more significant impact on the electrolyte conductivity. Also, the ohmic losses are directly proportional to both the cell resistance and current drawn; thus, the impact of any error in the approximation of conductivity will be more significant at high current densities. As a result, the current densities calculated by the numerical simulation deviate more from the experimental results at higher flow rates as the difference between the originally-assumed and actual conductivity values grows. For the practical cell voltages (i.e., around 0.8V), however, the unvarying electrolyte conductivity assumption holds since at this potential the reaction rates are not high enough to contribute to the large difference between the original and actual values of electrolyte conductivity.

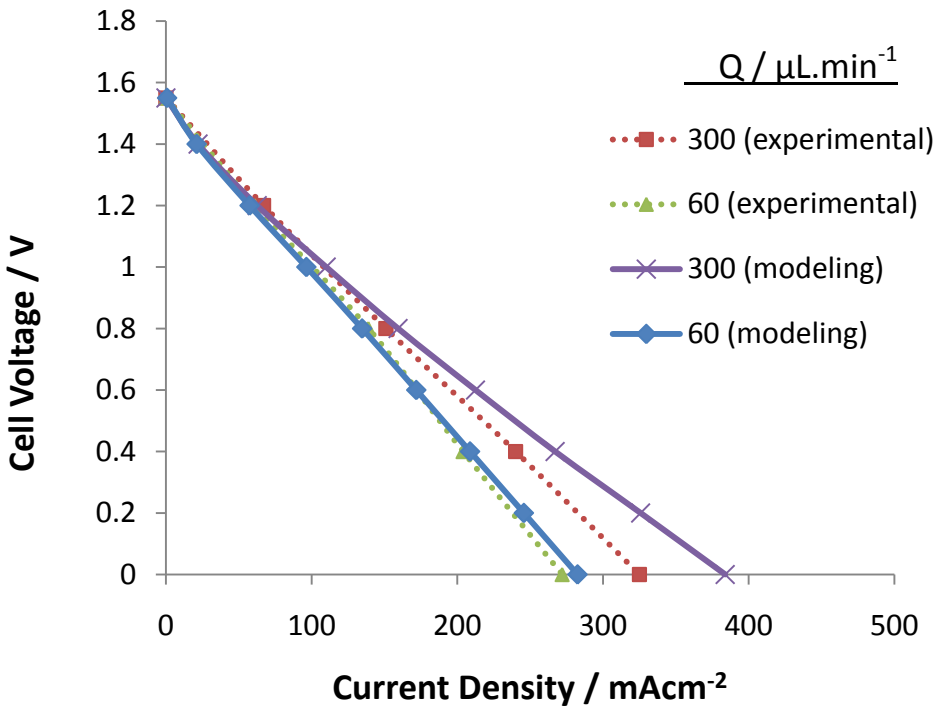

Figure 4.4 This figure presents the polarization curves of the microfluidic fuel cell with flow-through porous electrodes. The numerical results are in good agreement with those obtained from experiments [36].

Using the above model, the effect of porosity has also been investigated. The experimental conditions reported in [36] were used to study the effect of the porosity on the available power output which is defined as the difference between the total power produced and the parasitic power consumed for pumping the electrolyte. The formula used to calculate the available power output is given as

$$Available\ Power\ Output = V.I - Q.\Delta p \quad (4\text{-}10)$$

where, V and I represent the cell voltage and total current respectively.; therefore, $V.I$ reflects the total power produced. Q is the total electrolyte flow rate and Δp denotes the pressure difference across the porous electrodes; therefore, $Q.\Delta p$ gives parasitic pumping power.

The results presented in Figure 4.5 show that the porosity value of 0.67 is the optimal value. The goal of this study is to determine the porosity for which the net/available power output is maximum. In this investigation, all of the operational parameters such as temperature and electrolyte flow rate and the material properties such as electrical conductivity of the electrolytes and electrodes remain constant and only the variation of the porosity is studied. This represents a set of experiments in which only the porous carbon electrodes are replaced in each experiment and other affecting operational and experimental factors are constant. For example a constant value of 300μL.min^{-1} is selected for the electrolyte flow rate since it gives the lowest overpotentials as presented in Figure 4.4. The temperature is assumed to be 25°C (i.e., typical room temperature) for all of the values obtained.

As it is mentioned earlier, only the porosity values are varying from one simulation run to another. The porosity value has a direct effect on some parameters such as pressure drop across the porous electrode (Δp), the effective diffusion coefficient (D_{eff}), the effective electric conductivity of the electrolyte (σ_e^{eff}) and the electrodes (σ_s^{eff}), and the available surface area (a). Any variation or changes in these parameters would affect the final power output. As a result, porosity influences the net power output through changing the above-mentioned parameters. For example, low porosity increases the pressure drop across the porous electrode which leads to higher parasitic power loss to drive the electrolyte, and at the same time, it significantly reduces the active surface area which causes the electrochemical reactions to slow down (see Eq. (4-9)).

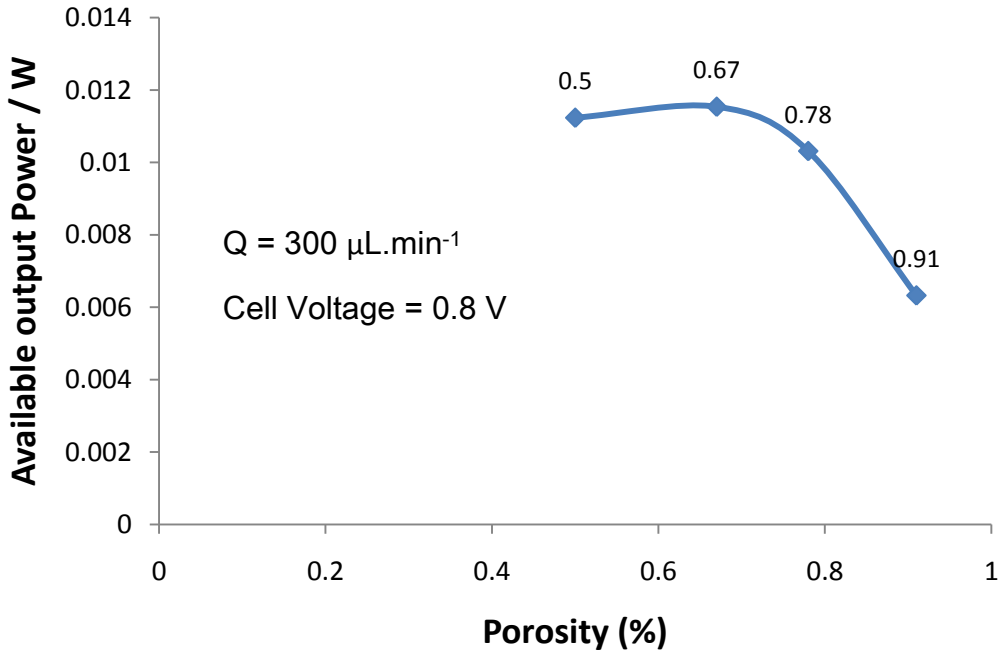

Figure 4.5 The effect of the porosity on the fuel cell net power output

5. Conclusions and Suggestions for Future Work

5.1 Conclusions

In this thesis, a comprehensive numerical study has been conducted to compare the performance of different microfluidic fuel cell designs reported in the literature (i.e., microfluidic fuel cells with different cross-section aspect ratios and electrode configurations, multi-stream laminar flow microfluidic fuel cells, fuel cells with multiple periodically-placed inlets and microfluidic fuel cell with porous electrodes). Polarization curves were obtained by solving equations describing the fluid flow, mass transport, and electric charge conservation during fuel cell operation using COMSOL Multiphysics. The results show that changing the cross-section aspect ratio has a significant impact on the cell performance. Specifically, it was found that cross-sections with either high or low aspect ratios are better than the square ones. At a very high current density (i.e., 8mA.cm^{-3} or even higher) the low aspect ratio geometry is proven to perform better whereas the high aspect ratio structure performs slightly better at lower current densities.

Adding the third flow between the anode and cathode contributes to a small improvement in the polarization curve. However, with the use of the numerical model developed in this thesis, it was verified that implementing multiple periodically-placed inlets has a great positive impact on the polarization curve. This design depicts 62.3% fuel utilization at a selected voltage value (say 0.45V). This high fuel utilization which

finally leads to high power generation (in a fixed potential) is due to the fast replenishment of the depletion area at the vicinity of the electrodes by the minor inlets.

The model developed in this thesis was also used to study further the performance of microfluidic fuel cells using porous electrodes. It has been shown in previous studies that the microfluidic fuel cell with flow-through porous electrodes is a promising design as it enhances fuel utilization and produces high power density compared to typical designs which use flow-over electrodes. In this thesis, modeling of a microfluidic fuel cell incorporating flow-through porous electrodes was presented. The results of the numerical model were verified against those reported from the experimental studies. It is possible to reach to almost 100% fuel utilization with this design. For this fuel utilization, however, low flow rates and low cell voltages are required. The effect of the electrode porosity was also investigated, and it is shown that 67% porosity is the optimum value for the given conditions.

In conclusion, the numerical model presented in this study is a valuable tool, as it can be used to investigate the effect of any design modifications on the cell performance before fabricating and testing the new design in an extensive and difficult experimental study. For instance, the model was used to test the performance of a new structure which includes a tapered channel. It has been found that the proposed tapered channel design has a great influence on the polarization curve and fuel utilization. By tapering the channel it is possible to restrict the mixing region growth rate and incorporate wider electrodes on the bottom and top walls of the channel without

causing reactant crossover. The proposed modification is shown to increase the fuel utilization up to four times and significantly improve the current density at low cell voltages.

5.2 Future Work

The numerical model developed in this work can be used to improve the design of microfluidic fuel cells to achieve higher fuel utilization and power density. In addition to testing the viability of novel designs, it is suggested to further investigate and optimize the performance of the various microfluidic fuel cell designs proposed in the literature. For instance, in this work, the ‘‘Low aspect ratio’’ structure is shown to be capable of accommodating larger active surface area. On the other hand, the ‘‘High aspect ratio’’ design is advantageous since it has lower ionic resistance. Therefore, there should be an optimum aspect ratio which produces the highest power density. As a future study, it is suggested to develop a closed-loop numerical model capable of testing different aspect ratios and determining the aspect ratio which produces the highest power density.

There are also some design modifications in the literature that have not been examined in this study. For example, there is no numerical model developed so far to investigate the air-breathing cathode design proposed by [29].

Future studies based on this work can also include changes to the numerical model to describe certain phenomena which impose limitations on specific fuel cell designs. As an example, the performance of direct hydrogen peroxide microfluidic fuel cell is primarily hampered by the oxygen evolution in the cathode that could perturb the co-laminar interface [72]. In order to achieve practical implementations of this technology, it seems essential to develop an accurate numerical model of the hydrogen

peroxide fuel cell which incorporates two-phase flow modelling to study the formation of oxygen bubbles in the electrolyte and the impact of the these bubbles on the stability of the co-laminar flow. A numerical model of the hydrogen peroxide fuel cell has been developed by Chen et al. [58] to examine different geometries, but in that model the oxygen bubbles produced from cathodic reaction is not considered.

Future work in the field of the microfluidic fuel cell can also be extended to cover the experimental efforts in this area. For instance, the fabrication of the novel design proposed in this thesis (i.e., tapered channel) is suggested for future studies.

6. References

[1] O. Principles, "by Vijay Ramani," *Electrochemical Society Interface,* pp. 41, 2006.

[2] C. BOGUŞ, "FUEL CELL–A CONCEPTION IN WEAR OR A HOPEFUL FUTURE FOR RENEWABLE SOURCES OF ENERGY?" .

[3] C. Dyer, "Fuel cells for portable applications," *J. Power Sources,* vol. 106, pp. 31-34, 2002.

[4] F. Barbir, "PEM fuel cells," *Fuel Cell Technology,* pp. 27-51, 2006.

[5] J. Larminie, A. Dicks and M. S. McDonald, "Fuel cell systems explained," 2003.

[6] M. Perry and T. Fuller, "A historical perspective of fuel cell technology in the 20th century," *J. Electrochem. Soc.,* vol. 149, pp. S59, 2002.

[7] S. Srinivasan, *Fuel Cells: From Fundamentals to Applications.* Springer Verlag, 2006.

[8] A. Bazylak, D. Sinton and N. Djilali, "Improved fuel utilization in microfluidic fuel cells: A computational study," *J. Power Sources,* vol. 143, pp. 57-66, 2005.

[9] R. Hahn, S. Wagner, A. Schmitz and H. Reichl, "Development of a planar micro fuel cell with thin film and micro patterning technologies," *J. Power Sources,* vol. 131, pp. 73-78, 2004.

[10] G. McLean, N. Djilali, M. Whale and T. Niet, "Application of micro-scale techniques to fuel cell systems design," in *Proceedings of the 10th Canadian Hydrogen Conference Quebec City,* 2000, pp. 349–358.

[11] J. Yu, P. Cheng, Z. Ma and B. Yi, "Fabrication of a miniature twin-fuel-cell on silicon wafer," *Electrochim. Acta,* vol. 48, pp. 1537-1541, 2003.

[12] S. Lee, A. Chang-Chien, S. Cha, R. O'hayre, Y. Park, Y. Saito and F. Prinz, "Design and fabrication of a micro fuel cell array with "flip-flop" interconnection," *J. Power Sources,* vol. 112, pp. 410-418, 2002.

[13] J. Yeom, G. Mozsgai, B. Flachsbart, E. Choban, A. Asthana, M. Shannon and P. Kenis, "Microfabrication and characterization of a silicon-based millimeter scale, PEM fuel cell operating with hydrogen, methanol, or formic acid," *Sensors Actuators B: Chem.,* vol. 107, pp. 882-891, 2005.

[14] A. Ozbek, "POWER-GREATER COMPLEXITY SHAPES POWER DESIGNS-POWER SUPPLIES-Bright Outlook For Micro Fuel Cells Despite Challenges," *Electronic Design,* vol. 51, pp. 102-106, 2003.

[15] C. Hebling and A. Heinzel, "Portable fuel cell systems," *Fuel Cells Bulletin,* vol. 2002, pp. 8-12, 7/1, 2002.

[16] E. Kjeang, N. Djilali and D. Sinton, "Microfluidic fuel cells: A review," *J. Power Sources,* 2008.

[17] E. R. Choban, L. J. Markoski, A. Wieckowski and P. J. A. Kenis, "Microfluidic fuel cell based on laminar flow," *J. Power Sources,* vol. 128, pp. 54-60, 2004.

[18] R. F. Ismagilov, A. D. Stroock, P. J. A. Kenis, G. Whitesides and H. A. Stone, "Experimental and theoretical scaling laws for transverse diffusive broadening in two-phase laminar flows in microchannels," *Appl. Phys. Lett.,* vol. 76, pp. 2376, 2000.

[19] R. Ferrigno, A. D. Stroock, T. D. Clark, M. Mayer and G. M. Whitesides, "Membraneless vanadium redox fuel cell using laminar flow," *J. Am. Chem. Soc.,* vol. 124, pp. 12930-12931, 2002.

[20] M. H. Chang, F. Chen and N. S. Fang, "Analysis of membraneless fuel cell using laminar flow in a Y-shaped microchannel," *J. Power Sources,* vol. 159, pp. 810-816, 2006.

[21] J. L. Cohen, D. J. Volpe, D. A. Westly, A. Pechenik and H. D. Abruña, "A dual electrolyte H2/O2 planar membraneless microchannel fuel cell system with open circuit potentials in excess of 1.4 V," *Langmuir,* vol. 21, pp. 3544-3550, 2005.

[22] S. M. Mitrovski, L. C. C. Elliott and R. G. Nuzzo, "Microfluidic Devices for Energy Conversion: Planar Integration and Performance of a Passive, Fully Immersed H2− O2 Fuel Cell," *Langmuir,* vol. 20, pp. 6974-6976, 2004.

[23] S. M. Mitrovski and R. G. Nuzzo, "A passive microfluidic hydrogen–air fuel cell with exceptional stability and high performance," *Lab on a Chip,* vol. 6, pp. 353-361, 2006.

[24] W. Sung and J. W. Choi, "A membraneless microscale fuel cell using non-noble catalysts in alkaline solution," *J. Power Sources,* vol. 172, pp. 198-208, 2007.

[25] E. Choban, J. Spendelow, L. Gancs, A. Wieckowski and P. Kenis, "Membraneless laminar flow-based micro fuel cells operating in alkaline, acidic, and acidic/alkaline media," *Electrochim. Acta,* vol. 50, pp. 5390-5398, 2005.

[26] E. R. Choban, P. Waszczuk and P. J. A. Kenis, "Characterization of limiting factors in laminar flow-based membraneless microfuel cells," *Electrochemical and Solid-State Letters,* vol. 8, pp. A348, 2005.

[27] R. S. Jayashree, D. Egas, J. S. Spendelow, D. Natarajan, L. J. Markoski and P. J. A. Kenis, "Air-breathing laminar flow-based direct methanol fuel cell with alkaline electrolyte," *Electrochemical and Solid-State Letters,* vol. 9, pp. A252, 2006.

[28] E. Kjeang, A. G. Brolo, D. A. Harrington, N. Djilali and D. Sinton, "Hydrogen Peroxide as an Oxidant for Microfluidic Fuel Cells," *J. Electrochem. Soc.,* vol. 154, pp. B1220, 2007.

[29] R. S. Jayashree, L. Gancs, E. R. Choban, A. Primak, D. Natarajan, L. J. Markoski and P. J. A. Kenis, "Air-breathing laminar flow-based microfluidic fuel cell," *J. Am. Chem. Soc.,* vol. 127, pp. 16758-16759, 2005.

[30] A. Li, S. H. Chan and N. T. Nguyen, "A laser-micromachined polymeric membraneless fuel cell," *J Micromech Microengineering,* vol. 17, pp. 1107, 2007.

[31] J. L. Cohen, D. A. Westly, A. Pechenik and H. D. Abruña, "Fabrication and preliminary testing of a planar membraneless microchannel fuel cell," *J. Power Sources,* vol. 139, pp. 96-105, 2005.

[32] E. Kjeang, R. Michel, D. A. Harrington, D. Sinton and N. Djilali, "An alkaline microfluidic fuel cell based on formate and hypochlorite bleach," *Electrochim. Acta,* vol. 54, pp. 698-705, 2008.

[33] M. Sun, G. Velve Casquillas, S. Guo, J. Shi, H. Ji, Q. Ouyang and Y. Chen, "Characterization of microfluidic fuel cell based on multiple laminar flow," *Microelectronic Engineering,* vol. 84, pp. 1182-1185, 2007.

[34] K. S. Salloum, J. R. Hayes, C. A. Friesen and J. D. Posner, "Sequential flow membraneless microfluidic fuel cell with porous electrodes," *J. Power Sources,* vol. 180, pp. 243-252, 2008.

[35] E. Kjeang, J. McKechnie, D. Sinton and N. Djilali, "Planar and three-dimensional microfluidic fuel cell architectures based on graphite rod electrodes," *J. Power Sources,* vol. 168, pp. 379-390, 2007.

[36] E. Kjeang, R. Michel, D. A. Harrington, N. Djilali and D. Sinton, "A microfluidic fuel cell with flow-through porous electrodes," *J. Am. Chem. Soc.,* vol. 130, pp. 4000-4006, 2008.

[37] E. Kjeang, B. T. Proctor, A. G. Brolo, D. A. Harrington, N. Djilali and D. Sinton, "High-performance microfluidic vanadium redox fuel cell," *Electrochim. Acta,* vol. 52, pp. 4942-4946, 2007.

[38] S. Hasegawa, K. Shimotani, K. Kishi and H. Watanabe, "Electricity generation from decomposition of hydrogen peroxide," *Electrochemical and Solid-State Letters,* vol. 8, pp. A119, 2005.

[39] C. Rice, S. Ha, R. I. Masel, P. Waszczuk, A. Wieckowski and T. Barnard, "Direct formic acid fuel cells," *J. Power Sources,* vol. 111, pp. 83-89, 9/18, 2002.

[40] Y. Zhu, Z. Khan and R. I. Masel, "The behavior of palladium catalysts in direct formic acid fuel cells," *J. Power Sources,* vol. 139, pp. 15-20, 1/4, 2005.

[41] A. Kundu, J. Jang, J. Gil, C. Jung, H. Lee, S. H. Kim, B. Ku and Y. Oh, "Micro-fuel cells--Current development and applications," *J. Power Sources,* vol. 170, pp. 67-78, 2007.

[42] J. D. Morse, "Micro-fuel cell power sources," *Int. J. Energy Res.,* vol. 31, pp. 576-602, 2007.

[43] M. Togo, A. Takamura, T. Asai, H. Kaji and M. Nishizawa, "An enzyme-based microfluidic biofuel cell using vitamin K3-mediated glucose oxidation," *Electrochim. Acta,* vol. 52, pp. 4669-4674, 2007.

[44] C. M. Moore, S. D. Minteer and R. S. Martin, "Microchip-based ethanol/oxygen biofuel cell," *Lab on a Chip,* vol. 5, pp. 218-225, 2005.

[45] M. Togo, A. Takamura, T. Asai, H. Kaji and M. Nishizawa, "Structural studies of enzyme-based microfluidic biofuel cells," *J. Power Sources,* vol. 178, pp. 53-58, 2008.

[46] C. P. de Leon, F. Walsh, A. Rose, J. Lakeman, D. Browning and R. Reeve, "A direct borohydride--Acid peroxide fuel cell," *J. Power Sources,* vol. 164, pp. 441-448, 2007.

[47] G. H. Miley, N. Luo, J. Mather, R. Burton, G. Hawkins, L. Gu, E. Byrd, R. Gimlin, P. J. Shrestha and G. Benavides, "Direct NaBH4/H2O2 fuel cells," *J. Power Sources,* vol. 165, pp. 509-516, 2007.

[48] N. Choudhury, R. Raman, S. Sampath and A. Shukla, "An alkaline direct borohydride fuel cell with hydrogen peroxide as oxidant," *J. Power Sources,* vol. 143, pp. 1-8, 2005.

[49] R. Aogaki, E. Ito and M. Ogata, "A new flow-type cell by the application of magnetic microfluidic chip," *Journal of Solid State Electrochemistry,* vol. 11, pp. 757-762, 2007.

[50] L. Gu, N. Luo and G. H. Miley, "Cathode electrocatalyst selection and deposition for a direct borohydride/hydrogen peroxide fuel cell," *J. Power Sources,* vol. 173, pp. 77-85, 2007.

[51] M. Skyllas-Kazacos, C. Menictas and M. Kazacos, "Thermal stability of concentrated V (V) electrolytes in the vanadium redox cell," *J. Electrochem. Soc.,* vol. 143, pp. L86, 1996.

[52] S. K. Yoon, G. W. Fichtl and P. J. A. Kenis, "Active control of the depletion boundary layers in microfluidic electrochemical reactors," *Lab on a Chip,* vol. 6, pp. 1516-1524, 2006.

[53] K. G. Lim and G. T. R. Palmore, "Microfluidic biofuel cells: The influence of electrode diffusion layer on performance," *Biosensors and Bioelectronics,* vol. 22, pp. 941-947, 2007.

[54] F. Chen, M. H. Chang and M. K. Lin, "Analysis of membraneless formic acid microfuel cell using a planar microchannel," *Electrochim. Acta,* vol. 52, pp. 2506-2514, 2007.

[55] W. Y. Chen and F. Chen, "Theoretical approaches to studying the single and simultaneous reactions in laminar flow-based membraneless fuel cells," *J. Power Sources,* vol. 162, pp. 1137-1146, 2006.

[56] D. H. Ahmed, H. B. Park and H. J. Sung, "Optimum geometrical design for improved fuel utilization in membraneless micro fuel cell," *J. Power Sources,* vol. 185, pp. 143-152, 2008.

[57] E. Khabbazi, A. J. Richards and M. Hoorfar, "Numerical study of the effect of the channel and electrode geometry on the performance of microfluidic fuel cells," *J. Power Sources,* vol. In Press, Accepted Manuscript, .

[58] F. Chen, M. H. Chang and C. W. Hsu, "Analysis of membraneless microfuel cell using decomposition of hydrogen peroxide in a Y-shaped microchannel," *Electrochim. Acta,* vol. 52, pp. 7270-7277, 2007.

[59] R. Bird, W. Stewart and E. Lightfoot, "Transport Phenomena John Wiley & Sons," *New York,* 2002.

[60] Z. Shi, X. Wang and Z. Zhang, "Comparison of two-dimensional PEM fuel cell modeling using COMSOL multiphysics," in *Proceedings of the COMSOL Users Conference,* 2006, .

[61] S. Um, C. Wang and K. Chen, "Computational fluid dynamics modeling of proton exchange membrane fuel cells," *JOURNAL-ELECTROCHEMICAL SOCIETY,* vol. 147, pp. 4485-4493, 2000.

[62] A. M. J. Bazylak, "Modelling microscale fuel cells," 2009.

[63] Y. Mu, T. T. Ren and H. Q. Yu, "Drag coefficient of porous and permeable microbial granules," *Environ. Sci. Technol.,* vol. 42, pp. 1718-1723, 2008.

[64] E. Rodriguez, F. Giacomelli and A. Vazquez, "Permeability-porosity relationship in RTM for different fiberglass and natural reinforcements," *J. Composite Mater.,* vol. 38, pp. 259, 2004.

[65] M. W. Verbrugge and R. F. Hill, "Ion and Solvent Transport in Ion-Exchange Membranes," *J. Electrochem. Soc.,* vol. 137, pp. 893, 1990.

[66] M. Ghouse, A. Al-Boeiz, H. Abaoud and M. Al-Garni, "Preparation and evaluation of PTFE-bonded porous gas diffusion carbon electrodes used in phosphoric acid fuel cell applications," *Int J Hydrogen Energy,* vol. 20, pp. 727-736, 1995.

[67] J. Gonzaléz-Garcia, P. Bonete, E. Expósito, V. Montiel, A. Aldaz and R. Torregrosa-Maciá, "Characterization of a carbon felt electrode: structural and physical properties," *Journal of Materials Chemistry,* vol. 9, pp. 419-426, 1999.

[68] F. Rahman and M. Skyllas-Kazacos, "Vanadium redox battery: Positive half-cell electrolyte studies," *J. Power Sources,* vol. 189, pp. 1212-1219, 2009.

[69] D. You, H. Zhang and J. Chen, "A simple model for the vanadium redox battery," *Electrochim. Acta,* 2009.

[70] T. YAMAMURA, N. WATANABE, T. YANO and Y. SHIOKAWA, "Electron-transfer kinetics of Np3 /Np4 , NpO (/NpO2 2, V2 /V3 , and VO2 /VO 2 at carbon electrodes," *J. Electrochem. Soc.,* vol. 152, pp. A830-A836, 2005.

[71] H. Zhou, H. Zhang, P. Zhao and B. Yi, "A comparative study of carbon felt and activated carbon based electrodes for sodium polysulfide/bromine redox flow battery," *Electrochim. Acta,* vol. 51, pp. 6304-6312, 2006.

[72] T. Zhao, *Micro Fuel Cells: Principles and Applications.* Academic Pr, 2009.